Baryon Production in Z Decay

Christopher G. Tully

A DISSERTATION
PRESENTED TO THE FACULTY
OF PRINCETON UNIVERSITY
IN CANDIDACY FOR THE DEGREE
OF DOCTOR OF PHILOSOPHY

RECOMMENDED FOR ACCEPTANCE
BY THE DEPARTMENT OF PHYSICS

January 1998

in memory of my father

ABSTRACT

How quarks become confined into ordinary matter is a difficult theoretical question. The point at which this occurs cannot be measured by experiment, but other properties related to confinement can. Baryon production is a situation where one type of confinement is chosen over another.

In this thesis, production rate measurements have been performed for Σ^+ and Σ^0 baryons produced in hadronic decays of the Z^0. The rates are low compared to meson production, but the particular properties of Σ^+ and Σ^0 decay allow these particles to be identified amongst the many mesons accompanying them. The average number of Σ^+ and Σ^0 per hadronic Z^0 decay was found to be

$$\left\langle N_{\Sigma^+ + \overline{\Sigma}^+} \right\rangle = 0.092 \pm 0.011_{stat} \pm 0.011_{syst}$$

and

$$\left\langle N_{\Sigma^0 + \overline{\Sigma}^0} \right\rangle = 0.112 \pm 0.016_{stat} \pm 0.025_{syst} \ ,$$

respectively.

These measurements take advantage of the unique photon detection capability of the L3 Experiment. The rates are in agreement with those measured by other LEP detectors.

ACKNOWLEDGEMENTS

This thesis would not have been complete without the contributions of some special individuals.

The inspiration of studying baryon decays came from my undergraduate research. I benefited a great deal from working under Jim Branson and then later with Krishna Kumar on electroweak measurements with leptons. Harvey Newman gave me encouragement and the opportunity to do this work.

My approach to doing research changed a great deal as a graduate student. The operation and measurement capability of the detector became an important concern, especially for the Princeton group. At this point, Peter Denes became something of a mentor to me. My several years of work with him on his projects including the BGO readout enabled me to play an important part in the experiment. I had the pleasure of working with other talented and devoted people during this time, among them were Vinod Gupta, J.J. Blaising, Xudong Cai, Giorgio Gratta and Yannis Karyotakis.

The completion of my analysis proper needed the mathematical help of two people. Scott Snyder introduced to me the techniques of constrained fitting, and Gerhard Raven and his work on the UCSD b-tag provided invaluable tracking information for my final measurements.

What remains is the emotional support and friendships which kept me on track and protected my sanity–although some beg to differ. Foremost was my advisor Pierre Piroué who always managed to look over me and could readily engage in diverse conversation which I enjoyed. The Dutch clan and others into which I was initiated by Marcel Merk and the soccer team beared with my lunch time discussions for years. Gerhard Raven, Franck Filthaut, Mirna van Hoek, Tasja van Rhee, Eric Laenen, Paul de Jong, Wim van Rossum, Sanda Muijs, Daniel van Dierendonck and others were all victim. My experiences at Carnaval with Marcel, Esther and their families I will never forget, nor the music.

From Chorus, I remember Gus Brooijmans, Muriel Vander Donckt, David

Saltzberg and others. From old acquaintance and elsewhere, there were Wenwen Lu, Alex Shvorob, Aaron Dominguez, Julie Abo, Ian Fisk, Benjamin Lev, Jill Soha and Paul Rubinov.

Merci à Laurence Barrin, Yvette Bernard, Caroline Laignel et Rachelle Decreuse qui sont toujours sympa.

Finally, I look dearly to my mom, Mike and his family, and Joyce Gledhill for being there all these years and to Tania for seeing something in me beyond this work.

CONTENTS

1. INTRODUCTION

Reaching higher energies, probing smaller distances, revisiting earlier times in the evolution of the universe, these are all ways of discussing the direction which particle physicists pursue to uncover the elementary building blocks and interactions of matter. When relativity and quantum mechanics were merged in the late 1920's to form a more complete description of particle dynamics, it became understood that the number and types of particles in a system did not have to remain unchanged in time. The freedom to annihilate and create new particles was linked to the relativistic quantum description of elementary forces.

In this thesis, a study is made of the rate of production of different types of baryons, heavier versions of ordinary nuclear matter. Baryons are particularly interesting to study because they are conserved. This means that for every baryon produced, an anti-baryon will also be produced. Baryons are heavier than other particles, hence the origin of their name. Their rate of production is related to their mass, their conservation law and properties of the "system" from which they arise. In particular, the production rate dependence on baryon mass is a measure of the temperature at which quarks become confined within ordinary matter. Long-lived but unstable baryons, known as hyperons, have a signature which allows them to be identified amongst other particle decays. That is why the Σ^+ and Σ^0 baryons, in particular, are measured in this thesis, and not others.

The creation of heavy matter is achieved by the operation of large-scale particle colliders. Charged particles introduced into the nearly perfect vacuum of a beam pipe can be accelerated and steered with electromagnetic fields. The Large Electron-Positron(LEP) Collider located near Geneva, Switzerland is today the highest energy electron-positron collider in the world. LEP was designed to have four principal collision points equally spaced along its 27 km circumference. The L3 Experiment, led by Samuel C. C. Ting, occupies one of these interaction regions and is the source of data used in this thesis.

1.1 Particle Creation and Detection

At the central-most part of the L3 Experiment, high-energy beams of electrons and positrons are brought into collision. The particles created in these collisions are detected by the surrounding apparatus. The apparatus consists of two main components, tracking and calorimetry.

The goal of the inner part of the detector, the tracking, is to measure the trajectories of the particles coming from the center of the detector while affecting the ideal "unmeasured" trajectories as little as possible. High-energy particles can travel through thin, light materials and gaseous volumes without losing a large fraction of their initial momentum. However, the small amount they do lose can be used to track their trajectories.

The function of the outer part of the detector, the calorimetry, is to stop and measure the energies of all the particles which have travelled through the tracking region. This task is achieved by using tons of heavy materials interspersed or instrumented with devices that gauge the total number of material interactions which occur during the stopping process. The number and distribution of material interactions can then be related to initial energies and types of particles which hit the calorimetry.

1.2 Searching for Particle Decays

Measuring the properties of short-lived particles requires a bit of detective work. Only a handful of particles produced in beam collisions live long enough to make it out of the evacuated beam pipe. Therefore, the bulk of the particles that enter the tracking and calorimetry are long-lived particles which come from particle decays.

But, in fact, how does one know that the short-lived particles even existed if they cannot be measured directly. When a particle decays, the particles coming from this decay will satisfy a set of kinematic relationships. Although the kinematics of the long-lived particles are measured with the tracking and calorimetry, there are measurement errors. This introduces the concept of satisfying kinematic relationships "within errors."

When searching for the evidence of a particular particle decay among the decay products of several different particles, there is no "smoking gun." The analysis requires that distributions of candidate particle decays show statistical evidence for the presence of a particular particle type. The most telling distribution to identify a particle is the mass distribution. In addition to a set of discrete symmetry and angular momentum quantum numbers, particles are distinguished by the way they interact and by their mass.

1.3 Going Back in Time

As was indicated, heavy particles are formed in the vacuum of the beam pipe when high-energy electrons and positrons are collided. This is not a normal everyday experience. The evolution of interaction energies into particle states froze out as the universe cooled down. Typical interaction energies in everyday life are well below that needed to generate nuclear matter.

The central story is about how particle interactions will behave when the interaction energies become closer and closer to those believed to be present in the early universe. The LEP Collider energies were designed for studying a particular period of history called the Electroweak Era. During this period, the interaction responsible for radioactivity in heavy atomic nuclei takes on a new form. This form is called the Z particle, and it is created when an electron and positron collide with an energy which is equal to or within close vicinity of the physical mass of the Z particle (multiplied by c^2 from Einstein's $\mathrm{E} = \mathrm{mc}^2$).

When Z particles decay into sub-nuclear particles, "quarks," the ensuing interactions generate a large number and variety of strongly interacting particles, known as "hadrons." The formation of hadrons with different masses and quantum numbers depends on the properties of the quarks coming from Z decay and the elementary interactions. This process cannot yet be calculated, but appears to occur at a characteristic temperature, the hadronization temperature. Understanding how this feature is related to the elementary strong interaction and quark confinement could have an impact on properties of the early universe and, hence, on yet-to-be-seen aspects of today's universe. The high-energy frontier of reaching the unification of all the forces of nature and how they entangle in the dawn of all matter formation seems today as far away as the most distant galaxies, but with every observation and study, this gap diminishes.

2. THE HISTORY BEHIND SUB-NUCLEAR PARTICLES: QUARKS

Many original ideas and challenging measurements brought about the quark model and the theory of the strong interaction. The following historical perspective was drawn mainly from a conference[1] which coincided with the start of this thesis research. Hopefully, some of the terms and ideas in Chapter 3 will become more clear when viewed with their historical context in mind.

2.1 Discovery of the Pion

The distinction between different chemical elements has its origin in the nuclei of atoms. However, nuclei play a very passive role in chemistry. It's not the nuclei themselves which determine the chemical behavior of the different elements, but rather the system of electrons which forms from the electromagnetic interaction with the nucleus. The interaction which forms the nuclei themselves has a much shorter distance over which it acts.

H. Yukawa, in 1935, explained the range of the nuclear force by attributing its origin to the exchange of a massive particle called the pion. Quantum mechanics views the binding of atomic electrons to the charge of a nucleus as due to the exchange of photons. Photons are massless, and the range of the electromagnetic interaction is infinite. Yukawa saw the limit in the range of the interaction binding nucleons within nuclei as being due to the exchange of a massive particle. The mass of the exchanged particle limits the range of the interaction. The measured range of the nuclear force allowed Yukawa to predict the mass of the pion. The pion was later discovered at its predicted mass in 1947 by C.F. Powell and his coworkers [2].

---

[1] Conference on the History of Original Ideas and Basic Discoveries in Particle Physics, held at the "Ettore Majorana" Centre for Scientific Culture in Erice, Sicily, July 27–August 4, 1994 [1].

2.2 The Quark Constituent Model

Strangely enough, the strong interaction didn't stop with protons, neutrons and pions. Not only would the scattering of pions off of protons reveal new higher mass versions of the proton, but at sufficiently high energies, pairs of particles would be formed that have distinctly different behavior from that of pions and protons. A new "charge" was needed to describe the behavior of these "strange" particles. This charge was named hypercharge and was introduced in 1953 by M. Gell-Mann and K. Nishijima as a quantity which was conserved by the strong interaction.

By 1961, M. Gell-Mann and Y. Ne′eman developed a mathematical description which was able to explain the proliferating "zoo" of particles being found by experimentalists. The algebra of SU(3) classified strongly interacting particles by their spin and parity. This description created geometrically constructed tables of particle types. Many of the predicted particle types had already been measured, but some had not, the most illustrious of which was the $\boldsymbol{\Omega}^-$(sss).

Spin-$\frac{1}{2}^+$ Octet			**Spin-$\frac{3}{2}^+$ Decuplet**			
n(udd)		**p**(uud)	$\boldsymbol{\Delta}^-$(ddd)	$\boldsymbol{\Delta}^0$(udd)	$\boldsymbol{\Delta}^+$(uud)	$\boldsymbol{\Delta}^{++}$(uuu)
$\boldsymbol{\Sigma}^-$(dds)	$\boldsymbol{\Sigma}^0$(uds) $\boldsymbol{\Lambda}^0$(uds)	$\boldsymbol{\Sigma}^+$(uus)	$\boldsymbol{\Sigma}^{*-}$(dds)	$\boldsymbol{\Sigma}^{*0}$(uds)	$\boldsymbol{\Sigma}^{*+}$(uus)	
$\boldsymbol{\Xi}^-$(dss)		$\boldsymbol{\Xi}^0$(uss)	$\boldsymbol{\Xi}^{*-}$(dss)	$\boldsymbol{\Xi}^{*0}$(uss)		
			$\boldsymbol{\Omega}^-$(sss)			

Flavor Symmetry: SU(3) Baryon Families[2]

It was not until 1964 that M. Gell-Mann and independently G. Zweig proposed that SU(3) tables could be explained by describing all strongly interacting particles, "hadrons," as being made from three flavors of quarks; u, d

---

[2] Many baryons are named with capital Greek letters.

and s [3]. The quarks were assigned to have spin-1/2 and fractional electric charge (+2/3, −1/3 and −1/3 respectively). This scheme identified protons and its heavier versions, generally called "baryons," as being composed of three quarks.

2.3 Deep Inelastic Scattering

As fantastic as the notion of quarks sounded, the idea that they would have fractional charge was unsettling. No experimental evidence existed to support this conjecture. Also missing was an explanation of how the $\mathbf{\Delta}^{++}$(uuu), for instance, could have a wavefunction with complete symmetry in spin and flavor, but still have an overall antisymmetric wavefunction. This is the well-known Pauli exclusion principle for particles with fractional total angular momentum. Some feature intrinsic to the strong interaction seemed to be missing.

Experiments at the Stanford Linear Accelerator(SLAC) starting in 1967 charted the way with high-energy electron scattering experiments off of protons and deuterons. In the case where the scattered electron has caused a change in the internal structure of the proton, this collision is called inelastic. Inelastic collisions are clearly identified by the kinematic relationship of the incoming and scattered electron. The inelastic behavior of the target protons and deuterons was measured for a range of scattering angles and energies.

Several important properties of the quark model and the strong interaction were measured in electron-nucleon deep-inelastic scattering experiments. The scattering data from different energies and angles was found to be related by a specific scaling property, now called "Bjorken scaling" [4]. This behavior implied that point-like charged constituents were present within protons and neutrons and that these constituents behaved as free particles, at least for a short time, in deeply inelastic collisions. The electron scattering data also determined by means of the Gross-Callan relationship that the charged constituents in nucleons were spin-1/2 particles [5].

Electrons were not the only means of looking inside of a nucleon. High-energy neutrinos probe the nucleon by means of the weak interaction alone. The uniquely different interaction of the neutrino was used by D. Gross and C. Llewellyn-Smith to derive a sum rule which counted the net number of quarks present in nucleons [6]. The quark model prediction of Gell-Mann and Zweig of nucleons containing three quark constituents was verified by the Gargamelle Experiment at the European Center for Nuclear Research(CERN) in 1974 [3,7].

2.4 Quantum Chromodynamics

That "something missing" from the strong interaction was arriving. A new quantity emerged that would be the analogue of the electric charge for the strong interaction. It was called "color." The behavior of color explained the Δ^{++}(uuu) wavefunction and why hadrons had no long-range strong interaction. The dynamics of color, however, such as why quarks were confined to hadrons but still behaved like free particles in deep-inelastic scattering experiments, were as yet unknown.

In 1973 D. Gross and F. Wilczek, and independently H.D. Politzer, calculated asymptotic freedom for the non-Abelian gauge theory based on an exact SU(3) color symmetry group [8]. This theory, also called Quantum Chromodynamics or QCD, plays the part of the renormalizable field theories used to describe the weak and electromagnetic interactions. It is the fundamental theory of the strong interaction. For the region in energy where the strong coupling constant is small, accurate QCD calculations can be made and compared with experiment.

2.5 Quarks and the Electroweak Interaction

The unification of the weak and electromagnetic forces implied that left-handed quarks came in doublets. This parallel to the weak charged-current interaction of leptons gave structure to the assignment of quark charges and flavors. The first verification of this theory came from the results on elastic neutrino-nucleon scattering measurements made by the Gargamelle Experiment at CERN in 1973 [9], the discovery of neutral currents. Elastic scattering of a neutrino off of a quark was predicted to occur through the exchange of the massive Z particle. This particle was later produced in proton anti-proton collisions at CERN in 1983 [10].

The 1973 picture of the electroweak doublets of particles was incomplete. Both the theoretical analyses of axial anomalies and the Glashow-Iliopoulos-Maiani(GIM) mechanism implied the existence of a second charge +2/3 quark [11]. The GIM mechanism as it applied to neutral kaon decays to dimuons was used to estimate the mass of the missing "charm" quark.

$$\begin{array}{r} \text{electron-neutrino} \\ \text{electron} \end{array} \begin{pmatrix} \nu_{\mathrm{e}} \\ \mathrm{e}^- \end{pmatrix} \begin{pmatrix} \nu_\mu \\ \mu^- \end{pmatrix} \begin{array}{l} \text{muon-neutrino} \\ \text{muon} \end{array}$$

$$\begin{array}{r} +2/3\ \text{quark} \\ -1/3\ \text{quark} \end{array} \begin{pmatrix} u \\ d \end{pmatrix} \begin{pmatrix} \\ s \end{pmatrix} \begin{array}{l} \\ -1/3\ \text{“strange”-quark} \end{array}$$

Electroweak Doublets: Known Quarks and Leptons in the Year 1973

In November of 1974, the charm quark was discovered in the form of the narrow charm anti-charm quark bound state produced in both the proton fixed-target experiment of Samuel C.C. Ting in Brookhaven, New York and in electron-positron collisions at SLAC in California. This moment of time was known as the “November Revolution.” It marked an incredible period of scientific development in the area of particle physics. There were now known to be four quarks. A standard model describing the electroweak interactions of both quarks and leptons had been formed.

2.6 Gluon Radiation from Quarks

In QCD, quarks are attracted to each other by the exchange of “gluons.” In high-energy collisions, quarks can radiate gluons in the same way as electrons exhibit photon emission in the electromagnetic interaction. An essential property of gluons and the strong interaction, is that the gluons, themselves, carry the color charge. Scattered quarks and energetic gluons will always form hadrons from the growing strength of the strong interaction as colored particles separate. Hadrons are colorless and exhibit no long-range strong interaction.

In 1979, the PETRA accelerator in Hamburg, Germany began colliding electrons and positrons in the search for the QCD prediction of gluon emission from quarks. This was a difficult step for the four PETRA experiments as the observation of “jets” of hadrons coming from energetic quark production was a new phenomenon. The production of a quark anti-quark pair with, in addition, the emission of an energetic gluon causes three jets of particles to be formed. The QCD prediction that these jets of particles should line in a plane and that the angles and energies of the three jets should follow a statistical pattern was verified, in particular, by the MARK-J, TASSO and PLUTO Experiments. The first measurement of the strength of the strong interaction coupling constant for three-jets events was performed by the JADE Experiment, indicating a size over a factor of 20 larger than the electromagnetic interaction.

3. THE STANDARD MODEL AND ITS HELPERS

This chapter contains all the theory and phenomenology needed to describe and interpret the measurements presented in Chapter 6.

3.1 Fundamental Interactions

The Dirac equation, introduced in 1928, was the first relativistically covariant equation describing a quantum mechanical spin-1/2 particle. The equation in modern notation is written,

$$(i\gamma_\mu \partial^\mu - m)\Psi = 0 \tag{3.1}$$

where m is the mass of the particle.
The ability to change the phase of the wavefunction $\Psi \rightarrow \Psi' = e^{iq\chi(\vec{x},t)}\Psi$ in a way which varies in space and time $(\vec{x}, t)$ violates the covariance of equation (3.1).

The covariance is re-established by introducing a field A^μ such that,

$$A^\mu \rightarrow A'^\mu = A^\mu - \partial\chi$$

$$\partial^\mu \rightarrow D^\mu \equiv \partial^\mu + iqA^\mu \; .$$

The Dirac equation, written with the covariant derivative D^μ, now describes the motion of a particle with charge q interacting with an electromagnetic field.

Electromagnetism is an example of how local gauge invariance generates a fundamental interaction described by a field. To describe the weak and electromagnetic interactions together, the covariant derivative becomes,

$$\partial^\mu \rightarrow D^\mu \equiv \partial^\mu - ig\boldsymbol{T} \cdot \boldsymbol{W}^\mu + ig'\frac{Y}{2}B^\mu \; . \tag{3.2}$$

This introduces three new fields $\boldsymbol{W}^\mu = (W_1^\mu, W_2^\mu, W_3^\mu)$, and in addition, the electromagnetic interaction has changed slightly, now written B^μ, as will be explained below. The operator $\boldsymbol{T}$ determines the strength of the weak interaction. The magnitude and components of $\boldsymbol{T}$ are different for right-handed and left-handed particles[1].

Quarks and leptons are characterized by the way they interact under the weak interaction, as seen in Table 3.1. Left-handed particles appear in doublets ($T = \frac{1}{2}$), and right-handed particles are singlets ($T = 0$).

	The Left-Handed World			The Right-Handed World		
lepton-neutrino lepton	$\begin{pmatrix}\nu_{\mathrm{e}} \\ \mathrm{e}^-_L\end{pmatrix}$	$\begin{pmatrix}\nu_\mu \\ \mu^-_L\end{pmatrix}$	$\begin{pmatrix}\nu_\tau \\ \tau^-_L\end{pmatrix}$	e^-_R	μ^-_R	τ^-_R
+2/3 quark −1/3 quark	$\begin{pmatrix}u_L \\ d'_L\end{pmatrix}$	$\begin{pmatrix}c_L \\ s'_L\end{pmatrix}$	$\begin{pmatrix}t_L \\ b'_L\end{pmatrix}$	u_R d'_R	c_R s'_R	t_R b'_R

Tab. 3.1: The World of Quarks and Leptons is Split by the Weak Interaction

The weak interaction as it was introduced in equation (3.2) lacks one of its most telling features – that is, being weak. Fields, such as A^μ, have an equation of motion. They are, in their own right, particles, as the photon is the particle described by A^μ. Apart from the coupling constants being potentially smaller, the interaction would be weak if the particles describing the $\boldsymbol{W}^\mu$ had non-zero masses.

The theoretical difficulty with introducing a non-zero mass to a field is that the equation of motion describing the field loses its invariance under local gauge transformations. Even so, the local gauge invariance can be present, but hidden, through relationships between masses and couplings. The masses of the particles describing the weak interaction were discovered by way of a theory of hidden gauge invariance, known as the electroweak theory of S. Glashow, A. Salam, and S. Weinberg [12].

---

[1] The handedness of a particle is determined by the relative orientation of its spin and momentum.

3.1.1 The GSW Standard Model of Electroweak Interactions

Starting with the covariant derivative (3.2), the kinetic energy of a spin-0 particle is given by,

$$|\partial^\mu \phi|^2 \to \left| \left(\partial^\mu - ig\boldsymbol{T}\cdot\boldsymbol{W}^\mu + ig'\frac{Y}{2}B^\mu \right)\phi \right|^2 \ . \tag{3.3}$$

In the case where the spin-0 particle has a self-interacting potential known as the Higgs potential,

$$V(\phi) = -\mu^2|\phi|^2 + \lambda|\phi|^4 \ ,$$

for μ^2 and λ positive, the minimum value of $|\phi|^2$ is non-zero, $|\phi|^2_{min} = \mu^2/2\lambda$.

With $|\phi|^2_{min}$ non-zero, the kinetic energy term of the Higgs particle becomes the difference of ϕ with respect to its minimum potential energy. In the single doublet model ($T = \frac{1}{2}, Y = 1$), this minimum is chosen to be,

$$\langle\phi\rangle = \frac{1}{\sqrt{2}}\begin{pmatrix} 0 \\ \sqrt{\mu^2/\lambda} \end{pmatrix} \ .$$

This generates a constant term from the kinetic energy (3.3),

$$\begin{aligned} &\left| \left(-ig\boldsymbol{T}\cdot\boldsymbol{W}^\mu + ig'\frac{Y}{2}B^\mu \right)\langle\phi\rangle \right|^2 \\ &= \frac{\mu^2}{8\lambda}(gW_3^\mu + g'B^\mu)^2 + \frac{\mu^2 g^2}{8\lambda}(W_1 - iW_2)_\mu (W_1 + iW_2)^\mu \\ &\equiv \frac{1}{2}M_Z^2(Z^\mu)^2 + M_W^2 W_\mu^+ W^{-\mu} \ , \end{aligned}$$

namely, the masses of the W^+, W^- and Z^0 particles, which are the physical fields of the weak interaction. The remaining field,

$$A^\mu = \frac{-g'W_3^\mu + gB^\mu}{\sqrt{g^2 + g'^2}} \ ,$$

is the massless field of the electromagnetic interaction.

3.2 The Properties of Quarks from Z^0 Decay

The couplings of the Z^0 to quarks and leptons, listed in Table 3.1, can be separated into left-handed couplings and right-handed couplings by use of the helicity projection operators (acting on a particle f).

$$f_L = \frac{1-\gamma_5}{2} f, \quad f_R = \frac{1+\gamma_5}{2} f$$

Then, expressing the interaction in the form,

$$\bar{f}\gamma_\mu Z^\mu \left(c_L^f \frac{1-\gamma_5}{2} + c_R^f \frac{1+\gamma_5}{2} \right) f$$

the values for c_L^f and c_R^f are

$$c_L^f = T_3 - q\sin^2\bar{\theta}_{\mathrm{W}}, \quad c_R^f = -q\sin^2\bar{\theta}_{\mathrm{W}} \tag{3.4}$$

with

$$\sin^2\theta_{\mathrm{W}} \equiv 1 - (M_W^2/M_Z^2) \approx 0.224$$

$$\sin^2\bar{\theta}_{\mathrm{W}} \approx 0.232 \tag{3.5}$$

where the effective coupling, $\sin^2\bar{\theta}_{\mathrm{W}}$, deviates from the tree-level coupling[2].

Of particular interest to the measurements made in Chapter 6 is the fraction of Z^0 decays to quark-antiquark ($q\bar{q}$) pairs,

$$Br(\mathrm{Z}^0 \to q\bar{q}) = \frac{N_c \sum_{f=d,u,s,c,b}\left(|c_L^f|^2 + |c_R^f|^2\right)}{N_c \sum_{f=d,u,s,c,b}\left(|c_L^f|^2 + |c_R^f|^2\right) + \sum_{f=e,\nu_e,\mu,\nu_\mu,\tau,\nu_\tau}\left(|c_L^f|^2 + |c_R^f|^2\right)} \approx 70\%$$

where $N_c = 3$ is the number of colors in the strong interaction[3].

The longitudinal polarization of quarks coming from Z^0 decay is

$$\mathcal{P}_q = -\frac{|c_L^f|^2 - |c_R^f|^2}{|c_L^f|^2 + |c_R^f|^2} = -\mathcal{P}_{\bar{q}}\ . \tag{3.6}$$

---

[2] This deviation allowed LEP measurements to predict the mass of the top quark before it was discovered at Fermilab in 1995 [13]. Similar predictions now exist for the Higgs mass.

[3] The quark sums have been modified by a QCD correction factor $\delta_{\mathrm{QCD}} \approx 1+\alpha_s(M_Z)/\pi$, not written in the above formula. This factor gives cross-section measurements sensitivity to the strong coupling constant.

3.3 Quantum Chromodynamics

The inclusion of the elementary strong interaction into the covariant derivative adds eight new fields. The particles associated to these fields are called gluons[4].

$$\partial^\mu \to D^\mu \equiv \partial^\mu - ig\,\boldsymbol{T}\cdot\boldsymbol{W}^\mu + ig'\frac{Y}{2}B^\mu + ig_s\,\boldsymbol{\Gamma}\cdot\boldsymbol{G}^\mu$$

The eight fields $\boldsymbol{G}^\mu = (G^\mu_{r\bar g}, G^\mu_{r\bar b}, G^\mu_{g\bar r}, G^\mu_{g\bar b}, G^\mu_{b\bar r}, G^\mu_{b\bar g}, G^\mu_{(r\bar r - g\bar g)/\sqrt{2}}, G^\mu_{(r\bar r + g\bar g - 2b\bar b)/\sqrt{6}})$ have a correspondence to the eight generators of the SU(3) color group[5]. The gluon indices are closely linked with color flow (Figures 3.1 and 3.2).

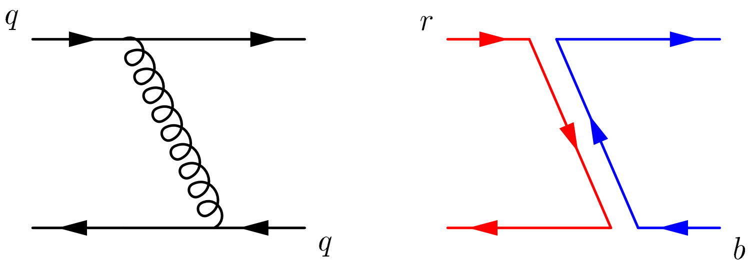

Fig. 3.1: Color flow demonstrated in single gluon exchange.

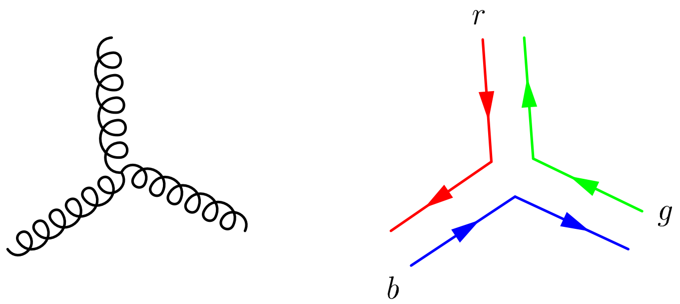

Fig. 3.2: Color flow demonstrated in the triple gluon vertex.

The strength of the strong interaction changes with scale following the principle of the renormalization group. The strong coupling,

$$\alpha_s = \frac{g_s^2}{4\pi}$$

---

[4] Electroweak symmetry breaking will not generate mass in the gluon fields as long as the Higgs scalar has no color charge.

[5] The indices r, g and b represent the colors red, green and blue. The combination of all three colors is white, or “color neutral.”

has a dependence on the renormalization scale μ which to one-loop is given by[6],

$$\mu \frac{\partial \alpha_s}{\partial \mu} \equiv \beta(\alpha_s) \approx -b_0 \frac{\alpha_s^2}{2\pi} = -(\frac{11}{3} N_c - \frac{2}{3} N_f) \frac{\alpha_s^2}{2\pi} \tag{3.7}$$

where $N_c = 3$ is the number of colors and $N_f \leq 6$ is the number of quark flavors contributing to the loop corrections. This equation predicts that the strength of the strong coupling constant decreases at high energy. It also identifies a quantity Λ_C^2 known as the "Landau pole,"

$$\Lambda_C^2 \equiv \mu^2 \exp\left(\frac{-4\pi}{\alpha_s(\mu)\, b_0}\right) . \tag{3.8}$$

At the scale of the Landau pole, the strength of the strong interaction becomes divergently strong. This is believed to be reason why all quarks and gluons become confined within hadrons. Confinement cannot be calculated with Feynman perturbation theory, and only has an approximate phenomenological description.

3.3.1 Hadronization Phenomenology

Two types of hadrons have been measured by experiments. These are mesons, bound states of $q\bar{q}$, and baryons, bound states of qqq, and their anti-particles. In both cases, the color potential for the singlet combination is attractive.

hadron type	Color Representation ($1 \equiv$ singlet)	Color Coupling of the Singlet (negative is attractive)
mesons	$3 \otimes \bar{3} = 8 \oplus 1$	$-\frac{4}{3}\alpha_s$
baryons	$3 \otimes 3 \otimes 3 = 10 \oplus 8 \oplus 8 \oplus 1$	$-\frac{2}{3}\alpha_s$

Tab. 3.2: Sign of the Potential Energy for Color Singlet Combinations

The basic features of hadron production rates in e^+e^- annihilation are described by the following parameterization [14].

$$\langle N \rangle = C_{\sqrt{s}} \cdot \frac{2J+1}{C_B} \cdot (\gamma_s)^{N_s} \cdot e^{-\frac{E_{bind}}{T}} \tag{3.9}$$

---

[6] First computed by D. Gross and F. Wilczek, and independently by H.D. Politzer [8].

The rate $\langle N\rangle$ is the expected number of primary hadrons[7] produced per event. The overall normalization factor $C_{\sqrt{s}}$ depends on the center-of-mass energy. The parameter C_B is a suppression factor for baryon production (defined to be 1.0 for mesons). The constants T and γ_s are universal[8], and the values of J, N_s and E_{bind} depend on properties of the hadron. Namely, J is the total intrinsic angular momentum; N_s is the number of strange quarks in the hadron according to the quark constituent model; and $E_{bind} = M_h - \sum_i m_{q_i}$ is the hadron binding energy. A list of fitted parameters for equation (3.9) is given in Table 3.3.

Parameters	$\sqrt{s} = 91$ GeV	Simultaneous Fit
γ_s	0.29 ± 0.03	0.29 ± 0.02
Δm (GeV)	0.150 ± 0.029	0.161 ± 0.024
T (GeV)	0.289 ± 0.020	0.298 ± 0.015
$C_{\sqrt{s}}$	0.209 ± 0.041	$C_{91} = 0.218 \pm 0.034$ *
C_B	10.0 ± 1.0	11.0 ± 0.9
χ^2/dof	56.2/19	155.8/57

* $C_{30} = 0.124 \pm 0.020$, $C_{10} = 0.049 \pm 0.008$

Tab. 3.3: Fit values for LEP data and to data at different center-of-mass energies.

The observed rate of hadrons depends on the number of primary hadrons produced, described by equation (3.9), and on the number of hadrons produced from decays, so-called "feed-down." Feed-down can be computed by predicting all of the primary hadron production, and then computing the decay contributions for all hadrons up to a mass of 2.5 GeV from measurements in the Particle Data Book [15]. Hadron masses above 2.5 GeV have sufficiently small production rates to be neglected, an exception to which are hadrons produced directly from c and b quark production (discussed in [14]).

---

[7] Primary hadrons are those which arise directly from the transition of quarks into confined particles. The quark flavor distribution of the inital $q\bar{q}$ pair affects hadron production rates and is accounted for separately [14].

[8] The values of the strange quark constituent mass m_s and the up and down constituent masses are also needed. The assumptions and definitions used for Table 3.3 are that $m_s = 0.5$ GeV, $m_u = m_d$ and $\Delta m = m_s - m_u$.

3.4 Hyperon Decay

The properties of hyperon decay are accurately parameterized by a phenomenological interaction density [16],

$$\mathrm{H}_{\mathrm{int}} = \underbrace{\phi_\pi^\dagger \bar{\Psi}_{\mathrm{p}}(\mathrm{g} + \mathrm{g}'\gamma_5)\Psi_\Lambda}_{\Lambda \to \mathrm{p} + \pi^-} + \underbrace{\bar{\Psi}_\Lambda(\mathrm{g}^* - \mathrm{g}'^*\gamma_5)\Psi_{\mathrm{p}}\phi_\pi}_{\bar{\Lambda} \to \bar{\mathrm{p}} + \pi^+}$$

where the two terms correspond to Λ and $\bar{\Lambda}$ decay, respectively.

Parity non-conservation in hyperon decays, which is present in $\mathrm{H}_{\mathrm{int}}$ when both g and g′ are non-zero, was experimentally discovered in 1957, following the insight of T.D. Lee and C.N. Yang. A consequence of parity violation is the possibility to measure the polarization of hyperons based on decay-angular distributions.

The polarization observable, $\langle \vec{\mathrm{s}}_\Lambda \rangle \cdot \vec{\mathrm{p}}$, changes sign under a parity transformation. The specific implication is that the hyperon decay rate will have a polarization dependence on the decay-angular distribution of the pion.

$$\frac{d\sigma_\Lambda}{d(\cos\theta_\pi)} \propto 1 + \mathcal{P}_\Lambda \cdot \alpha_\Lambda \cdot \cos\theta_\pi \tag{3.10}$$

where $\mathcal{P}_\Lambda$ is the magnitude of the polarization. The measured values of α for several hyperons are given in Table 3.4.

Hyperon		α
Λ	$\to \mathrm{p}\pi^-$	0.642 ± 0.013
	$\to \mathrm{n}\pi^0$	0.65 ± 0.05
Σ^+	$\to \mathrm{p}\pi^0$	$-0.98^{+0.017}_{-0.015}$
	$\to \mathrm{n}\pi^+$	0.068 ± 0.013
	$\to \mathrm{p}\gamma$	-0.76 ± 0.08
Σ^-	$\to \mathrm{n}\pi^-$	-0.068 ± 0.008

Tab. 3.4: Hyperon Decay Parameters

4. PARTICLE ACCELERATION AND COLLISION

4.1 The Large Electron-Positron(LEP) Collider

The design criteria for the LEP Collider were largely influenced by the opportunity to study in detail the properties of the massive particles responsible for electroweak interactions. In particular, a machine achieving electron-positron collision energies of approximately 100 GeV would be capable of studying the production and decay of the Z^0 particle. At 200 GeV, the pair production of W^+W^- could be observed. These two goals were achieved after the machine was constructed in 1989. Some of the line-shape data collected by the L3 Experiment from e^+e^- collisions produced by LEP from several years of operation is displayed in Figure 4.1.

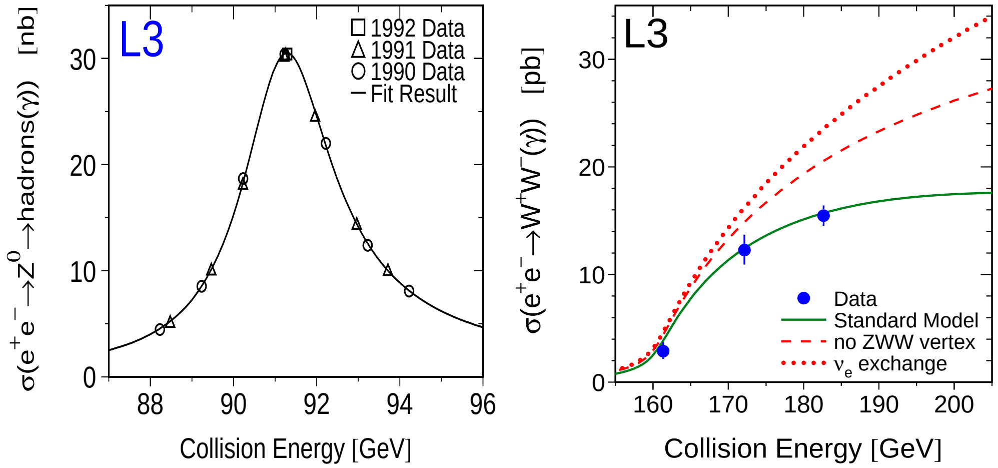

Fig. 4.1: **L3 Cross-Section Measurements for Z^0 and W^+W^- Production.**

LEP is a circular collider, building upon the existing system of circular accelerators operated at CERN. There are four experiments situated around the 27 km circumference of the LEP ring. These are L3, ALEPH, OPAL and DELPHI. Their relative locations can be seen in Figure 4.2.

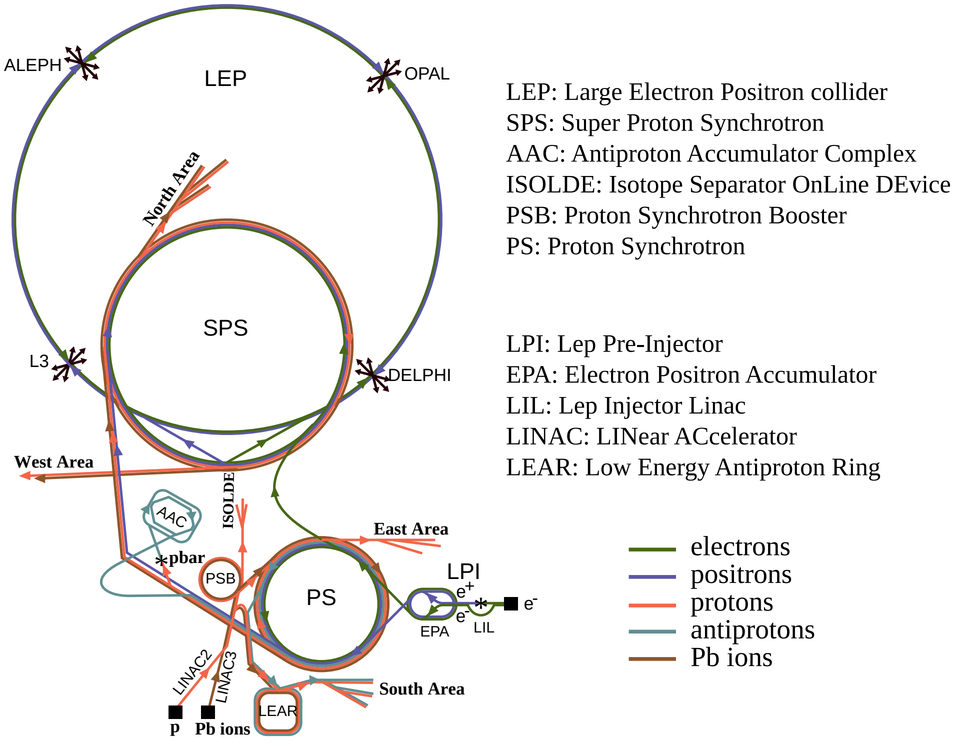

Fig. 4.2: **CERN Accelerator Complex**

The acceleration to the final collision energies achievable by LEP proceeds first through a chain of multi-purpose accelerators, generally referred to as the injector chain.

4.1.1 LEP Injector Chain

The LEP injector begins with two linear accelerators in tandem: a high-current 200 MeV electron linac, used for positron production, followed by a lower-current linac for accelerating electrons and positrons to 600 MeV prior to injection into the Electron-Positron Accumulator(EPA). The linacs produce a 12 nanosecond pulse of positrons (or electrons) every 10 milliseconds. These pulses are accumulated into 8 bunches of particles which circulate in the EPA. Since positrons need to be created from electron collisions with a target, positrons are accumulated 10 times slower than electrons.

After 10 seconds of positron accumulation, the bunches are transferred to the Proton Synchrotron(PS) accelerator. These are accelerated to 3.5 GeV before injection into the Super Proton Synchrotron(SPS)[1]. The SPS accelerates up to 20 GeV and then transfers the electron and positron bunches into LEP. The filling rate is roughly 0.25 milliAmps/minute and the total currents accelerated by the LEP machine is about 2 milliAmps of positrons colliding with 2 milliAmps of electrons.

4.1.2 LEP Main Ring

In the LEP main ring, the system of acceleration is based on the radio-frequency oscillation of electric fields within conducting (and superconducting) cavities. As electrons pass through a cell of a cavity, the electric fields are timed to oscillate in a direction of acceleration (see Figure 4.3 for a picture of LEP copper RF cavities). A corresponding timing is also present for the positrons, which counter-circulate in the same beam pipe as the electrons. The time interval referring to a period of RF electric field oscillation is called an "RF bucket."

There are an integral number of RF buckets in the LEP machine. The number is 31320, and the frequency of oscillation is 352.2 MHz. The RF buckets are the basic building block for setting up the timing of collisions at the interaction points of the four LEP experiments. Several timing schemes were using during the 1994 and 1995 years of operation, as shown in Table 4.1.

# of Bunches	Bunch Spacing μs (RF Buckets)	# of Bunchlets[2]	Bunchlet Spacing μs (RF Buckets)
8	11μs (3915)	1	–
4	22μs (7830)	1	–
4	22μs (7830)	4	0.25μs (87)

Tab. 4.1: LEP Accelerator Timing Schemes During 1994 and 1995.

---

[1] An amazing aspect of the CERN accelerator complex is the ability of the SPS to handle an electron and positron injection momentum of 3.5 GeV by setting the bending fields down to roughly 158 Gauss, while one second before they were set at 18000 Gauss during proton acceleration for the North Hall and West Hall fixed-target experiments. The cycling of particles through the machines is called the SPS Super-Cycle, which has a period of about 15 seconds.

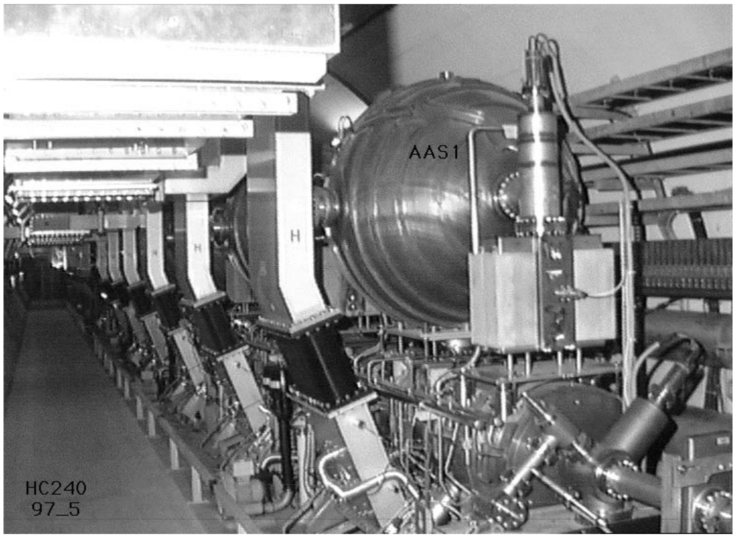

Fig. 4.3: **LEP Copper RF Cavities.** The evacuated beam pipe containing the electron and positron beams is located in the right bottom of the picture before it passes into a series of copper RF cavities. The waveguides feeding the RF cavities from the left are connected to a nearby Klystron.

4.2 The L3 Experiment

The L3 Experiment is positioned at one of four main interaction points of LEP. It was constructed by a group of physicists, technicians and engineers from 16 different countries from around the world [17]. The leader of the collaboration is Samuel C.C. Ting. The operation of the detector began with the startup of LEP in 1989 and has continued through 1997.

Two of the most visible features of the detector design are the large-volume electromagnet[3] which houses the experiment and a long stainless steel support tube. The support tube suspends all of the detector components in mid-air along the central axis of the magnet, as seen in Figure 4.4. What is called the "L3 Detector" is actually a collection of many individual sub-detectors, each designed to make specialized measurements. These components are drawn in Figure 4.5.

---

[2] Bunchlets are a sub-structure of a normal bunch, sometimes called "bunch trains."

[3] Listed in the 1997 Guinness Book of Records as the World's Largest Electromagnet.

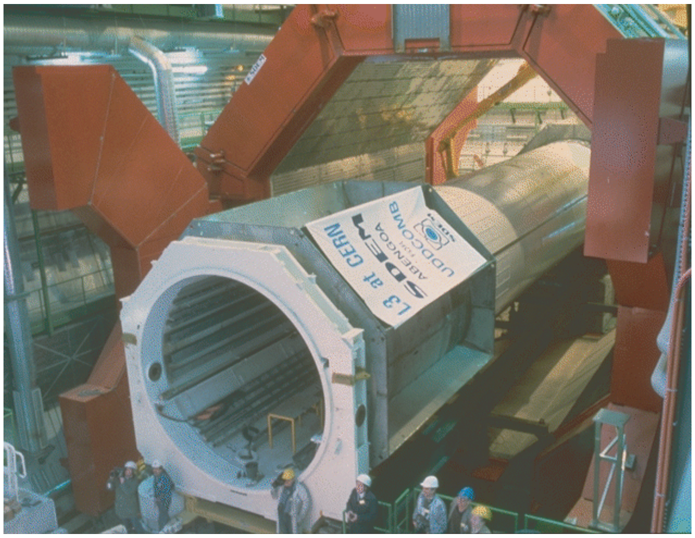

Fig. 4.4: **The L3 Magnet and Support Tube During Installation.**
In this picture, the doors of the magnet are open, and the newly installed support tube has been positioned along the center of magnet.

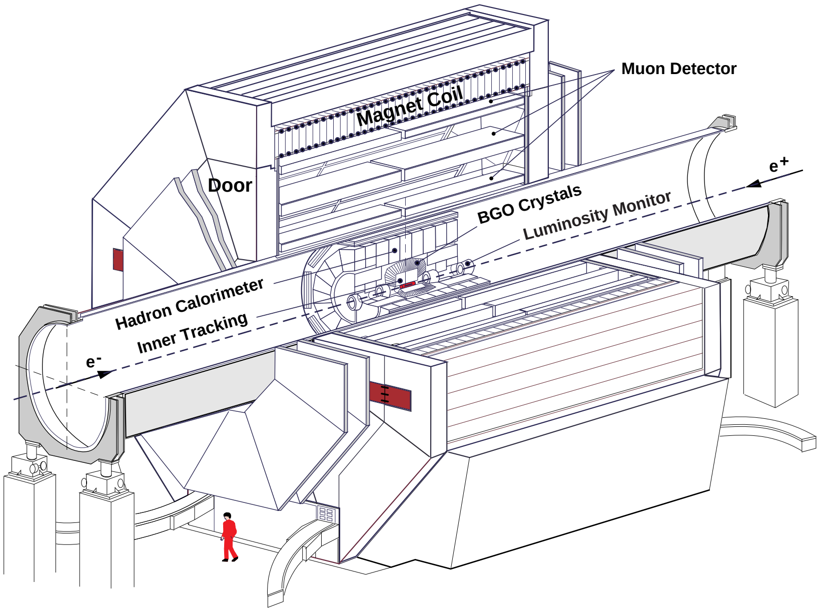

Fig. 4.5: **Perspective View of the L3 Sub-Detectors.**

4.2.1 Sub-Detectors of the L3 Experiment

Here is a list of the principal detector sub-systems and their function:

- **Inner Tracking Detectors**. Charged particles originating directly from the e^+e^- interaction point, or soon after, will have their trajectories measured by the inner tracking detectors.
    - *Silicon Micro-Vertex Detector.* Records accurate position information immediately outside the beam pipe volume.
    - *Time-Expansion Chamber.* Measures the curvature of charged tracks bending under the action of the solenoidal magnet field.
    - *Z-Chamber.* Determines how far forward or backward a charged particle has travelled before leaving the volume of the inner tracking detectors.
- **Electromagnetic Calorimeter(ECAL)**. A homogeneous scintillating crystal calorimeter composed of Bismuth Germanate ($Bi_4(GeO_4)_3$), generally referred to as BGO. Measures the total energy of electrons, positrons and photons. In addition, it acts as the first nuclear interaction length for combined energy measurements with the HCAL.
- **Hadron Calorimeter(HCAL)**. Consists of uranium absorber plates instrumented with proportional wire chamber readout. Measures the energy of pions, protons and other strongly interacting particles by sampling showering particles in between layers of absorber plates.
- **Muon Chambers**. Muons pass through the many tons of BGO, uranium and steel to leave a charged track in these chambers.
    - *Barrel Chambers.* Three layers of drift chambers mounted on the exterior of the support tube. Measures the curvature of muon tracks due to the magnetic field of the solenoid.
    - *Forward/Backward Chambers.* Muons travelling through the doors of the magnet are bent by a toroidal magnetic field. These chambers measure the amount of deflection to determine the momentum of the muon.
- **Scintillation Counters**. Positioned between the ECAL and HCAL, they determine the time at which particles have passed through the counters to sub-nanosecond precision. Used for cosmic muon rejection and LEP bunchlet tagging.

- **Luminosity Monitor**. Designed primarily to detect electron-positron scattering at small angles, it provides a high-statistics measurement of the collision luminosity of the LEP beams [18].

4.2.2 Trigger and Data-Acquisition System

Essential to the operation of the experiment is a system which determines whether or not a particle has been detected by one of the sub-detectors. Following initial particle detection, a decision is made as to whether the detector should record the information measured about this particle and potentially other particles which have interacted with the detector. This system is called the trigger and data-acquisition [19]. A decision is made every time the LEP beams are brought into collision. The amount of time to make the level-1 trigger decision is less than the time between bunch-crossings (see Table 4.1 for bunch spacings). Further reductions in the number of recorded events are made by two additional levels of trigger logic. The final rate of events recorded to tape during high-luminosity LEP running is roughly 5 Hz.

5. TRACKING AND CALORIMETRY

A photographic camera records an image by a technique that depends on how visible light interacts with a chemical emulsion. In the same way, a particle detector uses the interactions of long-lived particles, not specifically visible light, to form a picture of what has happened in a high-energy collision. In particular, charged pions, protons and anti-protons, and photons are detected by the tracking and calorimetry. Detector readings are translated into measurements by anticipating the pattern of readings expected from individual particles and groups of particles.

5.1 Tracking

5.1.1 Ideal Trajectories

A charged particle moving in a uniform magnetic field will follow the path of a helix in space. A convenient form for describing this trajectory is given by the following equations (J. Alcaraz, L3 Note 1666).

$$\begin{gathered} x = x_r - \delta \sin\phi_0 + s \cdot \mathrm{sinc}(\frac{C \cdot s}{2}) \cos(\phi_0 - \frac{C \cdot s}{2}) \\ y = y_r + \delta \cos\phi_0 + s \cdot \mathrm{sinc}(\frac{C \cdot s}{2}) \sin(\phi_0 - \frac{C \cdot s}{2}) \qquad (5.1) \\ z = z_0 + s \cdot \tan\lambda \end{gathered}$$

These functions define five quantities (C,ϕ_0,δ,$\tan\lambda$,z_0) which must be determined from the measurements made by the tracking system. The parameterization is in three independent variables (x,y,z) that represent a position in space. The variable s is an arc length in the (x, y)-plane. The coordinate (x_r,y_r) is used as a reference from which to compute δ and ϕ_0.

5.1.2 The Geometry of the Tracking Detectors

Charged particles originating from within the beam pipe will traverse three different tracking detectors before reaching the calorimetry. These are the Silicon Micro-Vertex Detector(SMD), the Time Expansion Chamber(TEC) and the Z-Chamber, as shown in Figure 5.1. Each tracking detector measures coordinates along the trajectory of the charged particle. The position resolution changes from 300 μm in the Z-Chamber, to 60 μm in the TEC, to 10 μm in the SMD. This follows the progressive importance of extrapolating the measured track back to its production vertex.

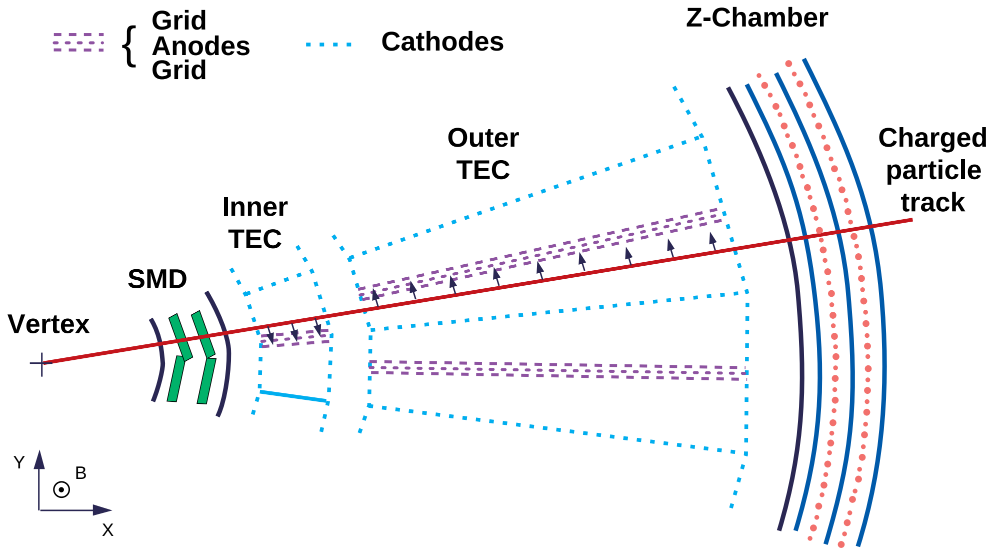

Fig. 5.1: **The Inner Tracking Detectors of the L3 Experiment.** A charged particle produced within the beam pipe will first cross the SMD, then the TEC, and finally the Z-Chamber before hitting the calorimetry.

5.1.3 Tracking Measurements

A charged particle suffers energy loss due to ionization as it travels through materials. The precision by which the position of ionization can be determined within a gas or silicon substrate is the intrinsic resolution of the tracking detector. In a silicon detector and in a gas-filled strip chamber, the strip pitch as well as the charge sharing on neighboring strips determines the intrinsic resolution. In a drift chamber, the situation is a bit more complicated. The position within the chamber is measured by the time it takes for ionization electrons to drift through the gas under the influence of an electric (and magnetic) field.

Silicon Micro-Vertex Detector

The SMD consists of 300 μm thin wafers of silicon with micro-strips of doped-silicon and metal implanted on both the top and bottom surfaces [20]. The micro-strips are accurately placed on the silicon wafer with the same technology made for electronic integrated circuits in chip fabrication. When a voltage bias is applied across the volume of the silicon wafer, electron-hole pairs created within the wafer when an ionizing particle passes through will be collected by nearby strips on both surfaces, as shown in Figure 5.2.

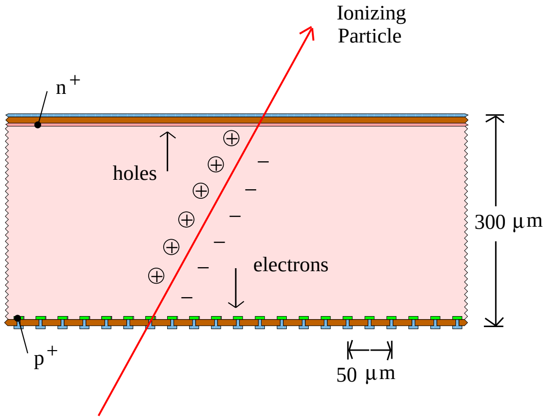

Fig. 5.2: **Charge Sharing on Neighboring Strips in the SMD.**
An ionizing particle passing through a silicon wafer will create electron-hole pairs in the interior of the silicon. Electrons are collected by strips on the bottom surface and holes by strips on the top surface.

Charged particles crossing the SMD will hit two layers of double-sided silicon. The orientation of the micro-strips on two surfaces is orthogonal. Since the wafer is very thin and carefully supported, a measurement of a coordinate from strips on the top and bottom surfaces can be accurately translated to a point in space along the trajectory of a charged particle. An important geometrical arrangement of the two layers of silicon greatly improves the pattern recognition of assigning the correct strip readings to a track, as seen in Figure 5.3.

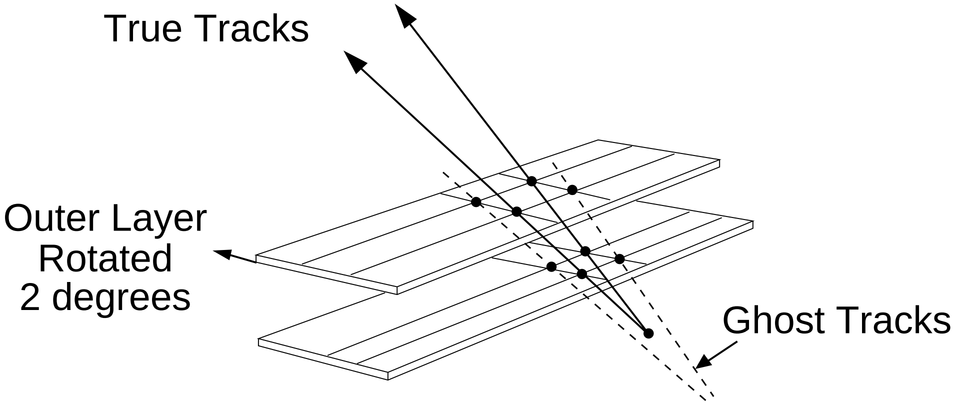

Fig. 5.3: **Stereo Arrangement of the Silicon Layers in the SMD.** The correct assignment of strip coordinates to charged particle tracks is aided by the 2 degree rotation of the outer silicon layer. An incorrect pairing of strip coordinates will cause a reconstructed track to point back to a different production point. The black lines drawn on each layer represent the micro-strip readings.

The grouping of strips in the readout of the SMD is optimized to reduce the number of readout channels while not deteriorating the intrinsic performance of the tracker. In particular, the angle at which an ionizing particle crosses a wafer changes the charge sharing on neighboring strips and therefore the accuracy of determining the strip coordinate. In low-angle regions, the number of z strips which are readout is reduced. The strip coordinate errors listed in Table 5.1 were determined from fits to the 1994 and 1995 data.

Time-Expansion Chamber

The tracking detectors are immersed in the uniform magnetic field of the L3 solenoid. This field points along the axis of the beam pipe. Therefore, charged particles traveling transverse to the beam pipe will follow a circular

Silicon Layer	Strip Coordinate Error[1](μm)	Readout Pitch Region
ϕ strips	10μm	50μm
z strips	$21\mu\text{m} \oplus 15\mu\text{m} \cdot \tan\lambda$ $21\mu\text{m} \oplus 26\mu\text{m} \cdot \tan\lambda$	150μm 200μm

Tab. 5.1: SMD Strip Coordinate Errors

path. The curvature C of this path is related to the transverse momentum $\mathrm{p_t}$ of the particle through the relationship,

$$\mathrm{p_t[GeV/c]} = \frac{\mathrm{B[kG] \cdot c[m/s] \cdot 10^{-13}}}{|C|}, \text{ where } C \text{ is measured in [1/mm].}$$

Curvature is the quadratic deviation from a straight-line trajectory; therefore, the accuracy with which it can be measured has a quadratic dependence on the span of the coordinate measurements made on a track.

The total lever arm available for coordinate measurements in the TEC is 31.7 cm radially with an additional 4.9 cm to the innermost SMD layer. To compensate for this relatively short lever arm, the TEC was specially designed to attain drift-distance measurements as accurate as 50 μm, one of the best ever achieved with a drift chamber. The technique relies on a low drift-velocity region complimenting an accurately described amplification region. These regions are drawn in Figure 5.4. An example of the achieved resolution measured in 1994 data is shown in Figure 5.5 for an outermost TEC wire.

5.1.4 Track Fitting and Error Propagation

Material effects within a tracking region are characterized by the angular deflection of a particle from multiple scattering,

$$\sigma_\theta = \frac{13.6 \text{ MeV}}{\beta \mathrm{cP}} \sqrt{\frac{X}{X_0}},$$

where X_0 is the radiation length of the material, X is the length of material traversed and P is the momentum in MeV/c of the particle. The particle velocity normalized to the speed of light, β, contains the multiple-scattering

---

[1] The symbol $\oplus$ indicates that the errors are added in quadrature.

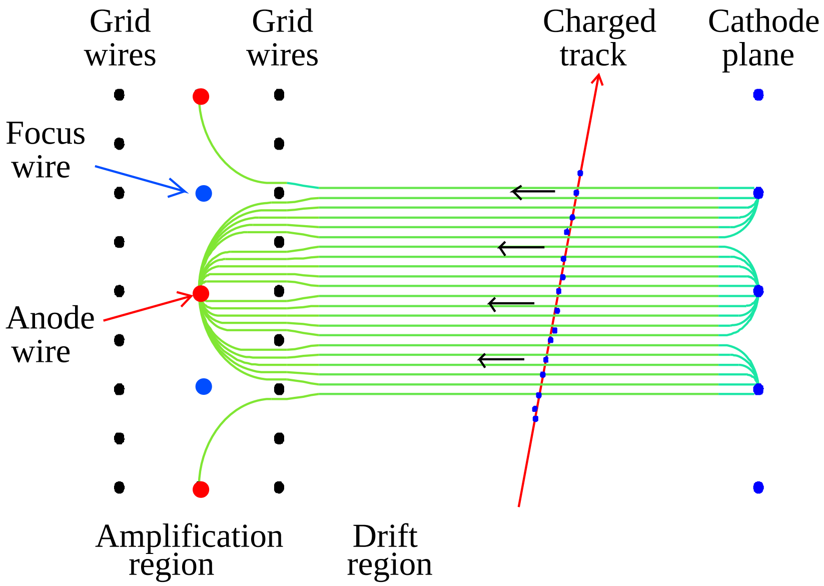

Fig. 5.4: **The Electric Field Lines of the Time-Expansion Chamber.** Electrons produced by ionization drift under the influence of a low-strength uniform electric field from the side of the Cathode towards the Grid wires. Electrons which pass the Grid wires enter a high electric field region and are focused onto an Anode wire. The timing measurements of when the first ionization electrons reach each of the Anode wires, relative to a Time Marker reference, are the principal measurements of the TEC.

dependence on the charged particle mass m.

$$\beta = \sqrt{\frac{\mathrm{P}^2}{\mathrm{P}^2 + m^2}}.$$

For P = 200 MeV/c, a proton has a factor of 4 larger contribution from multiple-scattering errors than a charged pion.

To perform track fitting in the presence of dense materials, a mathematical technique called Kalman filtering is used[2]. The Kalman filter needs both an initial estimate of the trajectory parameters of the track and the

---

[2] In 1958, R.E. Kalman developed an optimal solution for estimating linear dynamic systems in the presence of random Gaussian-distributed deviations. One of the first major applications of this technique was done by the Jet Propulsion Laboratory for the guid-

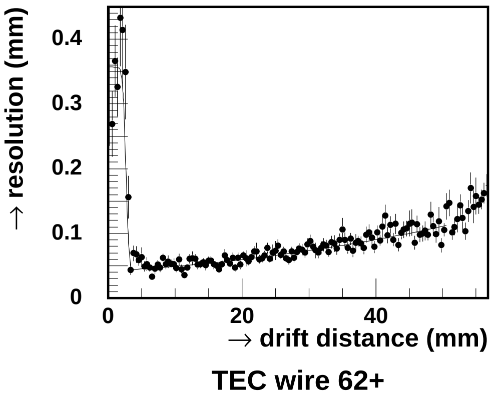

Fig. 5.5: **Time-Expansion Chamber Single Wire Resolution.** Electron diffusion in the gas causes large drift distance measurements to have increasingly larger errors.

measurement errors in the form of a covariance matrix. These estimates are provided by the TEC. The anode wire measurements are fit with the ideal trajectory equations (5.1), and the fit errors are used as an initial estimate of the covariance matrix.

The Kalman filter track fit proceeds through several steps. First, the extrapolation of the track back through the dense material layers located between the TEC drift volume and the beam pipe vacuum must be accurately computed[3]. In particular, the track trajectory parameters are allowed to change within the errors estimated from multiple-scattering between the TEC drift volume measurement and the SMD measured coordinates. Then, the Kalman filter iterates over the trajectory predictions and SMD measurements to determine the best error estimation and track extrapolation into the beam pipe vacuum, where the particle is assumed to originate.

5.1.5 Calculation of the Primary Vertex

When several particles originate from the same point in space, they are said to come from a common vertex. The location of this vertex can be computed from the intersection of the measured charged-particle trajectories. The primary vertex of a high-energy collision occurs within the beam pipe vacuum and specifically within the overlap of the electron and positron beam currents

---

ance system of the Ranger robot spacecrafts sent toward the Earth's moon in the early 1960's. Optimal combination of radar data with inertial sensor readings produced an overall trajectory estimate with a minimum expenditure of fuel.

[3] This calculation is performed by the GEANE package and makes use of a detailed description of the detector geometry and materials [21].

set by the LEP machine. The physical aperture over which the LEP beams are collided is called the "beam spot" (see Table 5.2).

LEP Beam Spot Size (μm)
$\sigma_x = 110\ \mu$m
$\sigma_y = 21\ \mu$m
$\sigma_z = 7000\ \mu$m

Tab. 5.2: LEP Beam Spot Size in 1994 and 1995

The calculation of the primary vertex[4] requires foremost a set of tracks which have accurate error estimations of their trajectory within the beam pipe vacuum. This is achieved with the Kalman filter, described in Section 5.1.4. The weeding out of tracks which do not belong to the primary vertex is done with a χ^2 probability calculation,

$$\chi^2_{N_{\mathrm{trk}}} = \sum_{i=1}^{N_{\mathrm{trk}}} \left(\vec{t}_i - \vec{f}(\vec{v},\vec{q}_i)\right)^T G_i^{-1} \left(\vec{t}_i - \vec{f}(\vec{v},\vec{q}_i)\right) + (\vec{v} - \vec{v}_{\mathrm{fill}})^T\, V_{\mathrm{fill}}^{-1}\, (\vec{v} - \vec{v}_{\mathrm{fill}})$$

where $\vec{t}_i$ is the vector of measured parameters for the i^{th} track and G_i the corresponding covariance matrix; $\vec{f}(\vec{v},\vec{q}_i)$ are the predicted measurements assuming the track originated from the vertex $\vec{v}$ with momentum $\vec{q}_i$; and $\vec{v}_{\mathrm{fill}}$ is the fill-vertex[5] with V_{fill} describing the size of the beam spot. The dimension of $\vec{t}_i$ is 5, corresponding to the 5 measurements (C,ϕ_0,δ,$\tan\lambda$,z_0) of the ideal trajectory equations (5.1).

For each track the probability $P_i = P(\chi^2_{N_{\mathrm{trk}}} - \chi^2_{N_{\mathrm{trk}}-1})$ is computed, and if either the probability of the vertex fit, $P(\chi^2_{N_{\mathrm{trk}}})$, is below 4% or any P_i is below 2%, the track with the lowest P_i is removed. The fit procedure is iterated until no track needs to be removed. If, in the end, less than three tracks remain, no primary vertex is computed.

---

[4] The primary vertex calculation is the work of Gerhard Raven (L3 Note 2108).

[5] The LEP machine is periodically filled with electron and positron beams, see Section 4.1.1. A single fill provides enough collision luminosity to last typically 8 hours. The fill-vertex is the average vertex position determined over this interval.

5.2 Calorimetry

5.2.1 Electromagnetic Showers

Photons with an energy more than an order of magnitude larger than the mass of an electron[6] will interact with dense matter primarily through the process of electron-positron pair production. Similarly, electrons and positrons will interact with atomic nuclei to radiate photons through the bremsstrahlung process, as shown in Figure 5.6. These processes occur roughly once per every radiation length of material encountered, and the particles produced in these interactions will also interact with the material. As both pair production and bremsstrahlung involve one particle coming in and two going out, the total number of interacting particles increases geometrically.

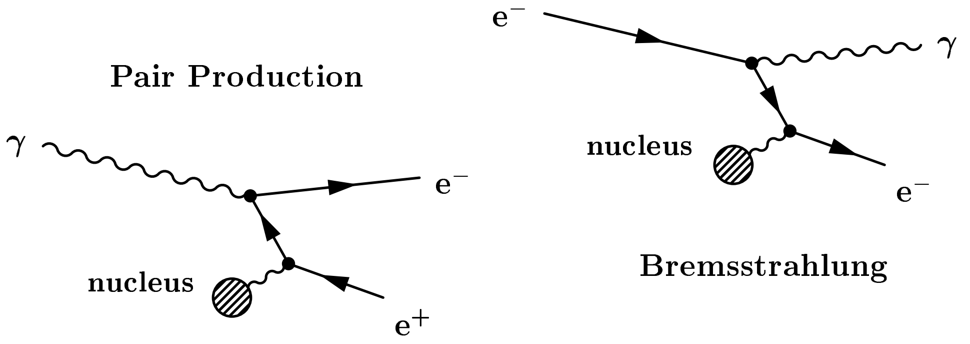

Fig. 5.6: **Electromagnetic Shower Development.**
The processes responsible for electromagnetic shower proliferation in dense materials are pair production and bremsstrahlung.

The proliferation of photons, electrons and positrons produced from pair production and bremsstrahlung is called an "electromagnetic shower." The energy of all the particles produced in a shower is eventually absorbed by atomic electrons once the interaction energies are below twice the electron mass. Direct interactions with atomic electrons include Compton scattering, the photoelectric effect, low-energy electron-positron annihilation and ionization loss [22].

---

[6] Masses and energies can be directly compared when expressed in units where the speed of light is equal to 1, from Einstein's $E = mc^2$.

5.2.2 The Geometry of the Electromagnetic Calorimeter

Surrounding the inner tracking system of the SMD, TEC and Z-Chamber is an electromagnetic calorimeter composed of Bismuth Germanate(BGO). A total of 10734 individually instrumented BGO crystals are arranged to form two half-barrels and two endcaps, as shown in Figure 5.7.

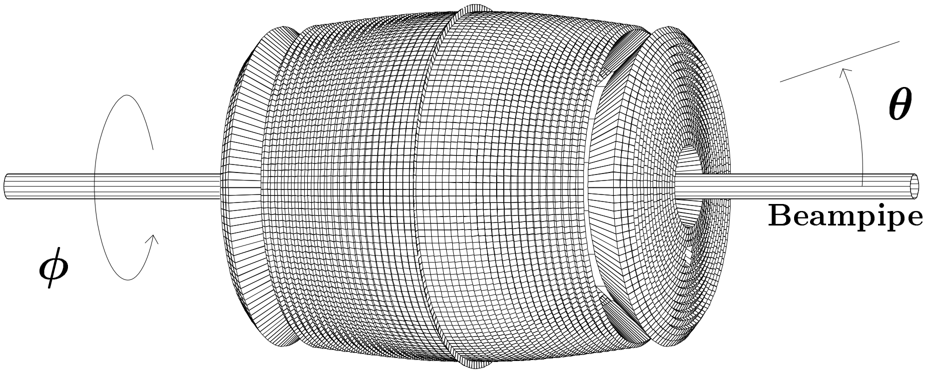

Fig. 5.7: **BGO Electromagnetic Calorimeter Geometry.**

One of the purposes of the BGO detector is to measure the energy of photons produced within the beam pipe or tracking volume. The BGO crystals point almost directly towards the primary interaction region[7] and provide more than 21 radiations lengths of stopping power for electromagnetic showers.

In a BGO crystal, the passage of low-energy electrons and positrons through the crystal lattice causes short-lived excitations in the system of lattice electrons. The special property of these crystals is that the de-excitation of lattice electrons can generate green light. As the crystal is optically transparent, the number of scintillation photons can be counted with photodiodes attached to the surface, and the amount of scintillation can be used to compute the energy of the electromagnetic shower.

---

[7] The BGO crystals in the barrel point away from the primary vertex in azimuthal angle to prevent particles from traveling down the cracks between adjacent crystals. The BGO endcaps were never fully pushed up against the barrel and therefore are non-pointing. This was done to keep the endflange of the tracking detector from shadowing the barrel and to make space for the tracking cables to pass between the BGO barrel and endcap.

5.2.3 The Electromagnetic Shower Shape

The spatial extent of an electromagnetic shower has a characteristic lateral size, as can be seen in Figure 5.8. The mean percentage of containment in the central-most crystal of a shower is roughly 75%. The remaining portion of the shower energy is mainly distributed in neighboring crystals. However, some energy is lost in the support material between crystals and in the case of electromagnetic showers below 1 GeV, front-end leakage of the shower becomes significant, as discussed in Section 5.2.4. Rear-end leakage, however, is below 1% even for 50 GeV showers.

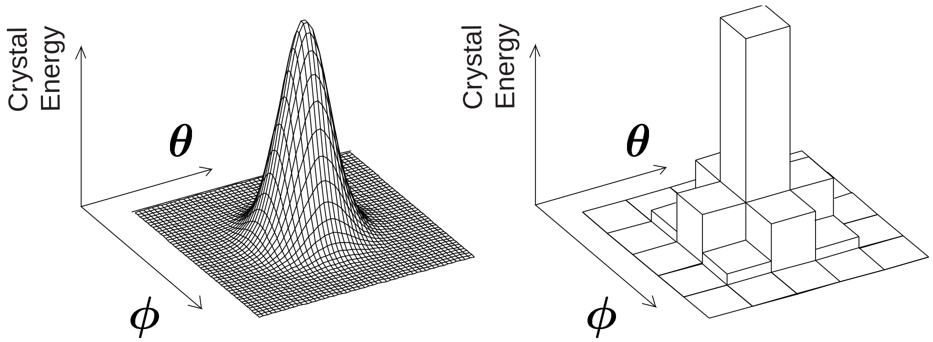

Fig. 5.8: **Electromagnetic Shower Shape in the BGO.**
On the right is the distribution of energy measurements expected in each crystal from an electromagnetic shower centered on an array of 25 BGO crystals. On the left is the continuous lateral distribution of energy deposition expected in a single crystal. (The amount of energy deposition expected at a point in the integral over the volume of a crystal.) This distribution is known as the transverse "shower shape."

The distribution of energy measurements in crystals surrounding the central-most crystal is the only means of identifying electromagnetic showers. Once identified, more precise information can be computed about the shower, such as better position and energy measurements.

5.2.4 Statistically Determined Errors on Energy and Angular Measurements

The BGO calorimeter stands prominently as the most accurate photon detector at LEP. The behavior of the measurement errors with photon energy and angle is simply described and lends itself to statistical parameterization.

The first resolution function to be studied was the energy resolution in the barrel region. The high-energy performance of the barrel was studied extensively in the years 1987-1988 in the CERN X3 test beam line and with simulation [23]. These measurements were performed at 2, 10, 20 and 50 GeV. Below 2 GeV, the resolution curve was supplemented with ideal[8] simulation data for π^0 photons in hadronic decays of the Z^0. An important aspect of low-energy photon measurements can be seen in Figure 5.9. Namely, there are two distinct energy resolution functions, one for the upper-edge and one that describes the tailing distribution.

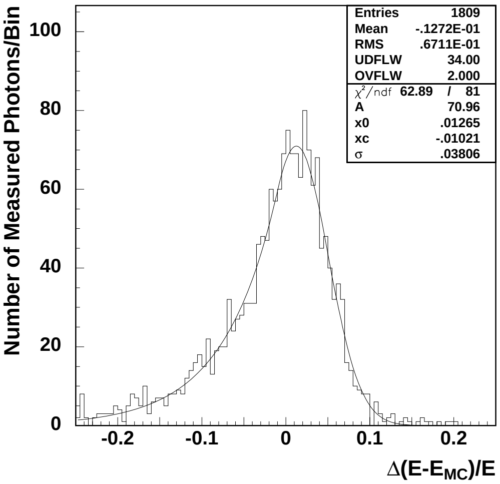

Fig. 5.9: **Front-End Leakage.** The distribution of the fractional error in 200 MeV photon energy measurements shows a tail toward low energy.

In order to match up with the already well-measured Gaussian error distributions at high-energy, a split function was used to fit the width of the photon energy distributions [24],

$$f(x) = \begin{cases} A\exp[-a(x-x_0)^2] & \text{if } x \geq x_c \\ B\exp[b(x-x_0)] & \text{if } x < x_c \end{cases} \tag{5.2}$$

where $a = 1/(2\sigma^2)$, $b = -2a(x_c - x_0)$ and $B = A\exp[a(x_c - x_0)^2]$. This leaves four free parameters, the three parameters (A, x_0, σ) for a Gaussian upper-edge fit and one parameter (x_c) which splices in an exponential tail continuously and which is smooth in the first derivative. A combined fit of

---

[8] Ideal running conditions means in this case, no calibration errors, perfect linearity, no electronic noise, no missing channels and a fixed energy threshold of 2 MeV for all crystals.

the X3 data and the Gaussian error from the supplemental data results in a resolution function which is the same as the resolution function of the X3 data alone,

$$\sigma_E^{\text{Gaussian}}(E)/E = \frac{1.57\%}{\sqrt{E}} + 0.34\%.$$

To account for the tailing distribution on the lower side, the RMS was computed of the fit function (5.2) for several energies. This results in a more accurate resolution function for low energies,

$$\sigma_E^{\text{Full}}(E)/E = 3.42\% \exp[-\frac{E}{0.854}] + \frac{1.57\%}{\sqrt{E}} + 0.34\%. \tag{5.3}$$

Both the Gaussian and full energy resolution functions[9] are plotted in Figure 5.10.

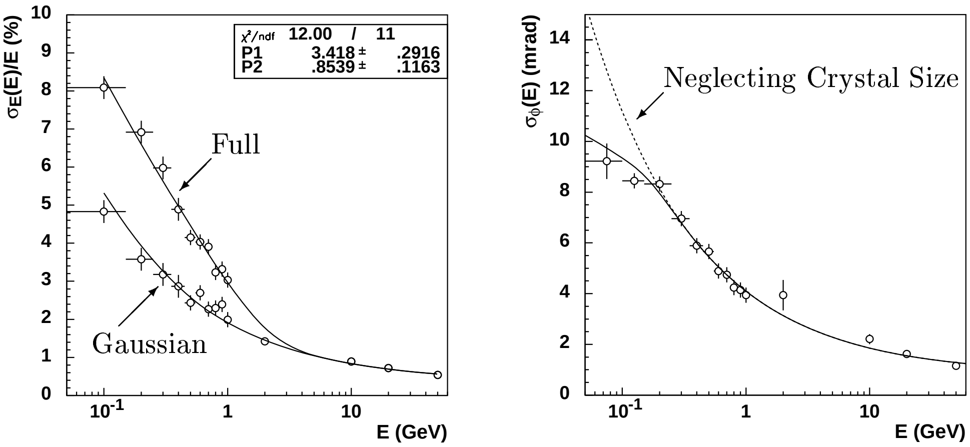

Fig. 5.10: **BGO Resolution Functions in Energy and ϕ-Angle.**
On the left are the two curves describing the energy resolution in the BGO barrel. On the right is the ϕ-resolution function in the barrel.

The second resolution function to be studied was the ϕ-angular resolution function in the barrel. The data from X3 at 2, 10, 20 and 50 GeV was

---

[9] To avoid underflows, the low-energy exponential term should be set to zero above 20 GeV.

supplemented with simulation data down to 50 MeV. An important effect found only below 200 MeV comes from the limiting angular resolution from the finite size of the crystal. Single-crystal photon measurements will have an angular resolution of 39 mrad/$\sqrt{12}$ = 11.3 mrad, the RMS of a flat distribution with 39 mrad being the average angular size of a crystal in ϕ. The ϕ-resolution function for all energies[10] was found to be,

$$\sigma_\phi(E) = \frac{3.28\ \text{mrad}}{\sqrt{E + E_c(E)}} + 0.82\ \text{mrad}, \tag{5.4}$$

with

$$E_c(E) = \frac{E_0}{1 + \exp\left[2\left(\frac{E - E_0}{E_0}\right)\right]}$$

and is plotted in Figure 5.10. The value $E_0 = 0.098$ GeV was determined from the limiting angular resolution and a fit to the data.

The θ-resolution function in the barrel and all of the endcap resolution functions are summarized in Appendix A.

5.2.5 Gain and Offset Calibration of the Electronics

The wide range of energies measured by the BGO calorimeter is digitized with a floating-point ADC[11]. The basic principle behind a floating-point ADC is to use an accurate N-bit ADC, with a short conversion time, to cover a dynamic range of signals which is larger than N bits. This is done by making several copies of the signal with different linear amplifications. The copy which has the highest amplification but is still within the range of the N-bit ADC will have the least digitization error. The digital readings, therefore, have N bits of mantissa from the ADC, and a few bits to record which signal amplification was used for digitization. This format is commonly known as a floating-point representation.

The calibration of the gains and offsets internal to each floating-point ADC matches up the different linear amplification regions to produce an overall linear response for the full range of input signals. The design of the BGO ADCs uses an accurate 12-bit ADC with a 220 μs conversion time to

---

[10] To avoid underflows, the function E_c should be set to zero above 2 GeV.

[11] Name coined by R. Sumner, formerly of Princeton University. Further designs of the Floating-Point Unit were invented by P. Denes, Princeton University.

cover 21 bits of dynamic range with 6 different linear amplifications[12]. A passive split of the signal after the preamp separates the lower three and higher three signal gains as the high-energy and low-energy channels, respectively. When the input signal for a particular amplification approaches the maximum voltage of the 12-bit ADC, the next lower amplification is used for digitization. The energy equivalence of the transition between gains within the floating-point ADC has a spread which depends on the gain calibrations, offsets, pedestals and energy calibrations. The distribution of transition energies is plotted in Figure 5.11.

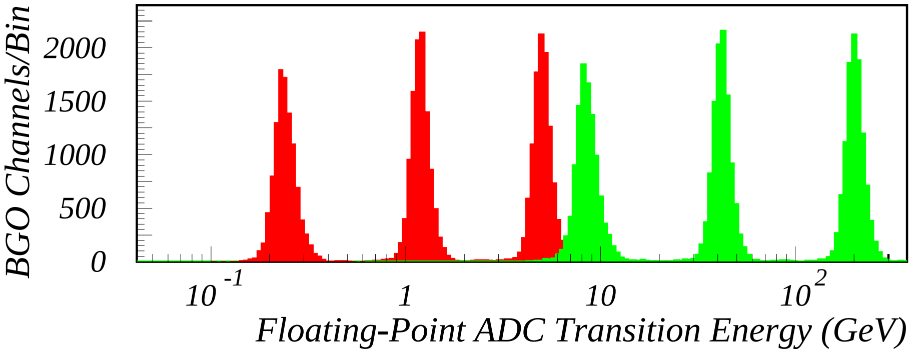

Fig. 5.11: **The BGO Floating-Point ADC.**
The distribution of transition energies for all the BGO ADCs. The three peaks on the left correspond to the low-energy channel. The three peaks on the right correspond to the high-energy channel, with the sixth peak indicating the maximum energy a single crystal can contain without saturating the ADC. The maximum energies are distributed around 200 GeV.

A method of relative gain and offset calibration of the floating-point ADC was incorporated as a special readout mode of the electronics, known as "bump" mode. In bump mode, the signal on the sample/hold is first digitized on the highest gain signal not saturating the ADC and then is digitized a second time on the next lower signal amplification. The droop on the

---

[12] The 6 different signal amplifications are approximately 1, 2^2, 2^4, 2^5, 2^7 and 2^9. The dynamic range of 21 bits is computed by summing the 12 bits from the ADC plus the 9 bits of maximal gain change. The digitization error is below 0.1%, even down to 80 MeV.

sample/hold is negligible, so the two readings provide a direct comparison between two different signal gains, as seen in Figure 5.12.

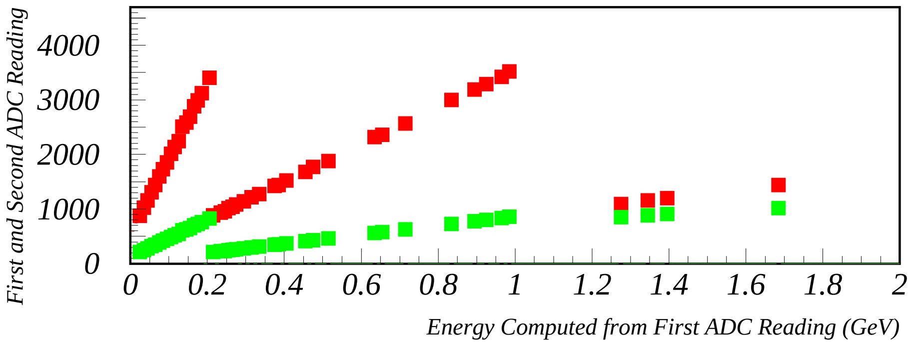

Fig. 5.12: **Bump Mode Data.**
For each ADC reading on the optimal gain, a second reading of the same signal is taken on the next lower gain. Data taken with a wide range of signal inputs allows for the relative gain and offset calibration of two successive internal gains of the floating-point ADC.

To calibrate, the BGO readout was put into bump mode during three LEP fills of Z^0 running in 1995. The combination of hadronic Z^0 decays and Bhabha data populated the full range of signal inputs. The re-measured gains and offsets were compared with the 1987 test set measurements, which are still currently in use (see Tables 5.3 and 5.4).

Side			G_{12}	G_{23}	G_{34}	G_{45}	G_{56}
RB24	Mean	(%)	-0.03	-0.02	-1.07	-0.01	-0.01
	RMS	(%)	0.09	0.07	1.50	0.24	0.08
RB26	Mean	(%)	-0.01	-0.01	-1.07	-0.01	0.00
	RMS	(%)	0.09	0.06	1.40	0.21	0.11

Tab. 5.3: **Bump Mode Gain Re-Calibration.**
The percentage change in the relative gains between the 1987 test set measurements and the 1995 Z^0 bump mode data is less than 0.1% for all gains except G_{34}. The increase of the BGO integration gate from 5 μs to 11 μs at the beginning of 1995 is believed to be the cause of this change.

Side			O_1	O_2	O_4	O_5
RB24	Mean	(ADC)	-0.72	-0.37	-0.1	0.0
	RMS	(ADC)	1.22	0.87	4.7	1.7
RB26	Mean	(ADC)	-0.15	-0.45	0.1	0.1
	RMS	(ADC)	1.40	0.83	4.8	1.6

Tab. 5.4: **Bump Mode Offset Re-Calibration.**
The change in offsets from 1987 to 1995 is less than 1 ADC count.

5.2.6 Energy Resolution and Linearity Measurements

The resolution functions derived in Section 5.2.4 neglected the effect of electronic noise, calibration errors and possible non-linearities in the energy measurement. The correction for electronic noise and energy linearity can be derived from the observed width and location of the mass peaks of the π^0 and η resonances measured in their two photon decay mode. The mass distribution for two photon combinations in hadronic decays of the Z^0 taken in 1995 is shown in Figure 5.13.

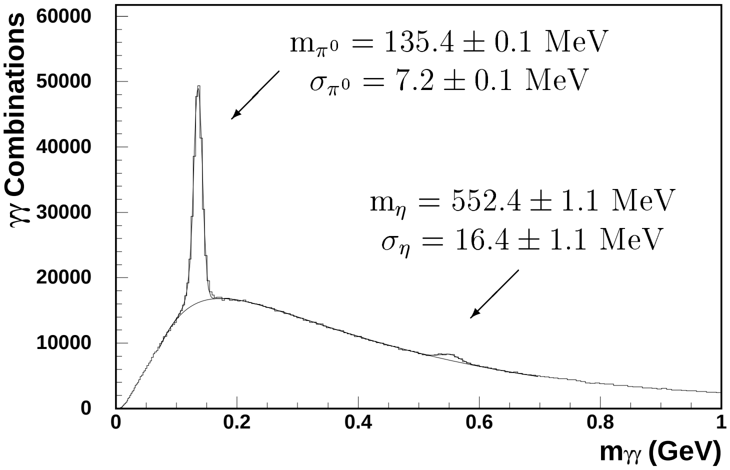

Fig. 5.13: **BGO Energy Linearity Measured with π^0 and η Resonances.** The difference in the width of the π^0 mass peak in data and Monte Carlo simulation is used as a measurement of the electronic noise contribution to the energy resolution. The photon energies in the 1995 data have been rescaled by a factor 1.039 in order to reproduce the mass peak locations for the π^0 and η determined in the Monte Carlo simulation.

The calibration errors and an additional linearity measurement can be determined from the observed width and location of the 45.6 GeV and 91.4 GeV electron peaks from Bhabha scattering measured in data taken in 1997[13]. The Bhabha peaks for these two beam energies are shown in Figure 5.14.

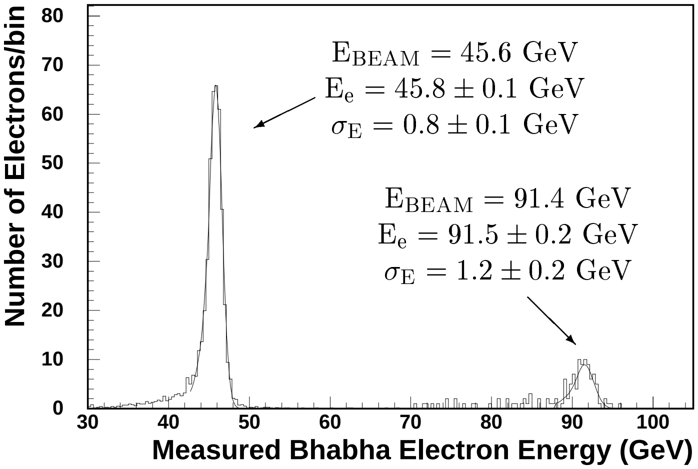

Fig. 5.14: **BGO Energy Linearity Measured with Bhabha Scattering.** The BGO energy calibration is adjusted every data-taking period to agree with the 45.6 GeV Bhabha peak. No further adjustment was needed to obtain less than 0.3% energy non-linearity for the 91.4 GeV high-energy Bhabhas. The width of the Bhabha peak is a measurement of the calibration errors.

The overall energy resolution function (5.3) is modified by the electronic noise and calibration error terms,

$$\sigma_E^{\mathrm{Full}}(E)^2 = \sigma_E^{\mathrm{Full}}(E)^2 + N_9 \cdot \sigma_{\mathrm{intrinsic}}^2 + (N_9 \cdot \sigma_{\mathrm{correlated}})^2 + (\sigma_{\mathrm{calibration}} \cdot E)^2 \quad (5.5)$$

with $\sigma_{\mathrm{intrinsic}} = 1$ MeV, $\sigma_{\mathrm{correlated}} = 1.6$ MeV and $\sigma_{\mathrm{calibration}} = 1.5\%$ in 1995 data-taking. A method for reducing the amount of correlated noise, which has been applied on all data taken since 1994, is described in Appendix B (C. Tully, L3 Note 1928). The BGO calibration is maintained with several

---

[13] The width of the 1995 Bhabha peak is slightly more narrow. The 1997 data provides a check of the energy linearity over a wide range of energies within the same calibration period. The measured Bhabha peaks in Figure 5.14 have been corrected for dead crystals and refit with an electromagnetic shower shape using methods developed by I.Kominis and I.Nemenman (L3 Note 2157).

monitoring systems [23]. A unique *in situ* calibration system based on an RFQ proton accelerator and a lithium target has provided accurate recalibration of the detector for several years [25].

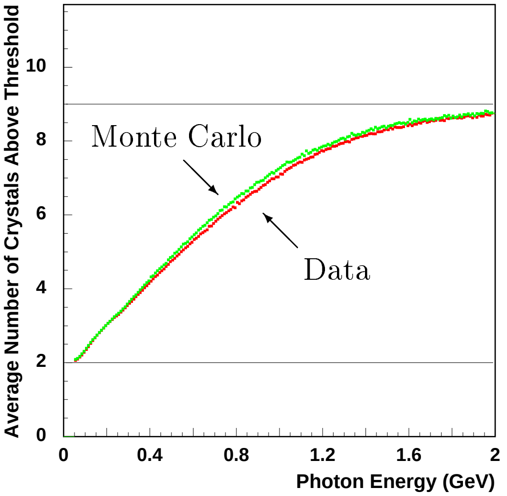

Fig. 5.15: **Readout Thresholds**. The number of crystals readout as a function of energy in the central 3×3 array of the photon shower is a measure of the energy thresholds. Below 50 MeV, the average number of crystals readout drops below 2. This is functionally the lowest energy shower which can reliably be identified as a photon.

The value of N_9 is the number of crystals above threshold in a 3×3 array centered on the electromagnetic shower. As the readout thresholds are set on a daily basis to keep up with external changes in the noise or ground conditions within the L3 detector, the static 3 MeV thresholds set in the Monte Carlo simulation are not a perfect description for computing N_9. A comparison of N_9 for 1995 data and Monte Carlo for selected photons is shown in Figure 5.15. The discrepancy in these distributions affects the accuracy of the energy resolution function (5.5).

6. BARYON PRODUCTION MEASUREMENTS

6.1 Secondary Vertices

Particle decays characterized by the presence of secondary vertices stand out among a background of long-lived particle tracks, as seen in Figure 6.1[1].

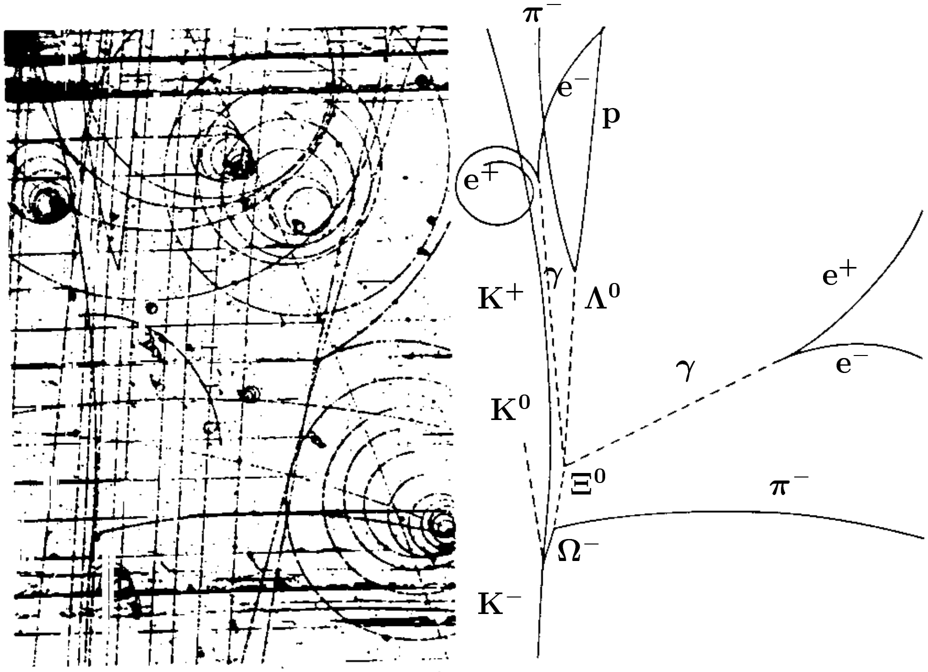

Fig. 6.1: **Evidence for the Ω^- Baryon.**
The Ω^- baryon, predicted from the SU(3) flavor model, was found in K^- beam bubble chamber experiments at Brookhaven in 1964 [1,26].

---

[1] This event was identified during scanning by N.P. Samios. Although the non-pointing Λ^0 and high transverse momentum π^- were the initial signatures for the Ω^-, the two converted photons from the π^0 decay unambiguously identified the decay $\Omega^- \to \Xi^0\pi^-$.

6.2 Kinematic Constraints

The application of external information to modify the direct measurements made by a detector or to perform hypothesis testing is, in general, referred to as "kinematic constrained fitting." The Ω^- decay in Figure 6.1 contains three secondary vertices constructed from two charged tracks, namely the two converted γ's and the Λ^0. The 3-dimensional opening angle between the two γ's can be determined by requiring them to originate from the same point and to form the mass of a π^0. A similar assumption can be made for the Λ^0 measurement. The numerical technique for constrained fitting is somewhat involved, but is included in Appendix C for reference.

6.3 Measurement of the $\mathbf{\Sigma^+}$ Baryon

The decay properties of the Σ^+ baryon have already been determined by previous experiments [15]. The decay mode $\Sigma^+ \rightarrow \mathrm{p}\pi^0$ with a branching ratio of 52% can be identified by combining measurements from the tracking and calorimetry.

Fig. 6.2: **Decay Kinematics.** The $\mathbf{\Sigma^+}$ baryon decays at the point $\vec{\mathbf{v}}_\mathbf{s}$.

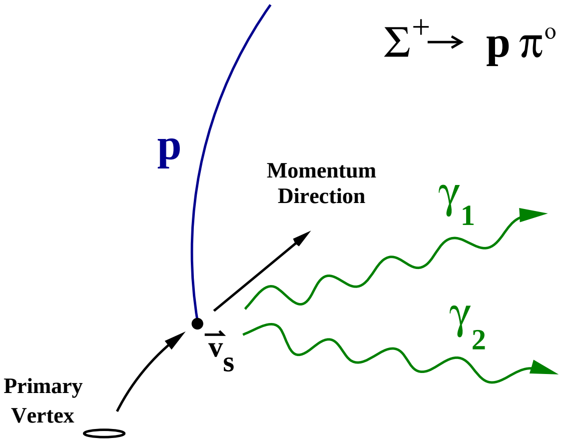

The signature of a $\Sigma^+ \rightarrow \mathrm{p}\pi^0$ decay is a single charged track and two photons measured in the calorimeter. If the decay point of the Σ^+ were known, the two photons would reconstruct to the mass of the π^0 within the error of the measurements. Similarly, at this decay point, the total momentum of the Σ^+ would be equal to the sum of the proton and π^0 momenta. These two pieces of kinematic information, in addition to the assumption that the Σ^+

is produced at the primary vertex, can be expressed as follows[2].

$$\vec{\mathbf{d}}'(\vec{\mathbf{v}}_\mathrm{s}) \times [\vec{\mathbf{p}}_\mathrm{p}(\vec{\mathbf{v}}_\mathrm{s}) + \vec{\mathbf{p}}_{\gamma_1}(\vec{\mathbf{v}}_\mathrm{s}) + \vec{\mathbf{p}}_{\gamma_2}(\vec{\mathbf{v}}_\mathrm{s})] = 0$$

$$\mathrm{m}_{\gamma_1\gamma_2}(\vec{\mathbf{v}}_\mathrm{s}) = \mathrm{m}_{\pi^0}$$

The computed probability for Σ^+ candidates to satisfy these constraints is plotted in Figure 6.3. The flatness of the signal distribution indicates accurate error estimation has been made for the measurements.

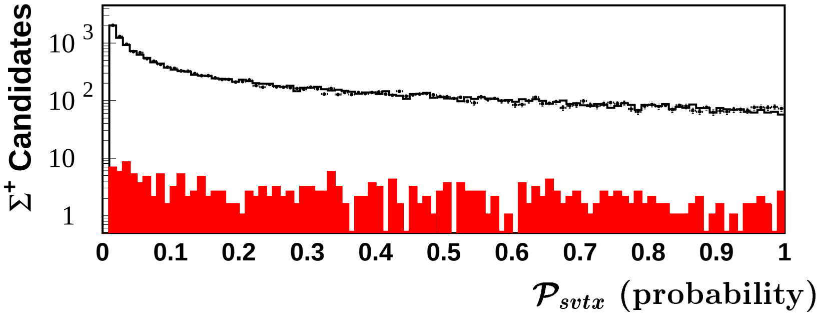

Fig. 6.3: **Computed Probability for $\Sigma^+ \to p\pi^0$ Decay Kinematics.** The agreement in data and Monte Carlo simulation is shown with the points and open histogram, respectively. The solid histogram is the distribution for true decays, based on Monte Carlo generator information.

The inclusive production rate measurement of Σ^+ baryons is based on a selection of hadronic Z^0 decays which have a measured primary vertex. The hadronic selection is similar to that used for electroweak line-shape measurements, and is based primarily on the observation of a well-balanced, high particle-multiplicity event with nearly the full collision energy measured by the calorimeters [27].

Hadronic Event Selection:

$\mathrm{E}_{\mathrm{perpendicular}}/\sqrt{\mathrm{s}} \leq 0.4$

$|\mathrm{E}_{\mathrm{longitudinal}}|/\sqrt{\mathrm{s}} \leq 0.4$

$\mathrm{N}_{\mathrm{clusters}} \geq 13$

$0.6 \leq \mathrm{E}_{\mathrm{total}}/\sqrt{\mathrm{s}} \leq 1.4$

---

[2] The vector $\vec{\mathbf{d}}'$ is the direction of flight of the Σ^+ at the time of decay. It is computed assuming a curved trajectory originating at the primary vertex.

The primary vertex, as described in Section 5.1.5, is constructed from the measured charged tracks in the event. The knowledge of the primary vertex in all three dimensions is important to the constrained fit calculations.

3D Primary Vertex Requirements:

- Includes tracks with SMD hits
- Kalman filtering performed on tracks
- At least 3 tracks remaining in fit

The selection criteria for $\Sigma^+ \to \mathrm{p}\pi^0$ can be separated into proton selection, photon selection and kinematic selection specific to the Σ^+.

The proton needs to have good or at least well-estimated transverse and longitudinal momentum measurements. To preferentially select protons from long-lived Σ^+ decays, the probability of the proton to belong to the primary vertex $\mathcal{P}_{\mathrm{pvtx}}$ is required to be small.

Proton Track Selection:

$\mathrm{SPAN}_{\mathrm{TEC}} \geq 10$ wires
SMD measured $\tan\lambda$ and z_0
$|\vec{\mathbf{p}}_{\mathrm{p}}| > 0.5$ GeV
$\mathcal{P}_{\mathrm{pvtx}} < 10^{-3}$
Not tagged as $\mathbf{\Lambda^0}$ or $\mathbf{K^0_s}$ track

Photons are identified by the properties of their electromagnetic shower in the BGO barrel calorimeter. Most of the electromagnetic selection is performed by an energy-dependent[3] cut on a single neutral network output F_{NN} (Y.J. Pei, L3 Note 1569). Electron rejection is done by eliminating showers which match with a charged track trajectory.

$\boldsymbol{\gamma}$ Bump[4] Selection:

$\mathrm{N}_{\mathrm{crystals}} > 1$
$|\cos\theta_\gamma| < 0.74$
$\mathrm{E}_{9\mathrm{CORR}} > 55$ MeV (${\mathrm{E}_{9\mathrm{CORR}}}$ is an approximation to E_γ)

---

[3] The energy-dependent cut on F_{NN} was developed by Howard Stone.

[4] The pattern of energy deposition of a photon in the electromagnetic calorimeter has a local maximum, or "bump," as shown in Section 5.2.3.

$$
\begin{aligned}
&\text{for } \mathrm{E_{9CORR}} < 0.93 \text{ GeV}, \\
&\qquad \mathrm{F_{NN}} > 0.3413 + 0.4 \cdot \mathrm{E_{9CORR}} \\
&\text{for } \mathrm{E_{9CORR}} \geq 0.93 \text{ GeV}, \\
&\qquad \mathrm{F_{NN}} > 0.7133 \\
&\text{if } |\phi_{\mathrm{TEC}} - \phi_{\mathrm{BGO}}|_{2\pi} < 5\,\sigma_{\phi_{\mathrm{BGO}}}, \\
&\qquad \text{then } |\theta_{\mathrm{TEC}} - \theta_{\mathrm{BGO}}| > 5\,\sigma_{\theta_{\mathrm{BGO}}}
\end{aligned}
$$

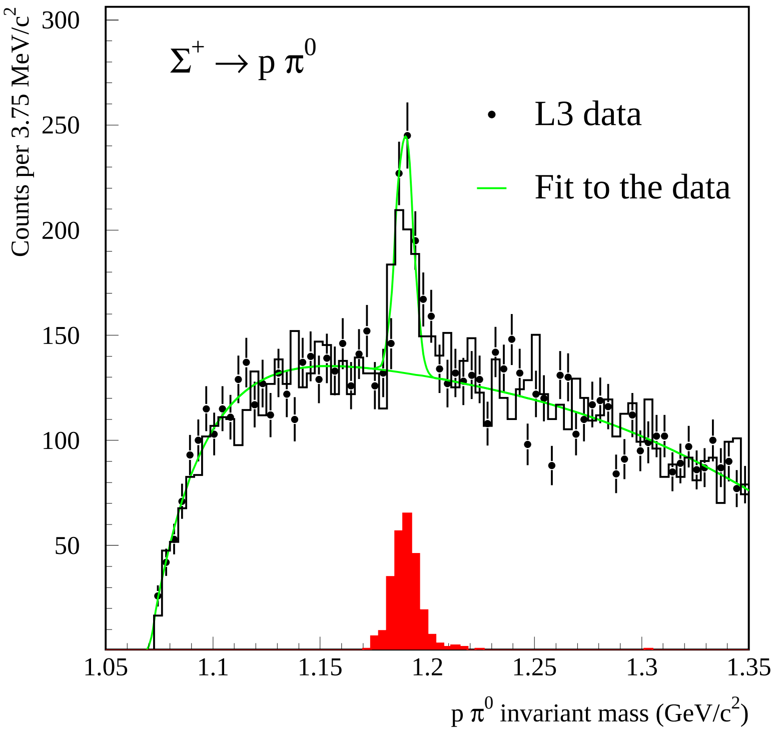

Fig. 6.4: **The Mass Distribution of $\mathbf{\Sigma^+}$ Candidates.**
The measured mass distribution has been fit with a threshold function $(P_1x_b{+}P_2x_b^2{+}P_3x_b^3)e^{(P_4x_b+P_5x_b^2+P_6x_b^3)}$, with $x_b = x - x_{threshold}$, in addition to a Gaussian function describing the $\mathbf{\Sigma^+}$ signal. The open histogram is from a Monte Carlo simulation, and the solid histogram is the amount of $\mathbf{\Sigma^+}$ signal according to the Monte Carlo generator information.

The final kinematics of the $\Sigma^+ \to \mathrm{p}\pi^0$ decay is restricted to reduce the amount of combinatorial background in the signal region of the mass distribution. In addition to a minimum constraint probability $\mathcal{P}_{\mathrm{svtx}}$, plotted in

Figure 6.3, the effectiveness of the kinematic constraint is strengthened by two factors, a minimum π^0 boost and a low probability $\mathcal{P}_{\text{psvtx}}$ that the Σ^+ decay vertex is equal to the primary vertex. The decay-frame angles, the total momentum and the transverse decay radius of the Σ^+ are also restricted.

$\boldsymbol{\Sigma^+}$ Selection:

$\mathcal{P}_{\text{svtx}} > 20\%$

$\mathcal{P}_{\text{psvtx}} < 10^{-12}$

$\gamma_{\pi^0} > 2.0, \ \ \cos\theta^* < 0.45$ and $|\vec{\mathbf{p}}_{\Sigma^+}| > 1.0$ GeV

$\mathrm{r}_{\text{min}} > 5$ mm (r_{max} is limited by the SMD inner radius)

The determination of the acceptance and efficiency for measuring the Σ^+ for this selection was computed based on a set of realistic Monte Carlo simulation. The mass distribution is shown in Figure 6.4.

6.4 *Measurement of the $\boldsymbol{\Sigma^0}$ Baryon*

The Σ^0 decays electromagnetically to $\Lambda^0\gamma$ nearly 100% of the time. The Σ^0 can, therefore, be assumed to decay at the primary vertex. Identification of the Λ^0 is done in the $\mathrm{p}\pi^-$ decay mode.

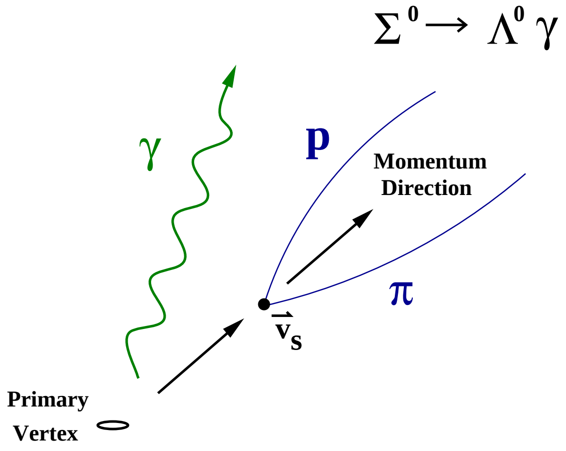

Fig. 6.5: **Decay Kinematics.** The $\boldsymbol{\Sigma^0}$ decays at the primary vertex, and the $\boldsymbol{\Lambda^0}$ decays at the point $\vec{\mathbf{v}}_{\mathbf{s}}$.

The kinematic constraints of the $\Sigma^0 \to \Lambda^0(\to \mathrm{p}\pi^-)\gamma$ decay are summarized by the following equations.

$$\vec{\mathbf{d}}(\vec{\mathbf{v}}_{\mathrm{s}}) \times [\vec{\mathbf{p}}_{\mathrm{p}}(\vec{\mathbf{v}}_{\mathrm{s}}) + \vec{\mathbf{p}}_{\pi}(\vec{\mathbf{v}}_{\mathrm{s}})] = 0$$

$$m_{p\pi}(\vec{\mathbf{v}}_s) = m_{\Lambda^0}$$

The hadronic event selection and the requirements on the primary vertex are the same as that for the Σ^+ baryon measurement, as described in Section 6.3. To select Λ^0 decays into $p\pi^-$, requirements are made on the tracking measurements.

Proton and π Track Selection:

$\mathrm{SPAN_{TEC}} \geq 10$ wires

$|\vec{\mathbf{p}}_{\mathrm{transverse}}| > 0.2$ GeV

either the proton or π must have

- SMD measured $\tan\lambda$ and z_0

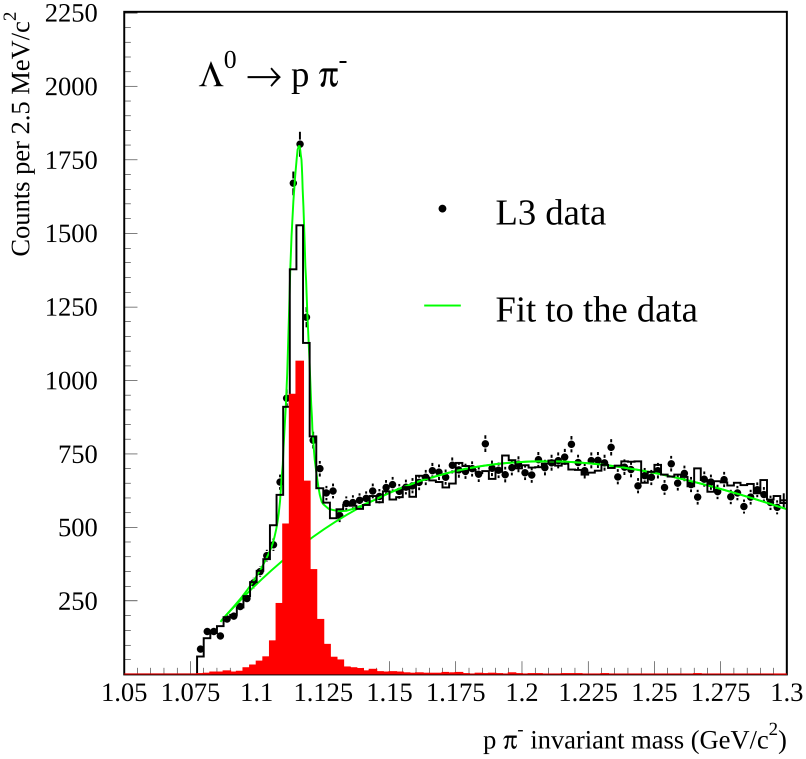

Fig. 6.6: **The Mass Distribution of $\boldsymbol{\Lambda^0}$ Candidates.**

The kinematics of the Λ^0 decay are summarized into three quantities: $\mathcal{P}_{\rm pvtx}$, $\mathcal{P}_{\rm zvtx}$ and $\mathcal{P}_{\rm lvtx}$. The first variable is the probability that the Λ^0 decays at the primary vertex. The logarithm of the probability is plotted in Figure 6.7. The second variable is the probability that the momentum-flight kinematics are satisfied[5]. The last variable is the combined probability of the momentum-flight kinematics and the Λ^0 mass constraint.

Λ^0 Selection:

$\mathcal{P}_{\rm pvtx} < 10^{-12}$

$\mathcal{P}_{\rm zvtx} > 1\%$

$\mathcal{P}_{\rm lvtx} > 1\%$

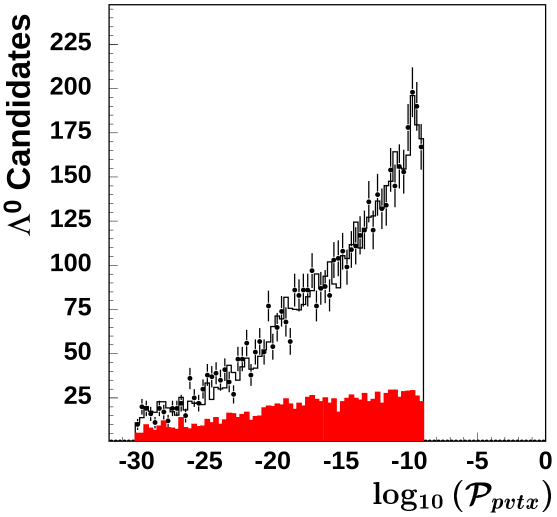

Fig. 6.7: **Λ^0 Primary Vertex Probability.** The 2-track primary vertex probability (after a pre-selection cut of 10^{-10}) is a falling distribution towards small probabilities. The Λ^0 distribution, shown with the solid histogram, because of its long decay-length does not fall off as rapidly.

The distribution of selected Λ^0 candidates, without the $\mathcal{P}_{\rm lvtx} > 1\%$ probability cut, is plotted in Figure 6.6.

The final kinematic requirements for the Σ^0 decay specify the range of the photon energy and the range of decay-frame angles for the Σ^0.

Σ^0 Selection:

$55\ \text{MeV} < E_{9\rm CORR} < 1000\ \text{MeV}$

$\cos\theta^* < 0.2$

The difference between the $\Lambda^0\gamma$ mass and the Λ^0 mass is plotted in Figure 6.8.

---

[5] The two-track 3D vertex is also part of the constraint.

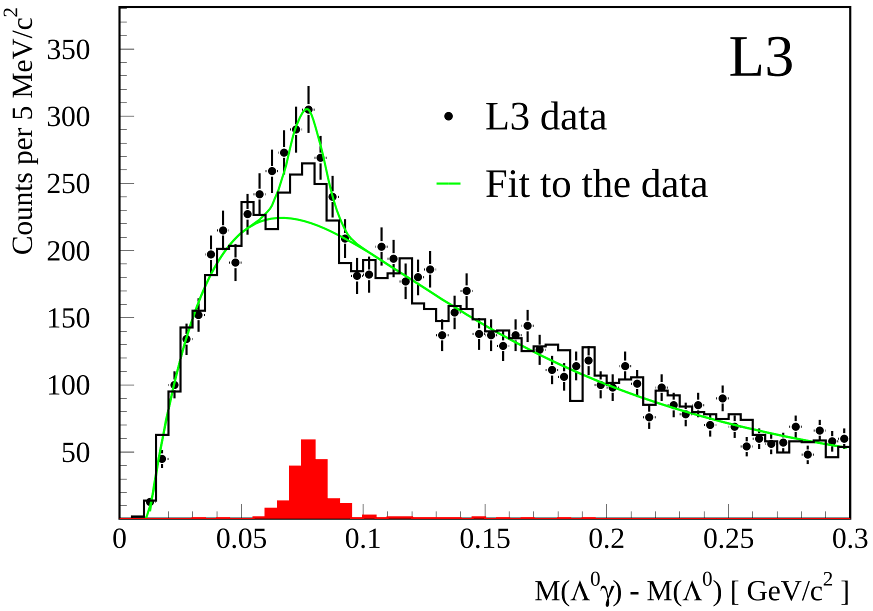

Fig. 6.8: **The Mass Difference Distribution of Σ^0 Candidates.**

The Σ^0 photon selection used for Figure 6.8 is the same as for the Σ^+ analysis. It is possible, however, to increase the purity of the photon selection by making use of the high photon detection efficiency of the BGO calorimeter. There are on average 18 photons per event coming from prompt π^0 production. Removing photons found in the π^0 peak reduces the combinatorial photon background for other decays. The increase in photon purity for selecting $\eta \to \gamma\gamma$ decays is shown in Figure 6.9. This method also improves the signal purity of the Σ^0 photon[6] selection, as shown in Figure 6.10.

6.5 Production Rates

The identification of Σ^+ and Σ^0 baryons in Z^0 decay data is based on the characteristic Gaussian-distributed signal shape present in the $p\pi^0$ and $\Lambda^0\gamma$ mass distributions, respectively. The extraction of production rate measurements requires some way to count the number of baryons found in these distributions and then to relate this count to the total number of baryons which were produced (including those which escaped detection).

---

[6] The energy and measurement width of the Σ^0 photon peak is reported in Section 6.6.

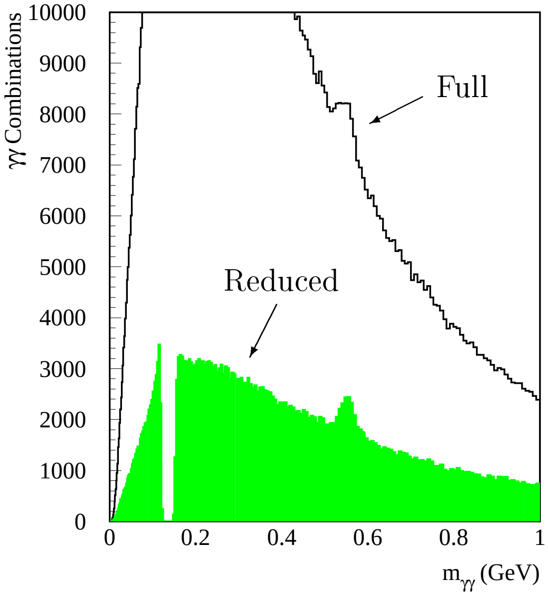

Fig. 6.9: **π^0 Photon Rejection.** The η peak from Figure 5.13 is more clearly seen when the photons from the π^0 peak are eliminated from the combinatorics.

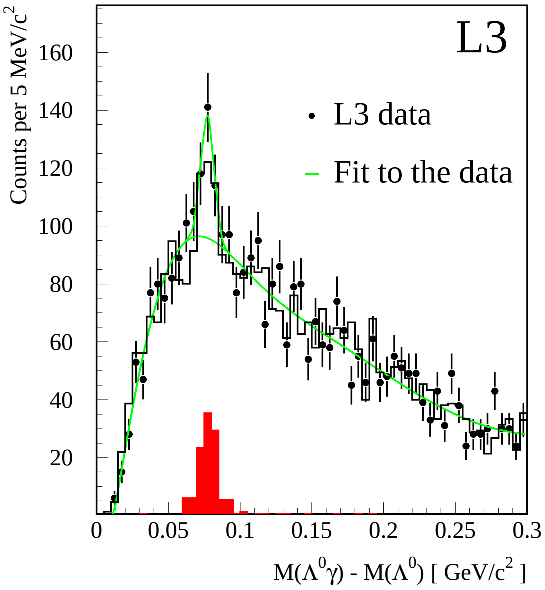

Fig. 6.10: **π^0 Photon Rejection.** The amount of background underneath the Σ^0 photon peak is reduced when photons selected from the π^0 peak are removed.

The calculation of the detection efficiency and acceptance is based on a set of realistic JETSET 7.4 Monte Carlo(MC) simulation for the L3 detector. The simulated events are hadronic decays of the Z^0, and the total MC statistics is

MC Statistics = 2011830 Events.

For quick reference, the exact numbers and calculations are stated in centered text in the following sections.

Σ^+ Rate Calculation

Of the Monte Carlo events, the percentage which have a Σ^+ (or a $\overline{\Sigma}^+$) produced in the Z^0 decay is 7.2%, computed from

Number of MC Σ^+ Produced = 144880 .

To determine the number of Σ^+ decays which are present in the Gaussian signal peak, the signal distribution (without background included) can be fit directly in the Monte Carlo. This avoids the additional statistical error of the background distribution. With a fixed value for the mass of the Σ^+ used in the fit,

$m_{\Sigma^+} = 1.18937$ GeV (Particle Data Group [15]),

the number of MC Σ^+ in the final $p\pi^0$ mass distribution is roughly 0.2%. The fit result is

Number of Σ^+ in MC Signal Distribution = 292.3 ± 17.1 .

However, because of differences between the MC and data, the normalization of the $p\pi^0$ candidate distribution, when comparing MC and data, does not agree with the statistical normalization. The number of selected hadronic Z^0 decays from 1994 and 1995 data-taking is

Number of Selected Hadronic Events in Data[7]= 1571162 Events.

The statistical normalization is, therefore,

$$\text{Statistical Normalization} = \frac{1571162}{2011830} = 0.781 \ .$$

The normalization of the $p\pi^0$ candidate distribution can be determined by calculating the total area in the sidebands next to the Σ^+ peak and using that to normalize. This procedure yields

Σ^+ Sideband Normalization = 0.835 ± 0.014 .

Therefore, there is a correction factor to the MC number of measured events

---

[7] This corresponds to the periods of data-taking called 94b, 94c, 94d, 95a and 95b.

which changes the Σ^+ efficiency,

$$\eta_{\Sigma^+} = \frac{\Sigma^+ \text{ Sideband Normalization}}{\text{Statistical Normalization}} = \frac{0.835 \pm 0.014}{0.781} = 1.069 \pm 0.018 \ .$$

⇒ The detection efficiency for all produced Σ^+ baryons is 0.22%, as seen,

$$\epsilon_{\Sigma^+} = \frac{292.3 \pm 17.1}{144880} \cdot \eta_{\Sigma^+} = \boxed{0.00216 \pm 0.00013} \ .$$

The number of measured Σ^+ in data with the fixed value of m_{Σ^+} listed above is determined by a combined fit with a threshold function, given in Table 6.4, and a Gaussian distribution. The number determined from the fit is

$$n_{\Sigma^+} = \boxed{310.3 \pm 35.7} \ .$$

Correcting this measurement with the above determined efficiency correction gives the Σ^+ production rate under the assumption of the shape of JETSET production distributions[8]. The average number of Σ^+ and $\overline{\Sigma}^+$ produced per hadronic Z^0 decay is found to be

$$\begin{aligned} \left\langle N_{\Sigma^+ + \overline{\Sigma}^+} \right\rangle^{\text{JETSET}}_{\text{fixed } m_{\Sigma^+}} &= \frac{310.3 \pm 35.7}{(0.00216 \pm 0.00013)(1571162)} \\ &= \boxed{0.0916 \pm 0.0105_{stat} \pm 0.0054_{eff}} \ . \end{aligned}$$

The contribution from the statistical(*stat*) error is significantly larger than the uncertainty in the efficiency(*eff*) calculation under the JETSET model assumption. The kinematic extrapolation based on other models and the systematic errors in the production rate measurement will be discussed later in this section.

Σ^0 Rate Calculation

The percentage of Σ^0 (and $\overline{\Sigma}^0$) produced per event in the set of 2 million Monte Carlo simulated hadronic decays of the Z^0 is 6.9%, computed from

$$\text{Number of MC } \Sigma^0 \text{ Produced} = 138300 \ .$$

To determine the number of signal events, both the mass and mass resolution

---

[8] The contribution to the rate measurement error from hadronic event selection is safely less than 5% and can be neglected.

of the Σ^0 are fixed to the values

$$m_{\Sigma^0} - m_{\Lambda^0} = 0.07687 \text{ GeV (Particle Data Group [15]) and}$$

$$\sigma_{(m_{\Sigma^0} - m_{\Lambda^0})} = 0.00695 \text{ GeV (Determined from MC).}$$

The signal shape for the Σ^0 photon is described by a Gaussian distribution. The photon resolution is determined primarily by the BGO calorimeter and the opening angle measurement between the photon and Λ^0, not the non-Gaussian mass distribution of the Λ^0. The number of MC Σ^0 in the final $\Lambda^0\gamma$ distribution is roughly 0.2%. The fit result is

$$\text{Number of } \Sigma^0 \text{ in MC Signal Distribution} = 256.9 \pm 16.0 \quad .$$

The difference between the sideband histogram normalization for the $\Lambda^0\gamma$ distribution and the statistical normalization appears to be small. However, the Λ^0 candidate distribution has a large deviation in sideband to statistical normalization[9] (discussed below). Therefore, the relatively small discrepancy in normalization in the final $\Lambda^0\gamma$ distribution is due to an internal cancellation. The statistical normalization is

$$\text{Statistical Normalization} = 0.781 \quad .$$

The correction factor is, therefore,

$$\eta_{\Sigma^0} = \frac{\Sigma^0 \text{ Sideband Normalization}}{\text{Statistical Normalization}} = \frac{0.699 \pm 0.012}{0.781} = 0.895 \pm 0.016 \ .$$

$\Rightarrow$ The detection efficiency for all produced Σ^0 baryons is 0.17%, as seen,

$$\epsilon_{\Sigma^0} = \frac{256.9 \pm 16.0}{138300} \cdot \eta_{\Sigma^0} = \boxed{0.00166 \pm 0.00010} \ .$$

The number of measured Σ^0 in data with the fixed value of m_{Σ^0} and σ_{Σ^0} listed above is determined by a combined fit with a threshold function, given in Table 6.4, and a Gaussian distribution. The number of Σ^0 baryons is

$$n_{\Sigma^0} = \boxed{293.3 \pm 40.8} \ .$$

The Σ^0 production rate is computed to be

$$\begin{aligned} \left\langle N_{\Sigma^0 + \overline{\Sigma}^0} \right\rangle^{\text{JETSET}}_{\text{fixed } m_{\Sigma^0} \text{ and } \sigma_{\Sigma^0}} &= \frac{293.3 \pm 40.8}{(0.00166 \pm 0.00010)(1571162)} \\ &= \boxed{0.1123 \pm 0.0156_{stat} \pm 0.0070_{eff}} \ . \end{aligned}$$

---

[9] From Figure 6.6, it appears that there is an excess of Λ^0 baryons measured in data. However, after mass selection, the number of Λ^0 candidates in data and MC with sideband normalization agrees to within 1%. The Λ^0 signal distribution is a double-Gaussian, and the fraction of signal in the wider Gaussian is larger in MC. However, this larger resolution is taken into account in the measurement errors and hence the mass probability selection.

In addition to the Σ^0 rate measurement, the ratio of Σ^0 to Λ^0 production can be determined from the data. The measurement of the ratio of rates involves a smaller efficiency correction and is therefore more accurate. In fact, the efficiency for selecting the Σ^0 photon once the associated Λ^0 has already been found is roughly 20%. This is to be compared with an overall 0.2% efficiency for Σ^0 selection.

The sideband normalization for the Λ^0 candidate distribution significantly differs from the statistical normalization. The source of this discrepancy was found to be the 2-track 3D vertex probability, which is flat in data, but is sloped in MC[10]. The correction factor is the ratio of the Σ^0 and Λ^0 sideband normalizations, as seen,

$$\eta_{\Sigma^0/\Lambda^0} = \frac{\Sigma^0 \text{ Sideband Normalization}}{\Lambda^0 \text{ Sideband Normalization}} = \frac{0.699 \pm 0.012}{0.573 \pm 0.004} = 1.219 \pm 0.023 \ .$$

The rate measurements were not found to be affected, within statistics, by the discrepancy in the vertex probability after the $\eta_{\Sigma^0/\Lambda^0}$ correction technique is applied.

$\Rightarrow$ The detection efficiency for selecting the Σ^0 photon is 23%,

$$\epsilon_{\Sigma^0/\Lambda^0} = \frac{256.9 \pm 16.0}{1391} \cdot \eta_{\Sigma^0/\Lambda^0} = \boxed{0.225 \pm 0.014} \ ,$$

where the efficiency is computed based on the number of Σ^0 found in the MC signal distribution, reported above, and the fraction of Λ^0 baryons coming from Σ^0 decay, namely,

Number of Λ^0 from Σ^0 in Selected Λ^0 Distribution = 1391 .

The Monte Carlo is used to determine the purity of the Λ^0 selection. The Λ^0 purity after mass selection was found to be

Purity of Λ^0 Selection = 0.522 (Determined from MC).

The ratio of the Σ^0 and Λ^0 production rates is measured by taking the number of Σ^0 measured in data correcting with the Σ^0 photon efficiency and then normalizing to the number of Λ^0 baryons[11] found in the data,

Number of Selected Λ^0 Baryons in Data = 6510.

---

[10] The theta-recovery technique using BGO bump information does not agree between MC and data in v213 of REL3. This can affect the theta determination for tracks without SMD measurements.

[11] The kinematic constraint requiring the Λ^0 to come from the primary vertex reduces the number of measured Λ^0 baryons coming from Ξ^-, Ξ^0 and Ω^- decay. Hence, the Λ^0 baryons used in the measurement are referred to as “prompt.”

This calculation results in the following measurement of the ratio of Σ^0 to prompt Λ^0 production in hadronic Z^0 decays,

$$\frac{\left\langle N_{\Sigma^0+\overline{\Sigma}^0}\right\rangle^{\mathrm{JETSET}}_{\text{fixed } m_{\Sigma^0} \text{ and } \sigma_{\Sigma^0}}}{\left\langle N^{\mathrm{prompt}}_{\Lambda^0+\overline{\Lambda}^0}\right\rangle^{\mathrm{JETSET}}} = \frac{293.3 \pm 40.8}{(0.225 \pm 0.014)(6510)(0.522)}$$

$$= \boxed{0.383 \pm 0.053_{stat} \pm 0.024_{eff}}\ .$$

Kinematic Extrapolation

If the entire kinematic range of the baryon production spectra were measurable by the detector, then there would be no need to rely in detail on the baryon kinematics predicted by the JETSET Monte Carlo simulation. However, since certain kinematic regions were excluded in the analysis, the prediction of the number of baryons in these regions is crucial.

The method used for determining the uncertainty in the measured fraction of baryons is to identify the principal kinematic restrictions on the baryon selection, and then to compute for several Monte Carlo models, the spread in the fraction of baryons predicted inside of these regions.

Kinematic Restrictions on the Σ^+:

$\gamma_{\pi^0} > 2.0$, $\cos\theta^* < 0.45$ and $|\vec{\mathbf{p}}_{\Sigma^+}| > 1.0$ GeV

$\mathrm{r_{min}} > 5$ mm (r$_{\mathrm{max}}$ is limited by the SMD inner radius)

The consequence of the $\mathrm{r_{min}}$ and $\mathrm{r_{max}}$ restrictions is to bias the Σ^+ acceptance towards a particular range of total momenta.

Kinematic Restrictions on the Σ^0:

55 MeV $< \mathrm{E_{9CORR}} <$ 1000 MeV

$\cos\theta^* < 0.2$

Λ^0 Kinematic Restrictions:

$|\vec{\mathbf{p}}_{\mathrm{transverse}}| > 0.2$ GeV (for the proton and pion)

$\mathrm{r_{min}}$ is limited by the $\mathcal{P}_{\mathrm{pvtx}}$ requirement

$\mathrm{r_{max}}$ is limited by the SMD inner radius

The fraction of baryons predicted to be inside the measured kinematic regions was computed for several Monte Carlo models, as summarized in Table 6.1. The maximum spread in these values is an estimate of the extrapolation error.

Monte Carlo	$\left\langle N_{\Sigma^+ + \overline{\Sigma}^+} \right\rangle$	$f^{obs}_{\Sigma^+}$	$\left\langle N_{\Sigma^0 + \overline{\Sigma}^0} \right\rangle$	$f^{obs}_{\Sigma^0}$	$\left\langle N_{\Lambda^0 + \overline{\Lambda}^0} \right\rangle$	$f^{obs}_{\Lambda^0}$
ARIADNE 4.08	0.0712	0.337	0.0680	0.123	0.3511	0.195
JETSET 7.4	0.0713	0.359	0.0679	0.126	0.3520	0.199
HERWIG 5.9	0.0975	0.339	0.0704	0.107	0.3710	0.182
COJETS 6.23	–	–	–	–	0.3899	0.213
Maximum Spread		6.1 %		15.1 %		14.6 %

Tab. 6.1: Estimation of Kinematic Extrapolation Error

The maximum spread in the predicted ratio of Σ^0 to Λ^0 production is 7.1%.

Systematic Errors

The systematic error of the production rate measurements is a combination of several sources of uncertainty. The efficiency calculation error from MC statistics was estimated in the Σ^+ and Σ^0 rate calculation sections. The kinematic extrapolation error was estimated in the previous section. What remains is the accuracy of the MC efficiency calculation in terms of modeling the detector performance and also the particle multiplicity and kinematics of hadronic decays of the Z^0.

For the most part, the level of disagreement in the shape of MC and data distributions is within the range of the statistical errors. An exception is in the 2-track 3D vertex probability calculation for Λ^0 baryons. The need for sideband normalization is due to a discrepancy in the tracking efficiencies for the category of tracks used in this analysis. There is also some effect from the differing size and position of the primary vertex in MC and data.

These discrepancies have been studied, and they affect mainly the overall normalization in the candidate distributions, as observed. In the case of the Σ^+, the removal of the fixed m_{Σ^+} constraint on the fit makes a change in the rate measurement, namely,

$$\begin{aligned}\left\langle N_{\Sigma^+ + \overline{\Sigma}^+} \right\rangle^{\text{JETSET}}_{m_{\Sigma^+}\text{ not fixed}} &= \frac{336.9 \pm 37.2}{(0.00216 \pm 0.00013)(1571162)} \\ &= 0.0994 \pm 0.0110_{stat} \pm 0.0058_{\mathit{eff}}\,.\end{aligned}$$

The change is less than 8% but indicates a systematic fit uncertainty. The total systematic error on the Σ^+ rate measurement is the sum in quadrature of three contributions,

$$\boxed{\sigma^{syst}_{\langle N_{\Sigma^+ + \overline{\Sigma}^+}\rangle} = 0.0054_{\mathit{eff}} \oplus 0.0056_{MC} \oplus 0.0072_{\mathit{fit}} = 0.0106_{syst}}\ .$$

In the case of the Σ^0, a second purity of selection was possible by means of the π^0 photon rejection technique. The production rate was measured with a higher signal to background ratio and found to be

$$\begin{aligned}\left\langle N_{\Sigma^0+\overline{\Sigma}^0}\right\rangle^{\mathrm{JETSET}}_{\pi^0\ \text{photon rejection}} &= \frac{114.4 \pm 24.3}{(0.00092 \pm 0.00008)(1571162)} \\ &= 0.0789 \pm 0.0168_{stat} \pm 0.0068_{\mathit{eff}}\ .\end{aligned}$$

The difference in this rate with the measurement made with a lower purity Σ^0 selection corresponds to a possible 15% systematic background/resolution uncertainty. The total systematic error on the Σ^0 measurement is

$$\boxed{\sigma^{syst}_{\langle N_{\Sigma^0 + \overline{\Sigma}^0}\rangle} = 0.0070_{\mathit{eff}} \oplus 0.0170_{MC} \oplus 0.0168_{back/res} = 0.0249_{syst}}\ .$$

For the measurement of the ratio of Σ^0 to prompt Λ^0 production, the two measurements of the Σ^0 production rate are used to estimate the systematic error in the background contribution[12]. This ratio with a higher Σ^0 purity is

$$\begin{aligned}\frac{\left\langle N_{\Sigma^0+\overline{\Sigma}^0}\right\rangle^{\mathrm{JETSET}}_{\pi^0\ \text{photon rejection}}}{\left\langle N^{\text{prompt}}_{\Lambda^0+\overline{\Lambda}^0}\right\rangle^{\mathrm{JETSET}}} &= \frac{114.4 \pm 24.3}{(0.125 \pm 0.011)(6510)(0.522)} \\ &= 0.270 \pm 0.057_{stat} \pm 0.023_{\mathit{eff}}\ .\end{aligned}$$

The total systematic error, denoted $\sigma^{syst}_{\Sigma^0/\Lambda^0}$, on the ratio of Σ^0 to prompt Λ^0 production is

$$\boxed{\sigma^{syst}_{\Sigma^0/\Lambda^0} = 0.0238_{\mathit{eff}} \oplus 0.0272_{MC} \oplus 0.0575_{back/res} = 0.0679_{syst}}\ .$$

---

[12] Included in this estimation is the systematic uncertainty in the Λ^0 selection and purity.

6.6 Comparison with Other LEP Measurements

The Σ^+ and Σ^0 production rate measurements can be compared directly to those made by the other LEP experiments. There is one other measurement of the Σ^+, and that was performed by the OPAL Experiment.

Σ^+ *Production from this analysis:*

$$\begin{aligned} \text{Data Statistics} &= 1.6 \text{ Million Hadronic } \mathrm{Z}^0 \text{ Decays} \\ m_{\Sigma^+} &= 1.1906 \pm 0.0007 \text{ GeV} \\ \sigma_{m_{\Sigma^+}} &= 0.0045 \pm 0.0007 \text{ GeV} \\ \left\langle N_{\Sigma^+ + \overline{\Sigma}^+} \right\rangle &= 0.092 \pm 0.011_{stat} \pm 0.011_{syst} \end{aligned}$$

To be compared with the OPAL measurement [28]:

$$\begin{aligned} \text{Data Statistics} &= 2.8 \text{ Million Hadronic } \mathrm{Z}^0 \text{ Decays} \\ m_{\Sigma^+} &= 1.1874 \pm 0.0012 \text{ GeV} \\ \sigma_{m_{\Sigma^+}} &= 0.0150 \pm 0.0014 \text{ GeV} \\ \left\langle N_{\Sigma^+ + \overline{\Sigma}^+} \right\rangle &= 0.099 \pm 0.008_{stat} \pm 0.013_{syst} \end{aligned}$$

The technique of detecting the Σ^+ in the OPAL detector differs greatly from that of the L3 Experiment. This difference is clearly seen in the shape of their Σ^+ mass spectrum, as shown in Figure 6.11.

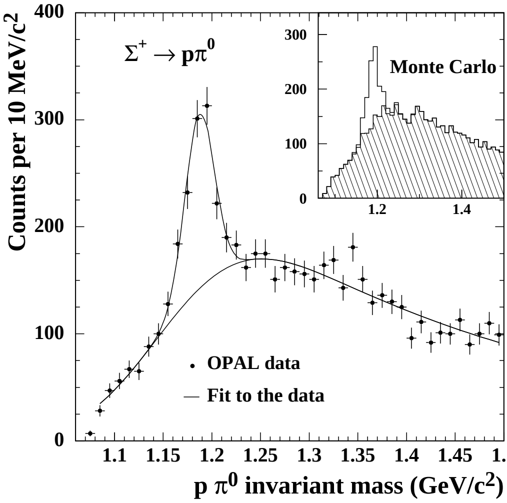

Fig. 6.11: **OPAL Σ^+ Distribution.** The mass distribution of $p\pi^0$ candidates measured by the OPAL detector has a characteristically different shape from that measured with the L3 detector, as shown in Figure 6.4.

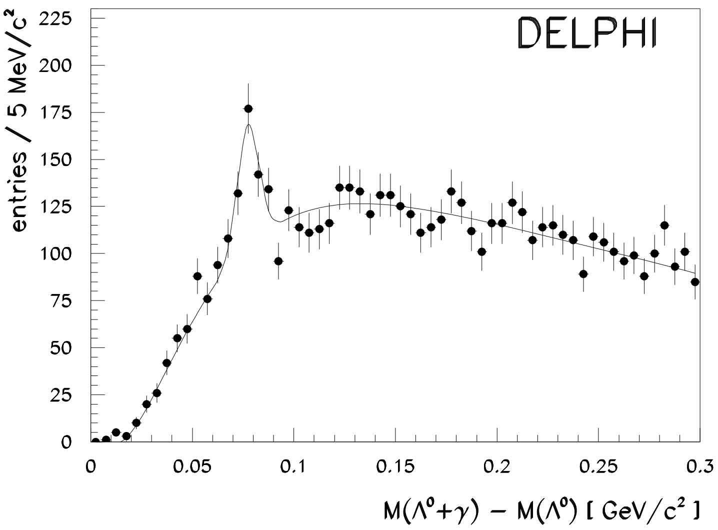

Fig. 6.12: **DELPHI Σ^0 Distribution.**
The Σ^0 photon is measured in the DELPHI detector by first having it convert through pair production. The momenta of the charged particles are then measured with their tracking detector.

Both OPAL and DELPHI have made Σ^0 rate measurements. These detectors rely on beam pipe and tracking material to convert the Σ^0 photon into an e^+e^- pair. The momenta of these particles are then measured with tracking detectors and combined to determine the photon energy.

Σ^0 *Production from this analysis:*

$$\text{Data Statistics} = 1.6 \text{ Million Hadronic } Z^0 \text{ Decays}$$
$$m_{\Sigma^0} - m_{\Lambda^0} = 0.0772 \pm 0.0012 \text{ GeV}$$
$$\sigma_{m_{\Sigma^0} - m_{\Lambda^0}} = 0.0046 \pm 0.0016 \text{ GeV}$$
$$\left\langle N_{\Sigma^0 + \overline{\Sigma}^0} \right\rangle = 0.112 \pm 0.016_{stat} \pm 0.025_{syst}$$

To be compared with the OPAL measurement [28]:

$$\text{Data Statistics} = 3.5 \text{ Million Hadronic } Z^0 \text{ Decays}$$
$$m_{\Sigma^0} - m_{\Lambda^0} = 0.075 \pm 0.001 \text{ GeV}$$
$$\sigma_{m_{\Sigma^0} - m_{\Lambda^0}} = 0.0044 \pm 0.0009 \text{ GeV}$$
$$\left\langle N_{\Sigma^0 + \overline{\Sigma}^0} \right\rangle = 0.071 \pm 0.012_{stat} \pm 0.013_{syst}$$

And the DELPHI measurement [29]:

$$\begin{aligned} \text{Data Statistics} &= 3.1 \text{ Million Hadronic } Z^0 \text{ Decays} \\ m_{\Sigma^0} - m_{\Lambda^0} &= 0.078 \pm 0.001 \text{ GeV} \\ \sigma_{m_{\Sigma^0} - m_{\Lambda^0}} &= 0.0053 \pm 0.0011 \text{ GeV} \\ \left\langle N_{\Sigma^0 + \overline{\Sigma}^0} \right\rangle &= 0.070 \pm 0.010_{stat} \pm 0.010_{syst} \end{aligned}$$

The Σ^+ production rate measurement agrees with that measured by OPAL. However, the Σ^0 measurement from this analysis is larger than the DELPHI and OPAL measurements by more than the statistical error. The BGO detector makes it possible to measure Σ^0 photons down to lower energies than can be measured by other detectors. Thus, the discrepancy in the rate measurements could be due to the kinematic extrapolation term in the systematic error.

6.7 $\mathbf{\Sigma^+}$ *Polarization*

Quarks coming from Z^0 decay are highly polarized. Anti-quarks are polarized by the same amount, but in the opposite direction. The percentage of polarization depends on the electroweak interaction as expressed in equation (3.6). These evaluate to

$$\mathcal{P}_q = -\mathcal{P}_{\bar{q}} = \left\{ \begin{array}{ll} -67\% & u, c \\ -94\% & d, s, b \end{array} \right. ,$$

for the different quark flavors listed.

Heavy baryons formed from primary quarks are predicted to retain this polarization, while lighter baryons are not [30]. However, light baryons produced in heavy baryon decay, such as the Σ^+, may inherit some of this polarization[13]. Therefore, a longitudinal polarization in Σ^+ baryons (and the opposite polarization for $\overline{\Sigma}^+$) would indicate both that heavy baryons are polarized and that a fraction of which decay into the Σ^+.

As described in Section 3.4, the Σ^+ baryon and the $\overline{\Sigma}^+$ anti-baryon decay via the parity-violating charged-current interaction. Therefore, if there were

---

[13] The α parameter for two-body decays of heavy baryons is predicted to be near unity [30]. This would cause light baryons produced in heavy baryon decay to have a longitudinal polarization.

a longitudinal polarization of the Σ^+, it would be present in the $p\pi^0$ decay-angular distribution. In fact, the value of α determining the coefficient of the $\cos\theta_p$ dependent part of the differential cross-section is maximal for the Σ^+, as shown in Table 3.4.

The difference in the Σ^+ and $\overline{\Sigma}^+$ rates for equal values of the decay-frame angle of the proton and anti-proton, respectively, is a way to look for polarization. This is expressed in the quantity

$$\mathrm{A}_{\Sigma^+} = \frac{n_{\Sigma^+} - n_{\overline{\Sigma}^+}}{n_{\Sigma^+} + n_{\overline{\Sigma}^+}} \cdot \frac{1}{\epsilon} \quad ,$$

where ϵ is the fraction of Σ^+ and $\overline{\Sigma}^+$ signal present in each bin of $\cos\theta^*$. The error on ϵ is a binomial error

$$\sigma_\epsilon = \epsilon \cdot \sqrt{\frac{(1-\epsilon)}{n_{\mathrm{signal}}}}, \qquad \epsilon = \frac{n_{\mathrm{signal}}}{n_{\mathrm{total}}} \quad .$$

The value of A_{Σ^+} is computed in bins of $\cos\theta^*$ and plotted in Figure 6.13.

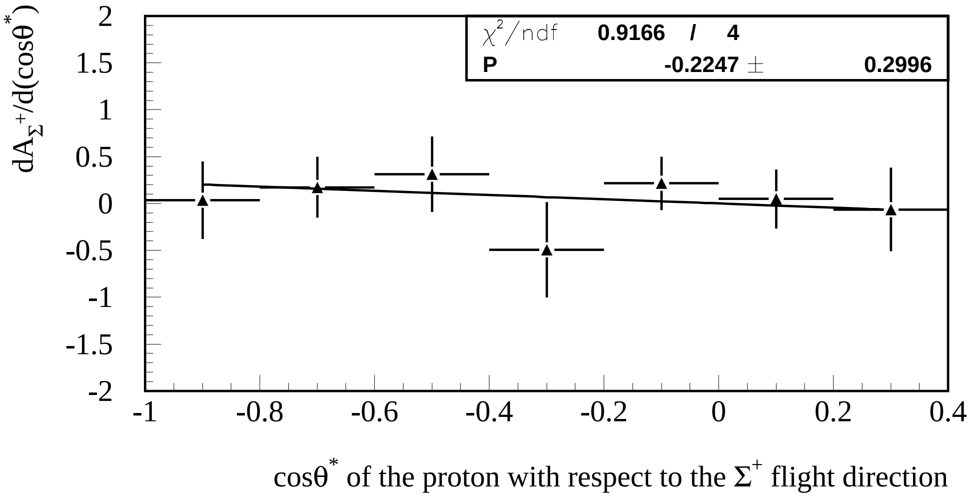

Fig. 6.13: **Longitudinal Polarization Measurement in Σ^+ Decays.**

No statistically significant polarization is observed in Σ^+ baryons produced in Z^0 decay. The value is taken from the fit of Figure 6.13 divided by $-\alpha$, as the proton and not the π flight direction is being measured. The result obtained is

$$\boxed{\mathcal{P}_{\Sigma^+} = (-23 \pm 31)\%} \ .$$

This measurement has not been performed by the other LEP experiments. It is a potentially interesting way to infer the polarization of charm baryons produced from Z^0 decay especially if the "Σ^+ from charm" sample could be enhanced in some way.

6.8 Summary and Outlook

The production rates of two baryons, the Σ^0 and Σ^+, have been measured in hadronic Z^0 decays using the L3 detector at LEP. These baryons come from the same isospin multiplet and therefore are predicted to be produced at nearly equal rate. The ratio of the Σ^0 and Σ^+ rates and the corresponding estimates for the statistical and systematic errors were measured to be

$$\frac{\left\langle N_{\Sigma^0+\overline{\Sigma}^0}\right\rangle}{\left\langle N_{\Sigma^++\overline{\Sigma}^+}\right\rangle} = 1.22 \pm 0.23_{stat} \pm 0.31_{syst} \quad \text{(Measured)} ,$$

while the predicted value of this ratio is

$$\frac{\left\langle N_{\Sigma^0+\overline{\Sigma}^0}\right\rangle}{\left\langle N_{\Sigma^++\overline{\Sigma}^+}\right\rangle} = 1.05 \quad \text{(Predicted [14])} .$$

The measurement and prediction are in agreement. A summary of several baryon and meson production measurements taken at three different e^+e^- accelerators is plotted in Figure 6.14. Included in this figure are the two measurements made by this analysis.

A large fraction of Σ^0 and Σ^+ baryons come from heavier baryon decays or contain a primary quark from $Z^0(\rightarrow q\bar{q})$ decay, 67% and 66%, respectively [14]. Deviations from the trend set by the production rate curve of Figure 6.14 could indicate unaccounted for heavy baryon decays. In particular, both the Σ^0 and Σ^+ production rates are greater than one standard deviation above the predicted rate. One possible explanation is that this excess comes from c-baryons whose decays are not yet well-catalogued [15].

The ratio of Σ^0 to prompt Λ^0 production was also measured in this analysis. The Σ^0 and Λ^0 baryons have the same quark content, and yet their rates are predicted to be different. This is due to the mass difference of the Σ^0 and Λ^0, measured to be $m_{\Sigma^0} - m_{\Lambda^0} = 0.0772 \pm 0.0012$ GeV, and to the

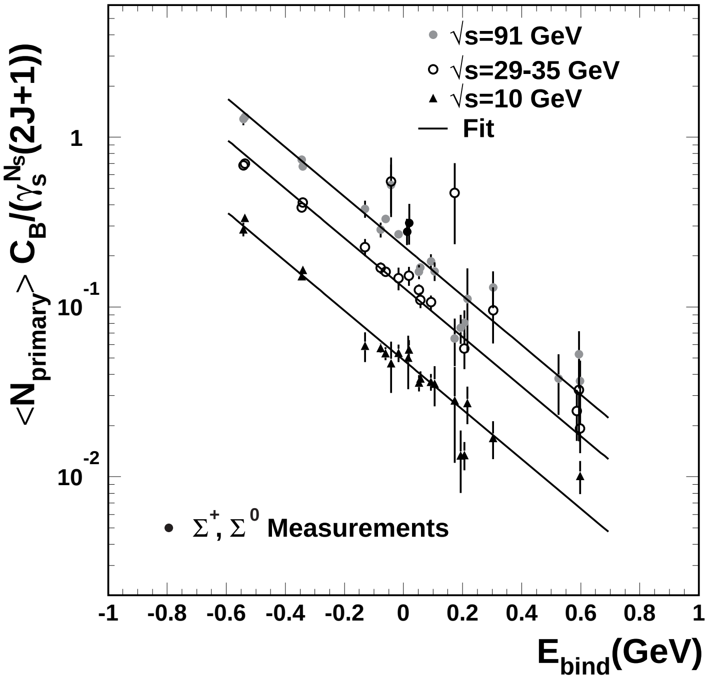

Fig. 6.14: **Production Rate Measurements [14].** As a function of the hadron binding energy, described in Section 3.3.1, baryon and meson production rates (excluding primary quark contributions and feed-down from other hadron decays) lie on a single curve for different center-of-mass energies. The $\mathbf{\Sigma^0}$ and $\mathbf{\Sigma^+}$ measurements from this analysis are included with the $\sqrt{s} = 91$ GeV data.

differing amount of feed-down contribution from other baryon decays. The measurement of Σ^0 to prompt Λ^0 production, found to be

$$\frac{\left\langle N_{\Sigma^0+\overline{\Sigma}^0}\right\rangle}{\left\langle N^{\text{prompt}}_{\Lambda^0+\overline{\Lambda}^0}\right\rangle} = 0.383 \pm 0.053_{stat} \pm 0.068_{syst} \quad \text{(Measured)}\ ,$$

can be used to infer the temperature T in equation (3.9).

For $T = 0.29$ GeV $= 3.4$ trillion degrees centigrade, the predicted value for this ratio is

$$\left.\frac{\left\langle N_{\Sigma^0+\overline{\Sigma}^0}\right\rangle}{\left\langle N^{\text{prompt}}_{\Lambda^0+\overline{\Lambda}^0}\right\rangle}\right|_{T=0.29\ \text{GeV}} = 0.277 \quad \text{(Predicted [14])}\ .$$

The prediction is lower than the value measured above. This indicates that the mass dependence of baryon production is not as strong, and implies a correspondingly higher value for T. As can be seen in Figure 6.14, the final determination of T requires a combined fit of all baryon and meson production rate data from many experiments and collision energies.

The hadronization temperature, if indeed that is what the parameter T describes, is potentially an important physical quantity. The impact of baryon production measurements in Z^0 decay might one day influence the description of the fundamental interaction responsible for quark confinement in addition to applications outside of collider experiments.

From P.J.E. Peebles, *Principles of Physical Cosmology* [31] (page 681),

> In the standard model the universe at redshifts $z \gtrsim 10^4$ has to expand in a nearly homogeneous way, with few of the complications that characterize recent epochs. There are departures from near thermal equilibrium, at the epoch of production of light elements, at the earlier phase transitions of the particle physics that produced ordinary baryonic matter out of quarks, separated the electric and weak interactions, and maybe adjusted the local value of the entropy per baryon, and perhaps still earlier at the phase transitions that produced cosmic strings or textures or nonbaryonic dark matter. We have relicts in the light elements; it would be exceedingly interesting to find others.

A. BGO RESOLUTION FUNCTIONS

This appendix presents the resolution functions for electromagnetic showers measured in both the barrel and endcap regions of the BGO calorimeter.

Energy Resolution Functions:

Barrel

$$\sigma_E^{\text{Gaussian}}(E)/E = \frac{1.57\%}{\sqrt{E}} + 0.34\% \tag{A.1}$$

$$\sigma_E^{\text{Full}}(E)/E = 3.42\% \exp[-\frac{E}{0.854}] + \frac{1.57\%}{\sqrt{E}} + 0.34\% \tag{A.2}$$

Endcap[1]

$$\sigma_E^{\text{Gaussian}}(E)/E = \frac{1.57\%}{\sqrt{E}} + 0.34\% \tag{A.3}$$

$$\sigma_E^{\text{Full}}(E)/E = 10.73\% \exp[-\frac{E}{1.784}] + \frac{1.57\%}{\sqrt{E}} + 0.34\% \tag{A.4}$$

Modification for Electronic Noise and Calibration Errors

$$\sigma_E^{\text{Full}}(E)^2 = \sigma_E^{\text{Full}}(E)^2 + N_9 \cdot \sigma^2_{\text{intrinsic}} + (N_9 \cdot \sigma_{\text{correlated}})^2 + (\sigma_{\text{calibration}} \cdot E)^2 \tag{A.5}$$

with $\sigma_{\text{intrinsic}} = 1$ MeV, $\sigma_{\text{correlated}} = 1.6$ MeV and $\sigma_{\text{calibration}} = 1.5\%$ in 1995 data-taking. The value of N_9 is the number of crystals above threshold in a 3×3 array centered on the electromagnetic shower.

ϕ-Resolution Functions:

Barrel

$$\sigma_\phi^B(E) = \frac{3.28 \text{ mrad}}{\sqrt{E + E_c(E)}} + 0.82 \text{ mrad} \tag{A.6}$$

---

[1] Below 300 MeV, the tailing effect in the endcap energy measurement becomes extreme. Photons in the tail are lost.

$$E_c(E) = \frac{E_0}{1+\exp\left[2\left(\frac{E-E_0}{E_0}\right)\right]}, \quad E_0 = 0.098\ \mathrm{GeV}$$

Endcap

$$\sigma_\phi^E(E,\theta) = \big(1.21\,\sigma_\phi^B(E) + 2.56\ \mathrm{mrad}\big)\left(\frac{4.76/|\tan\theta| + 3.81}{4.76/|\tan\theta_{ref}| + 3.81}\right) \qquad \text{(A.7)}$$

with $\tan\theta_{ref} = 523\ \mathrm{mm}/758\ \mathrm{mm}$ taken to be the intersection of the barrel and endcap volumes.

θ-Resolution Functions:[2]

Barrel

$$\sigma_\theta^B(E,\theta) = \sigma_\phi^B(E)\left(\frac{5.55\ \sin\theta + 1.21}{5.55\ \sin\theta_0 + 1.21}\right), \quad \theta_0 = \frac{\pi}{2} \qquad \text{(A.8)}$$

Endcap

$$\sigma_\theta^E(E,\theta) = \big(0.77\,\sigma_\phi^B(E) + 0.99\ \mathrm{mrad}\big)\left(\frac{6.06\,|\cos\theta| + 0.66}{6.06\,|\cos\theta_{ref}| + 0.66}\right) \qquad \text{(A.9)}$$

with $\tan\theta_{ref} = 523\ \mathrm{mm}/758\ \mathrm{mm}$ taken to be the intersection of the barrel and endcap volumes.

---

[2] The θ-resolution functions were determined assuming the smearing of the primary vertex position is removed, as would be the case if the 3D primary vertex were used. In addition, the correction to θ for a non-zero vertex position must be applied.

B. BGO NOISE DE-CORRELATION ALGORITHM

The presence of correlated noise in the BGO analog electronics has a pronounced effect on low energy measurements and shower shape parameters. A method was developed to recompute event-by-event for each correlated region a new pedestal baseline. This method is known as the BGO Noise De-Correlation Algorithm and can be found in the ECL3 Reconstruction code in the routine ECCORNO. This appendix reports on the principles and drawbacks of this technique as well as simulation results and noise calculations that measure its performance.

Introduction

Many analyzes in L3 are based on measurements made by the BGO calorimeter. Typically, distributions of the number of BGO bumps above some energy cut, the ratio of an energy estimate based on 9 crystals to an estimate based on 25 crystals or an even more elaborate neural network analysis using the measurement of every crystal are useful handles for identifying event topologies and single particle showers. Fundamental to all these techniques is the basic knowledge of the working set–that is, which crystals were readout, why they were readout, and how useful is the information they contain. Noise plays an important part in determining this set as does the general organization of the BGO readout electronics.

Correspondingly, noise de-correlation modifies the BGO working set. The noise de-correlation algorithm is nothing but a pattern recognition technique for deciding whether particular channels of a correlated group reside within the pedestal baseline, and then subtracting the mean value of those channels found in the baseline. As is easily seen in the noise calculations presented in this paper, what the noise de-correlation algorithm does (barring pattern recognition failures) is to guarantee that the correlated noise level in the worst case is equal to the intrinsic noise of a single channel. What is also clear is that the most reliable way to reduce the noise down to this level is to improve the grounding connections at the analog electronics, and this was achieved during the 1995 running period, giving the total average noise levels for the whole detector the value of 1.45 MeV.

BGO Readout System

The BGO analog electronics, or Princeton level-1 boards, are mounted in aluminum boxes located at the end of the barrel hadron calorimeter. There are 16 Lausanne boxes on each side. The general layout of the readout boards within each box is displayed in Figure B.1.

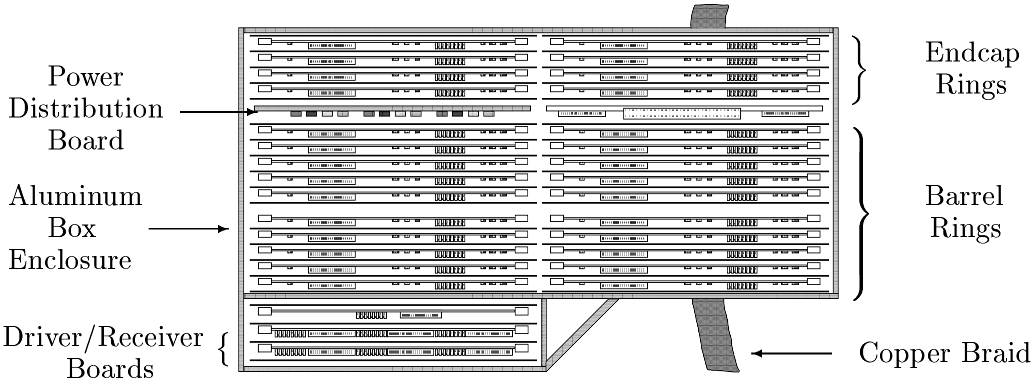

Fig. B.1: General Layout of BGO Readout Electronics within 1 of the 32 Lausanne Boxes.

As far as correlated noise is concerned, the most important board is the power distribution board. Three separate power supplies each providing three voltages are given a common ground connection on this board, the so-called box ground. The box ground for each of the 16 Lausanne boxes per side is connected directly to a thick copper braid mounted on the barrel hadron calorimeter. If the box ground is damaged, the box will “float” with an AC ground level different from that of the copper braid. This is the first source of correlated noise.

Each Princeton level-1 board has 12 complete BGO channels, meaning each channel has its own 6305 processor and can be given separate readout instructions. In the barrel, 5 of the 12 channel boards have their 40-pin connectors cabled together forming one linear chain of processors each of which is communicated to one after the other, the so-called BGO ring. Each ring is connected to one of the driver/receiver 40-pin connectors. The endcap rings have 4 of the 12 channel boards cabled together. If each microprocessor did not have its own 80 reading event buffer, then the length of the BGO ring would impose a speed limitation in the BGO readout and subsequent dead time for the whole detector.

Historically, in fact, the BGO in 8-bunch timing was never run in buffered mode. The reason for this is that buffer transfers–reading from each microprocessor and transferring digital data over the flat cables through the driver/receiver to the level-2 microprocessors in P1–would cause ground level shifts for the analog electronics while the BGO was live (integrating the signal of a new trigger). Much analysis, performed by Peter Denes of Princeton, was done to overcome the problem of "mixed mode" readout boards–that is, the presence of digital and analog electronics on the same PCB. The solution comes from the completely synchronous operation of the experiment. In addition, the driver/receiver boards now have an optical isolation between the direct microprocessor reading and the driving of the signal to level-2, which is done on a separate power supply not connected to the box ground.

Nevertheless, mixed-mode is mixed-mode, and digital activity will, in general cause ground level AC shifts within each ring. This gives the final grouping of the correlated noise pattern. For an overall summary, there are 4 barrel rings and 2 endcap rings in each Lausanne box. Each level-1 power supply powers 2 BGO rings. The 24 channel preamp boards are grouped from two 12 channel level-1 boards in separate rings powered by the same supply. The preamp shields are separately connected to the copper braid, but the lowest impedance ground for a given channel is still the ring ground.

Sparsed Mode

The BGO electromagnetic calorimeter consists of 192 rings, 128 barrel and 64 endcap, giving 10752 total channels. In addition, there are 16 Lumi Rings, 4 ALR Rings and 2 EGAP Rings. A threshold setting system called BASE in combination with the 6305 microprocessor code was developed to reduced the amount of readings transferred from level-1 to level-2 of the BGO.

In a BASE reading, each level-2 processor sends triggers to the ring it communicates with and histograms all the pedestal readings which are made.

The level-2 processor then does a running integration from the upper edge of the histogram until it find 6% of the number of triggers. This ADC value (which can be at maximum the full range of the highest gain part of the ADC–"comparator 1") is the sparsed threshold. If the microprocessor instruction byte is set to sparsed mode, then in normal data taking, if the ADC reading is equal to or above this value, then the ADC value is transferred up to level-2. (The lowest threshold value is 1; therefore, 0 ADC readings from negative pedestals are suppressed.) Some channels are chosen to be read unsparsed.

The unsparsed channels were used to monitor the functioning of the digital connection to the ring. Without unsparsed channels, no readings from a ring in a given event would be possible, even though this could also occur from a broken ring cable. Through mid-1994, only one unsparsed channel was given to each ring, but with the advent of noise de-correlation, there are currently 2 barrel unsparsed channels and 3 endcap unsparsed channels.

As an aside, the 6% sparsed thresholds may or may not correspond to a particular number of BASE RMS above the nominal pedestal, that depends on the exact pedestal spectrum. The thresholds are recorded in the BGO initialization vector which is attached to the end of events with hardware event number 0. By direct comparison, the difference between the threshold and nominal pedestal for one particular BASE run corresponds to a mean value of 1.632 times the RMS noise measurement, as shown in Figure B.2. Online monitors constantly monitor the readout percentage of the BGO during data taking. This value is consistently 11%.

BGO Noise Levels

Intrinsic Noise

The ADC alone, with no preamp connected, has 20 μV of noise, referenced to input. The Lyon preamp has a noise level of 40 - 45 μV, which in quadrature with the ADC noise gives a total intrinsic noise of 50 μV per channel (this corresponds to roughly 1 MeV of signal). Anomalously low noise levels indicate that something is broken or disconnected. In the case of Endcap Ring 9/8, or in ECCORNO convention Ring 119, the pin carrying one of the ADC timing signals was broken. This had resulted in noise levels of 11 μV, which is even below the noise level for a functioning ADC. Another source of low noise readings comes from negative pedestals.

Negative pedestals are a concern. These channels have no noise measure-

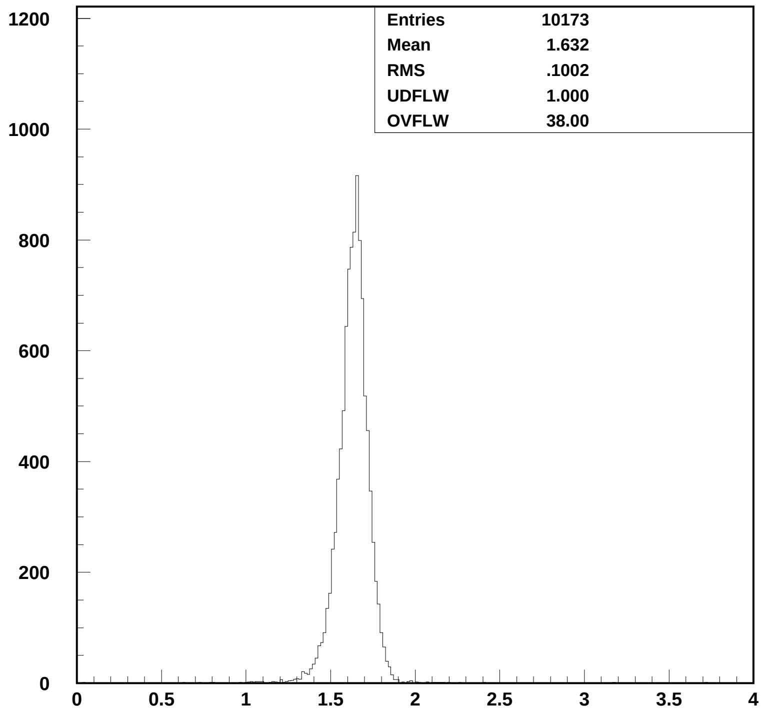

Fig. B.2: Distribution of Thresholds in Number of BASE RMS above Pedestal.

ments. The DC feedback of the low energy ADC channel to the preamp is set so that the integration of a voltage over the timing gate is a positive value. The digitizing DAC only goes from 0.0 V to 10.0 V, which is the same dynamic range as the Lyon preamp. However, in a synchronous environment, negative spikes which come exactly at the same frequency as the LEP crossing time (or in an integer multiple), will integrate to a net negative value–the equal and opposite positive part being injected during non-integration times. One unpleasant example of synchronous noise was the double-headed BGO pedestals in a ratio of 1:2. This came from the SMD switching power supplies which ran at 1/3 the LEP crossing time. This noise source was eventually removed by Italian ingenuity and additional ground cables from the box ground to the copper braid for boxes with preamp cables located in the vicinity of SMD power cables.

Correlated Noise

If the noise in the calorimeter were dominated by intrinsic noise, then the probability that in sparsed readout mode that n crystals in a ring are readout would be a monotonically decreasing function of n. By direct measurement, as shown in Figure B.3, there is a spike present at 100 % readout percentage. In fact, a detailed look at the time dependence of the pedestal readings of any two channels in a ring shows that their fluctuations are nearly identical for BASE measured RMS values above 2 MeV, as in Figure B.4.

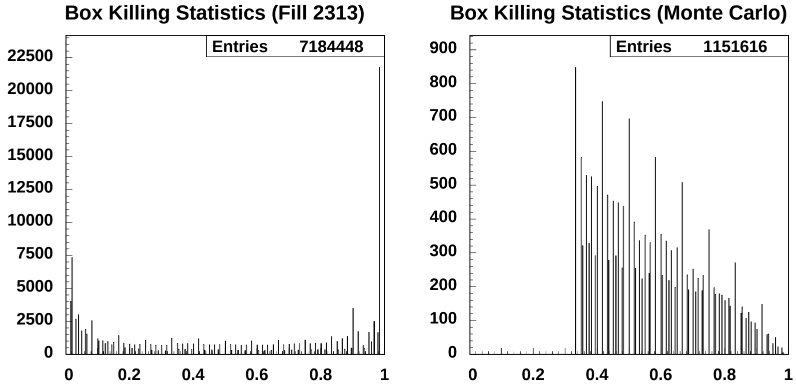

Fig. B.3: BGO Ring Readout Fraction for Data (Fill 2313) and Monte Carlo.

Suppose that after a fill of data were taken, one were to go back and correct the event-by-event pedestal values for each channel in every ring. There would still be the remaining problem of the readout thresholds. Even if the noise level were measured to be 2.5 MeV from correlated noise, instead of the 1.0 MeV of intrinsic noise, the effective threshold would not be 1.632×2.5 MeV = T_BASE for every event. If there were a negative baseline swing of 5 MeV in a ring, then the readout threshold for channels in that ring would be 5 MeV + T_BASE. Similarly, for upward swings, the effective thresholds are reduced. This kind of behavior is, in general, not modeled by shower shape parameters that do not take into account the event-by-event thresholds for each crystal.

Another important point about correlated noise is that since it is, in general, coming from an external source, its average effect on pedestals can change between the time the BASE was taken and when data taking actually begins. This is also a natural consequence of BEAM PICKUP/BGOMARK phase locking which only occurs once beam is in the machine. Therefore, the

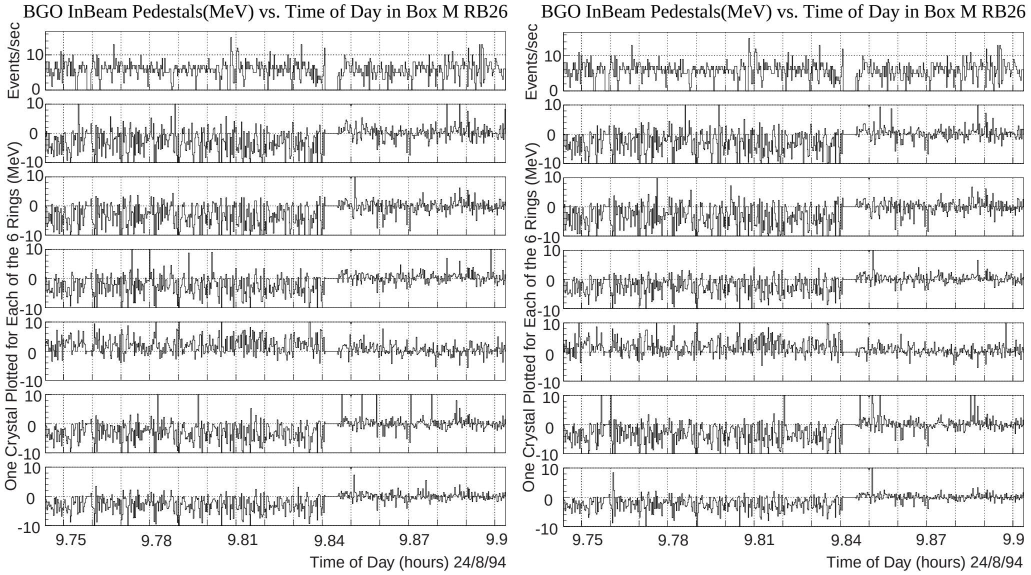

Fig. B.4: Example of Time-Dependent Pedestal Fluctuations for Two Sets of Channels Located in Each of the 6 Rings in a Box. Correlation of the Horizontally Arranged Plots is the Ring Ground, of the Vertical Plots is the Box Ground, and Pair-Wise in the Vertical is the Power/Preamp Ground. The top-most plots are the number of events per second.

mean value of the pedestal for all pedestals in a ring may have a constant shift. This is exhibited by rings that have an abnormally high or low readout frequency during a fill. Fortunately, a constant shift is corrected in the same way as an event-by-event shift.

Noise De-Correlation Pattern Recognition

The "de-correlation" of the pedestals in a ring is a misnomer. In fact, if one computes based on the readings within a ring a new pedestal baseline, then the error on the calculated mean becomes the new level of correlated noise. When using a single unsparsed channel to restore the baseline, the intrinsic noise fluctuations on that channel now become common to all the channels from which it was subtracted. Therefore, if the total noise levels for all channels fell below $\sqrt{2}$ MeV and only single channel subtraction were being performed, then the noise "de-correlation" routine would become the noise "correlation" routine. Calculations below show that even for 1995 data, the routine is estimated to still improve the average noise level in a 3x3 matrix of crystals.

Preparation. The algorithm begins by computing the average RMS noise levels per ring of the crystals which have been readout. The RMS reading of a single crystal is sufficient; however, care must be taken to remove the readings of crystals whose channels have been marked as non-functioning. **A minimum required RMS cut of 36 μV is the only means of removing broken channels.** In the database, non-functioning channels are given a negative RMS. Disconnected channels and negative pedestal channels are also removed by this cut.

Readout Percentage Breakup. Based on Figure B.3, the different approaches to de-correlation are split up. Above 2/3 readout fraction, enough crystals are present to attempt **Box Killing**, described below. If the unsparsed channel is reading a voltage less than its nominal pedestal plus 3 BASE RMS, then both the **Local Flatness Test** of Y.F.Wang and the **Ring Readout Fraction Test** are applied. Above this range, only the **Ring Readout Fraction Test** is applied.

1) **Local Flatness Test** of Y.F.Wang. One approach for eliminating the use of unsparsed channels which have had energy deposited within the crystal is to look at neighboring channels (even if the channels are located in a different ring in the same box). A computation is made of the RMS of the readings in the unsparsed channel and in neighboring channels, and if this RMS is less than 6 times the average ring RMS and the mean value is less than 3 times the average ring RMS above the nominal pedestal, then the unsparsed channel under test is marked as being in the pedestal baseline.

2) **Ring Readout Fraction Test.** Another approach is to make use of the very low levels of intrinsic noise present in each channel, approximately 1 MeV. First of all, if the unsparsed channel reading is over 3 BASE RMS above the nominal pedestal and the ring readout fraction is less than 1/3, then the channel is considered to have energy in it. If in a window of ±1 MeV around the reading of the unsparsed channel, over 1/3 of the fraction of channels readout are present, then the unsparsed channel under test is marked as being in the baseline. This window increases slightly with voltage, but goes to a maximum of ±3.5 MeV for 250 MeV baseline shifts and above.

3) Box Killing. In the case where over 2/3 of a ring has been readout, then the same **Ring Readout Fraction Test** is performed, but for every crystal that has been readout. A limit is then placed on the minimum number of crystals that must to be found in the baseline (at least 11) and the RMS spread of the channels found in the baseline as a function the computed baseline correction. Figure B.5 shows the number of crystals used in **Box Killing** in data, with a peak just below 48 crystals for the endcap and just below 60 crystals for the barrel. Figure B.6 shows the maximum allowed RMS spread curve overlayed on top of data and Monte Carlo for **Box Killing** candidates. Data points above this curve are considered to be energy depositions and not noise. What is important about this curve is that the slope is less than 1 to avoid large localized energy depositions from mimicking upward pedestal shifts. The slope of the curve for large pedestal shifts is 3/8.

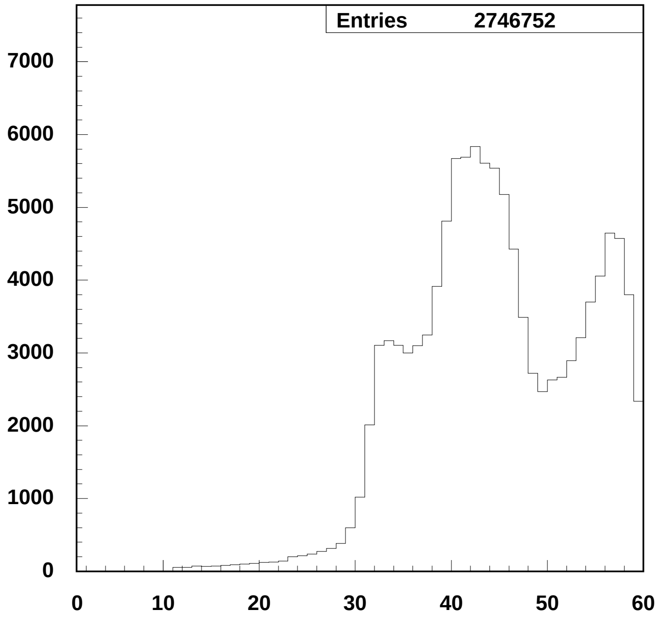

Fig. B.5: Number of Crystals Used in Box Killing Algorithm for 95 Data.

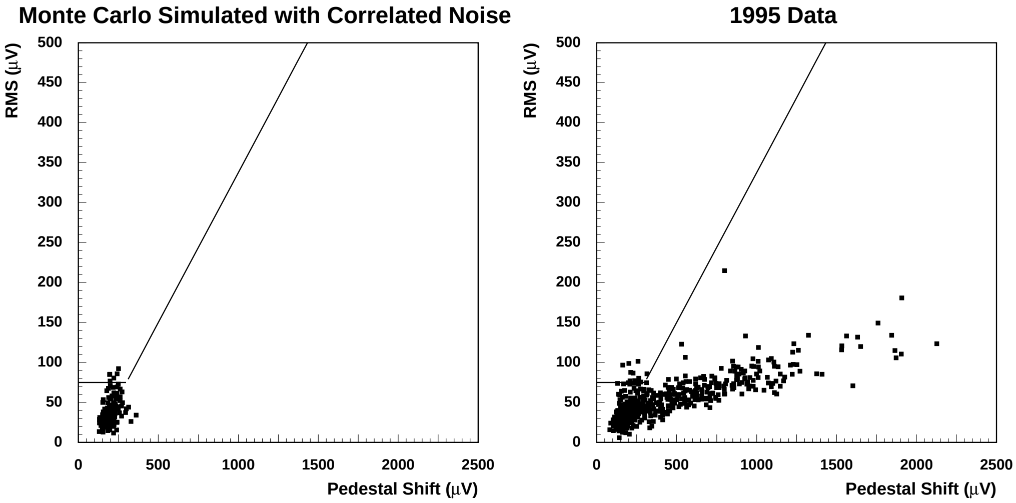

Fig. B.6: RMS Spread for Box Killing Candidates in Data and Monte Carlo.

Remarks

1) The **Local Flatness Test** was tuned by the Multi-photon Group to give the best performance for their signals. In the absence of a noise simulation in the Monte Carlo, it was believed that this routine had a low failure rate, which is not the case as seen in Figure B.11. Improvement could possibly be made by restricting the computed RMS to within the ring and then comparing it with something characteristic of the intrinsic noise, not the average ring RMS.

2) The **Ring Readout Fraction Test** used to check that the fraction of readings lying below the windowed baseline did not exceed the fraction found in the baseline. This was somehow lost.

3) **Box Killing** does not iterate to remove stray baseline estimators and then to recheck the minimum number of estimators requirement before recomputing an average baseline. This was a mistake.
The original purpose of **Box Killing** was to remove large noise spikes which were affecting the summed energy in the event (hence the forceful name). When possible, it is the most accurate means for computing the pedestal.

Results

In the case where all channels are read unsparsed, the correlated noise can be very accurately removed, as demonstrated in Figure B.7 using the unsparsed fill data. However, in normal sparsed data mode, the amount of correlated noise removed is a function of how many channels were used to de-correlate and for particular BGO bumps, the distribution of bump crystals among different rings.

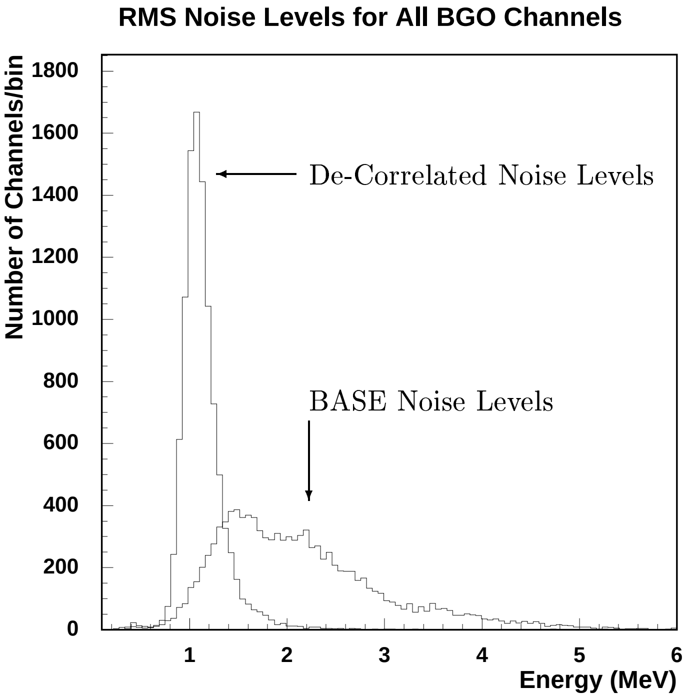

Fig. B.7: Noise Levels After De-Correlation Compared to BASE Noise Levels.

A routine ECNOISE was written to do the explicit calculation of the total noise present in a bump, based on which crystals in an array of 3×3 were readout. The distributions for 94 and 95 Data are presented separately in Figure B.8. The 9 spikes in the de-correlated distributions correspond to how many of the crystals of the bump were present in the same ring. There is still a tail of uncorrected pedestal baselines going above 10 MeV, but the peak of the calculated noise spectrum for 9 crystals is shown to be at $\sqrt{9}$ MeV, the ideal uncorrelated case.

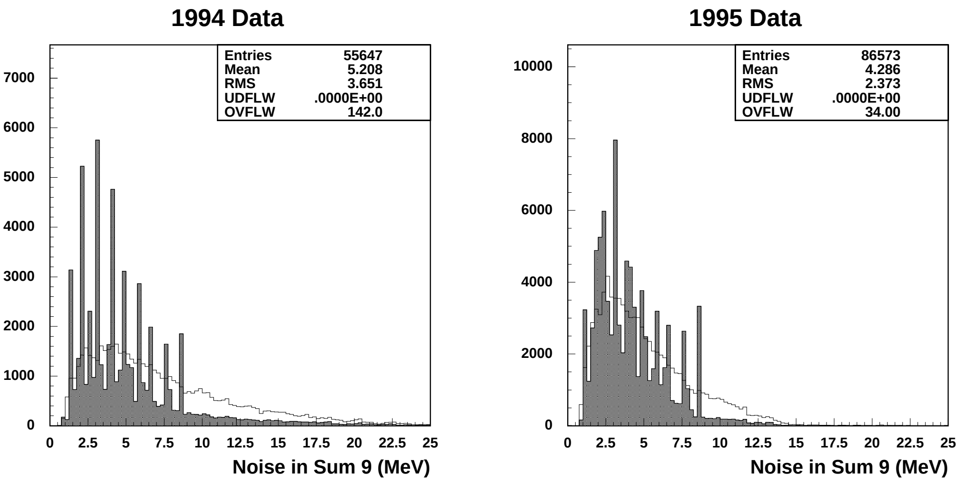

Fig. B.8: Calculated Noise in the Sum of 9 Crystals for 94 and 95 Data.

The detailed study of the de-correlation algorithm first required accurate noise simulation to be included in the Monte Carlo. The routines to do this were written based on the QE_532 simulation parameters. Previously, the Monte Carlo was simulated with 3 MeV thresholds, 0.1 MeV of global correlated noise, and only added intrinsic noise to channels readings.

The QE_532 Monte Carlo is simulated with no noise, and no thresholds. Then, within the ECRWMC routine, the digitization bank is expanded to include unsparsed channels and then intrinsic and correlated noise is added to all channels. The event is then processed by an exact replica of the ECCORNO routine running within the Monte Carlo reconstruction routine ECENMC. The noise was added assuming only box ground correlations and tuned to match roughly the observed data performance with the same resolution and efficiency improvements on the π^0 spectrum. Figure B.9 shows a comparison of QE_532 with noise and threshold simulation with the 1994 fill 2313. There will always be some discrepancy with the Monte Carlo because it is difficult to model accurately the large non-Gaussian pedestal swings which occur in data (see Figure B.6).

In 1995, the π^0 spectrum is much improved, as seen in Figure B.10 (rescaled mass). This resolution is to be compared with an ideal Monte Carlo resolution of 6.7 MeV (no noise, no thresholds and perfect energy calibration and linearity). However, the large variation between the two years in

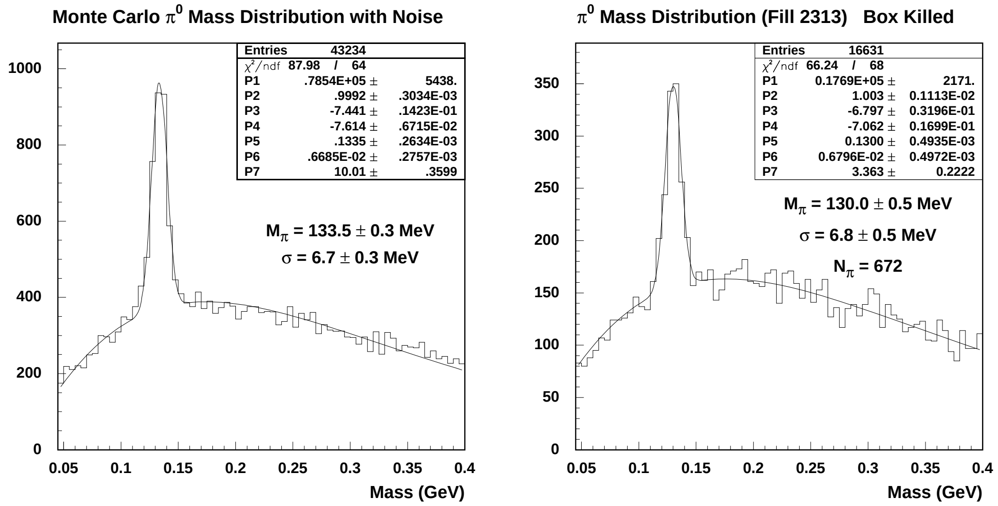

Fig. B.9: Comparison of QE_532 Monte Carlo with Noise and 1994 Fill 2313.

noise levels warrants statistical use of the database entries from both years instead of hardwired values in the Monte Carlo noise simulation.

The general effects of the noise de-correlation routine on low energy data is to improve the ratio of the corrected sum of 9 to the corrected sum of 25 towards higher values for isolated photons, and to improve the accuracy of the energy measurements. In Table B.1, the result of the routine on π^0 data and QE_532 Monte Carlo with and without noise is shown.

Data Type	Uncorrected	De-Correlated	Box Killed
1994 Unsparsed Fill	6.5 %	5.4 % (+10%)	5.4 % (+19%)
1994 Data Fill 2313	6.0 %	5.0 % (+20%)	5.2 % (+29%)
1995 Data	6.1 %		5.2 % (+4%)
Monte Carlo (noise)	6.5 %		5.1 % (+8%)
Monte Carlo (noise)	6.0 %		5.0 % (+6%)
Monte Carlo (no noise)	5.0 %		5.0 % (+0%)

Tab. B.1: π^0 Mass Resolution (+Efficiency Increase) from Noise De-Correlation.

A detailed picture of the routine's effect comes from plotting the energy spectrum of subtracted channels. As shown in Figure B.11, the failure rate of the routine from the **Local Flatness Test** is fairly large, where large is about 10^{-3} at 2.5 MeV. With 192 decisions per event, this rate means

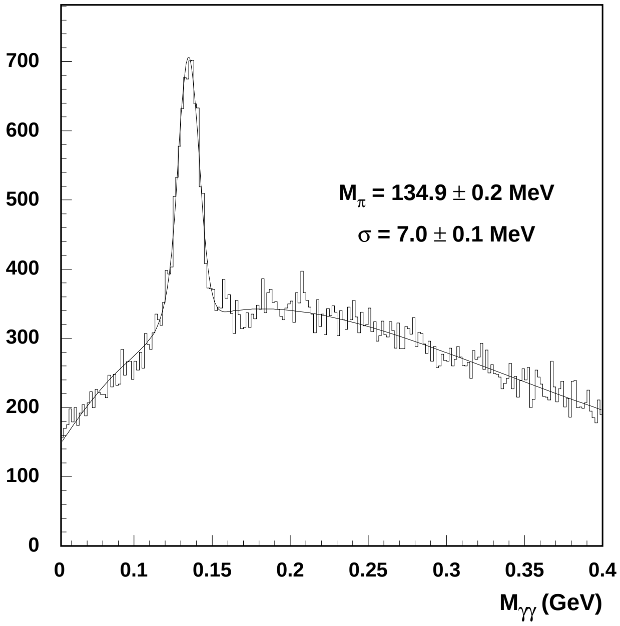

Fig. B.10: 1995 π^0 Mass Spectrum Compared to an Ideal Monte Carlo Resolution of 6.7 MeV.

that once every 5 events, at most 0.5% of the crystal readings have been over-corrected by 2.5 MeV (however, this may have still been better than leaving a 5 MeV correlated shift, for example). Clearly, the main concern is to keep the failure rate down, and most important is to make sure the energy spectrum of failed subtractions dies off quickly with energy.

Both single crystal de-correlation tests die off at 10^{-6} failure rates above 10 MeV. **Box Killing** is applied less frequently in Monte Carlo as shown in Figure B.6. A notable comparison is that in roughly 12k no-noise Monte Carlo events, corresponding to 2 million de-correlation decisions, **Box Killing** is run about 5 times, subtracting an average of 4 MeV from a single ring. In data, **Box Killing** occurs on average 10 times per event with energy spectra going well into the tens of MeV in 1995 and hundreds of MeV in 1994.

As mentioned in the introductory remarks on correlated noise, the effective readout threshold for each crystal varies from event-to-event. However, with the information from the noise de-correlation routine, the thresholds can be estimated. This technique has been implemented in the routine ECTHRES. The distribution of thresholds for a sample of crystals in a 1994 data fill is shown in Figure B.12.

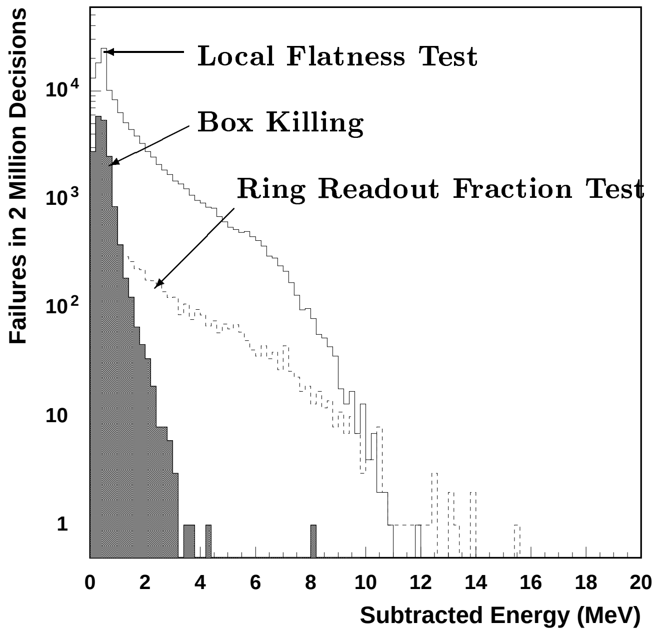

Fig. B.11: Subtracted Energy Spectrum for Noise De-Correlation Pattern Recognition Failures.

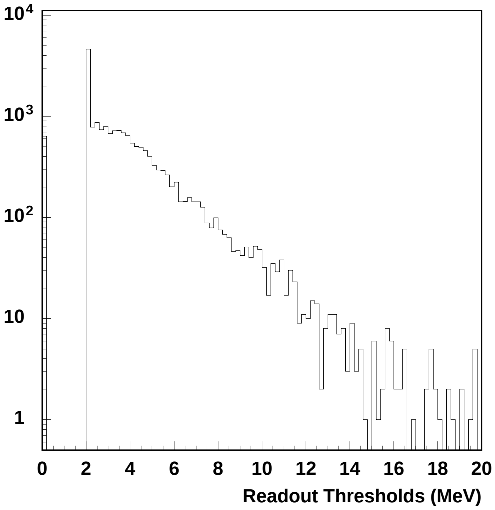

Fig. B.12: Readout Thresholds for 1994 Data Fill showing Unsparsed Channels designated by Zero Threshold and the Software Cut for PP Bank Creation at 2 MeV.

Conclusions

Calculation and simulation techniques have been developed for the BGO Noise De-Correlation Routine ECCORNO. With these new tools, any potential faults or biases with the algorithm can be studied. The calculated noise contribution in the sum of 9 crystals can go directly in an energy resolution function such as ECEMRES, and the threshold calculations from ECTHRES can be used to make better sense out of shower shape parameters. The improvement on the readout percentage, threshold modeling and noise contributions should give better agreement between data and Monte Carlo comparisons on a wide variety of computed quantities. The general structure of the ECCORNO routine as well as a few comments are provided for potential future development and tuning of the algorithm.

C. CONSTRAINED FIT DETAILS

This appendix discusses the mathematical details of the constrained kinematic fit. The fitter[1] was written by Scott S. Snyder. Excerpts of his thesis are included here for reference [32].

The problem to be solved is this: given a set of measurements $\mathbf{x}^m$ and their error matrix $G_{ij}^{-1} = \langle \delta x_i^m \delta x_j^m \rangle$, what is the smallest change one can make to $\mathbf{x}$ to make them satisfy a given set of constraints $F_i(\mathbf{x}) = 0$?

That is, minimize the quantity $\chi^2 = (\mathbf{x} - \mathbf{x}^m)^T \mathbf{G} (\mathbf{x} - \mathbf{x}^m)$, subject to the constraints $\mathbf{F}(\mathbf{x}) = 0$. The algorithm, which is based on SQUAW kinematic fitting program [33, 34], is developed in this section.

C.1 Definitions

Divide the set of variables into 'well-measured' and 'poorly measured' sets. Let $\mathbf{x}$ and $\mathbf{y}$ be column vectors of the well-measured and poorly-measured variables, respectively. (Whole vectors and matrices are denoted by **boldface** symbols, and their elements by subscripted plain symbols.) Denote the measured values of the variables by $\mathbf{x}^m$, $\mathbf{y}^m$, the 'true' values of the variables by $\mathbf{x}^t$, $\mathbf{y}^t$, their values after iteration ν by $\mathbf{x}^\nu$, $\mathbf{y}^\nu$, and their values at the end of the fit by $\mathbf{x}^f$, $\mathbf{y}^f$. The error matrices are given by

$$\begin{aligned} G_{ij}^{-1} &\equiv \langle \delta x_i^m \delta x_j^m \rangle \\ Y_{ij}^{-1} &\equiv \langle \delta y_i^m \delta y_j^m \rangle, \end{aligned} \tag{C.1}$$

where it is tacitly assumed that $\langle \delta x_i^m \delta y_j^m \rangle = 0$. (Here, $\delta \mathbf{x}^m = \mathbf{x}^m - \mathbf{x}^t$.)

The fitting algorithm will be designed to reference only the arrays $\mathbf{G}^{-1}$ and $\mathbf{Y}$, not their inverses. This permits one to specify that a well-measured variable is constant by setting the appropriate diagonal element in $\mathbf{G}^{-1}$ to

---

[1] The method of convergence testing was changed following the removal of "cut steps."

zero. One can also specify that a poorly measured variable is completely unknown by setting the appropriate element in $\mathbf{Y}$ to zero.

It is convenient to define the displacement vectors

$$\begin{aligned}\mathbf{c} &= \mathbf{x} - \mathbf{x}^m \\ \mathbf{d} &= \mathbf{y} - \mathbf{y}^m.\end{aligned} \tag{C.2}$$

The constraints which must be satisfied are given by the row vector

$$\mathbf{F}(\mathbf{x}^\nu, \mathbf{y}^\nu) = \mathbf{F}^\nu = 0 \tag{C.3}$$

with gradients

$$\begin{aligned}B_{\mathbf{x}i\lambda}(\mathbf{x}^\nu, \mathbf{y}^\nu) &= B^\nu_{\mathbf{x}i\lambda} = \frac{\partial F^\nu_\lambda}{\partial x_i} \\ B_{\mathbf{y}i\lambda}(\mathbf{x}^\nu, \mathbf{y}^\nu) &= B^\nu_{\mathbf{y}i\lambda} = \frac{\partial F^\nu_\lambda}{\partial y_i}.\end{aligned} \tag{C.4}$$

A column vector of Lagrange multipliers $\boldsymbol{\alpha}^\nu$ will also be needed.

The quantity which should be minimized subject to the constraints $\mathbf{F} = 0$ is

$$\chi^2 = \mathbf{c}^T\mathbf{G}\mathbf{c} + \mathbf{d}^T\mathbf{Y}\mathbf{d}. \tag{C.5}$$

C.2 Fit

In order to minimize the χ^2 subject to the constraints $\mathbf{F} = 0$, use the method of Lagrange multipliers and minimize the quantity

$$M = \mathbf{c}^T\mathbf{G}\mathbf{c} + \mathbf{d}^T\mathbf{Y}\mathbf{d} + 2\mathbf{F}\boldsymbol{\alpha}. \tag{C.6}$$

At the minimum, it must be the case that

$$0 = \frac{\partial M}{\partial \boldsymbol{\alpha}} = \mathbf{F} \tag{C.7}$$

$$0 = \frac{\partial M}{\partial \mathbf{x}} = \mathbf{G}\mathbf{c} + \mathbf{B}_\mathbf{x}\boldsymbol{\alpha} \tag{C.8}$$

$$0 = \frac{\partial M}{\partial \mathbf{y}} = \mathbf{Y}\mathbf{d} + \mathbf{B}_\mathbf{y}\boldsymbol{\alpha}. \tag{C.9}$$

Write (C.7) in terms of $\mathbf{x}^{\nu+1}$, $\mathbf{y}^{\nu+1}$ and linearize around $\mathbf{x}^\nu$, $\mathbf{y}^\nu$:

$$\begin{aligned}0 &= \mathbf{F}^\nu + (\mathbf{x}^{\nu+1} - \mathbf{x}^\nu)^T\mathbf{B}^\nu_\mathbf{x} + (\mathbf{y}^{\nu+1} - \mathbf{y}^\nu)^T\mathbf{B}^\nu_\mathbf{y} \\ &= \mathbf{F}^\nu + (\mathbf{c}^{\nu+1} - \mathbf{c}^\nu)^T\mathbf{B}^\nu_\mathbf{x} + (\mathbf{d}^{\nu+1} - \mathbf{d}^\nu)^T\mathbf{B}^\nu_\mathbf{y}.\end{aligned} \tag{C.10}$$

Make the definitions

$$\mathbf{E} \equiv \mathbf{G}^{-1}\mathbf{B}_{\mathbf{x}} \tag{C.11}$$
$$\mathbf{H} \equiv \mathbf{E}^T\mathbf{B}_{\mathbf{x}} = \mathbf{B}_{\mathbf{x}}^T\mathbf{G}^{-1}\mathbf{B}_{\mathbf{x}} \tag{C.12}$$
$$\mathbf{r} \equiv \mathbf{c}^T\mathbf{B}_{\mathbf{x}} + \mathbf{d}^T\mathbf{B}_{\mathbf{y}} - \mathbf{F}. \tag{C.13}$$

Note that $\mathbf{H}$ is symmetric, $\mathbf{H}^T = \mathbf{H}$.

Then (C.10) yields

$$\mathbf{r}^\nu = \mathbf{c}^{\nu+1T}\mathbf{B}_{\mathbf{x}}^\nu + \mathbf{d}^{\nu+1T}\mathbf{B}_{\mathbf{y}}^\nu. \tag{C.14}$$

From (C.8) one gets

$$\mathbf{c}^{\nu+1} = -\mathbf{E}^\nu\boldsymbol{\alpha}^{\nu+1} \tag{C.15}$$

so

$$\mathbf{r}^\nu = -\boldsymbol{\alpha}^{\nu+1T}\mathbf{H}^\nu + \mathbf{d}^{\nu+1T}\mathbf{B}_{\mathbf{y}}^\nu \tag{C.16}$$

or

$$\mathbf{r}^{\nu T} = -\mathbf{H}^\nu\boldsymbol{\alpha}^{\nu+1} + \mathbf{B}_{\mathbf{y}}^{\nu T}\mathbf{d}^{\nu+1}. \tag{C.17}$$

Combining this with (C.9) yields

$$\begin{pmatrix} -\mathbf{H}^\nu & \mathbf{B}_{\mathbf{y}}^{\nu T} \\ \mathbf{B}_{\mathbf{y}}^\nu & \mathbf{Y} \end{pmatrix} \begin{pmatrix} \boldsymbol{\alpha}^{\nu+1} \\ \mathbf{d}^{\nu+1} \end{pmatrix} = \begin{pmatrix} \mathbf{r}^{\nu T} \\ 0 \end{pmatrix}. \tag{C.18}$$

Thus, for each iteration, given $\mathbf{x}^\nu$ and $\mathbf{y}^\nu$, evaluate $\mathbf{F}^\nu$, $\mathbf{B}_{\mathbf{x}}^\nu$, and $\mathbf{B}_{\mathbf{y}}^\nu$. Then calculate $\mathbf{E}^\nu$, $\mathbf{H}^\nu$, and $\mathbf{r}^\nu$, and find $\boldsymbol{\alpha}^{\nu+1}$ and $\mathbf{d}^{\nu+1}$ by solving (C.18). Finally, $\mathbf{c}^{\nu+1}$ follows from (C.15).

C.3 χ^2 Calculation

Define

$$\begin{pmatrix} \mathbf{W} & \mathbf{V}^T \\ \mathbf{V} & \mathbf{U} \end{pmatrix} \equiv \begin{pmatrix} -\mathbf{H} & \mathbf{B}_{\mathbf{y}}^T \\ \mathbf{B}_{\mathbf{y}} & \mathbf{Y} \end{pmatrix}^{-1}. \tag{C.19}$$

Note that since both $\mathbf{H}$ and $\mathbf{Y}$ are symmetric, $\mathbf{W}$ and $\mathbf{U}$ are also symmetric.

Multiplying out (C.19) yields

$$\begin{aligned} -\mathbf{H}\mathbf{W} + \mathbf{B}_{\mathbf{y}}^T\mathbf{V} &= 1 & \qquad \mathbf{B}_{\mathbf{y}}\mathbf{W} + \mathbf{Y}\mathbf{V} &= 0 \\ -\mathbf{H}\mathbf{V}^T + \mathbf{B}_{\mathbf{y}}^T\mathbf{U} &= 0 & \qquad \mathbf{B}_{\mathbf{y}}\mathbf{V}^T + \mathbf{Y}\mathbf{U} &= 1. \end{aligned} \tag{C.20}$$

From these relations, one can derive the identities

$$\begin{aligned}\mathbf{WHW} + \mathbf{V}^T\mathbf{YV} &= (\mathbf{V}^T\mathbf{B_y} - 1)\mathbf{W} + \mathbf{V}^T(-\mathbf{B_y}\mathbf{W}) \\ &= -\mathbf{W},\end{aligned} \tag{C.21}$$

$$\begin{aligned}\mathbf{VHV}^T + \mathbf{UYU} &= (\mathbf{UB_y})\mathbf{V}^T + \mathbf{U}(1 - \mathbf{B_y}\mathbf{V}^T) \\ &= \mathbf{U},\end{aligned} \tag{C.22}$$

and

$$\begin{aligned}\mathbf{V}^T\mathbf{YU} + \mathbf{WHV}^T &= \mathbf{V}^T(1 - \mathbf{B_y}\mathbf{V}^T) + (\mathbf{V}^T\mathbf{B_y} - 1)\mathbf{V}^T \\ &= 0.\end{aligned} \tag{C.23}$$

Now, combining (C.19) with (C.18) yields

$$\begin{pmatrix} \boldsymbol{\alpha} \\ \mathbf{d} \end{pmatrix}^{\nu+1} = \begin{pmatrix} \mathbf{W} & \mathbf{V}^T \\ \mathbf{V} & \mathbf{U} \end{pmatrix}^{\nu} \begin{pmatrix} \mathbf{r}^T \\ 0 \end{pmatrix}^{\nu}, \tag{C.24}$$

or, multiplying it out,

$$\boldsymbol{\alpha}^{\nu+1} = \mathbf{W}^{\nu}\mathbf{r}^{\nu T} \tag{C.25}$$

and

$$\mathbf{d}^{\nu+1} = \mathbf{V}^{\nu}\mathbf{r}^{\nu T}. \tag{C.26}$$

Also, from (C.15),

$$\mathbf{c}^{\nu+1} = -\mathbf{E}^{\nu}\mathbf{W}^{\nu}\mathbf{r}^{\nu T}. \tag{C.27}$$

Pulling these all together and plugging them into the χ^2 definition (C.5), the result is (suppressing ν superscripts)

$$\begin{aligned}\chi^2 &= \mathbf{c}^T\mathbf{Gc} + \mathbf{d}^T\mathbf{Yd} \\ &= (-\mathbf{rWE}^T)\mathbf{G}(-\mathbf{EWr}^T) + (\mathbf{rV}^T)\mathbf{Y}(\mathbf{Vr}^T) \\ &= \mathbf{r}(\mathbf{WHW} + \mathbf{V}^T\mathbf{YV})\mathbf{r}^T \\ &= -\mathbf{rWr}^T \\ &= -\mathbf{r}\boldsymbol{\alpha}.\end{aligned}$$

Thus,

$$\left(\chi^2\right)^{\nu+1} = -\mathbf{r}^{\nu}\boldsymbol{\alpha}^{\nu+1}. \tag{C.28}$$

C.4 Convergence

The fit is deemed to have converged if the following two criteria are satisfied for two iterations in a row:

$$\sum_{\lambda} |F_{\lambda}^{\nu+1}| < \epsilon_1 \tag{C.29}$$

$$|(\chi^2)^{\nu+1} - (\chi^2)^{\nu}| < \epsilon_2 \quad \text{or} \quad |(\chi^2)^{\nu+1} - (\chi^2)^{\nu}| < \epsilon_3\,(\chi^2)^{\nu+1} \tag{C.30}$$

That is, when the constraints are satisfied and the χ^2 has stopped changing.

If after several iterations, the constraint sum $\sum_{\lambda} |F_{\lambda}|$ is not decreasing and the convergence conditions have not been met, then convergence is aided with the use of directed steps. If a directed step is not able to reduce the constraint sum, then the constraint problem undoubtedly has a very large χ^2 and no further iterations are made. If the constraint sum is reduced, then normal iteration of the constraint problem is continued.

C.4.1 Directed Steps

For a directed step, try to take the smallest step which satisfies the constraints; i.e., minimize

$$N = \boldsymbol{\gamma}^T \mathbf{G} \boldsymbol{\gamma} + \boldsymbol{\delta}^T \mathbf{Y} \boldsymbol{\delta} + 2\mathbf{F}\boldsymbol{\beta} \tag{C.31}$$

by stepping to $\mathbf{x}'$, $\mathbf{y}'$, where

$$\boldsymbol{\gamma} = \mathbf{x}' - \mathbf{x}^{\nu}, \qquad \boldsymbol{\delta} = \mathbf{y}' - \mathbf{y}^{\nu}. \tag{C.32}$$

After linearizing, this gives

$$0 = \mathbf{F}^{\nu} + \boldsymbol{\gamma}^T \mathbf{B}_{\mathbf{x}}^{\nu} + \boldsymbol{\delta}^T \mathbf{B}_{\mathbf{y}}^{\nu} \tag{C.33}$$

$$0 = \mathbf{G}\boldsymbol{\gamma} + \mathbf{B}_{\mathbf{x}}^{\nu}\boldsymbol{\beta} \quad \longrightarrow \quad \boldsymbol{\gamma} = -\mathbf{G}^{-1}\mathbf{B}_{\mathbf{x}}^{\nu}\boldsymbol{\beta} \tag{C.34}$$

$$0 = \mathbf{Y}\boldsymbol{\delta} + \mathbf{B}_{\mathbf{y}}^{\nu}\boldsymbol{\beta} \quad \longrightarrow \quad \boldsymbol{\delta} = -\mathbf{Y}^{-1}\mathbf{B}_{\mathbf{y}}^{\nu}\boldsymbol{\beta}. \tag{C.35}$$

Putting together (C.33) and (C.34) yields

$$-\mathbf{H}^{\nu}\boldsymbol{\beta} + \mathbf{B}_{\mathbf{y}}^{\nu T}\boldsymbol{\delta} = -\mathbf{F}^{\nu T}. \tag{C.36}$$

Combining this with (C.35),

$$\begin{pmatrix} -\mathbf{H} & \mathbf{B}_{\mathbf{y}}^T \\ \mathbf{B}_{\mathbf{y}} & \mathbf{Y} \end{pmatrix}^{\nu} \begin{pmatrix} \boldsymbol{\beta} \\ \boldsymbol{\delta} \end{pmatrix} = \begin{pmatrix} -\mathbf{F}^T \\ 0 \end{pmatrix}^{\nu}. \tag{C.37}$$

This can be solved to find $\boldsymbol{\beta}$ and $\boldsymbol{\delta}$, and thence $\boldsymbol{\gamma}$.

Using (C.19), the result is

$$\begin{pmatrix} \boldsymbol{\beta} \\ \boldsymbol{\delta} \end{pmatrix} = \begin{pmatrix} \mathbf{W} & \mathbf{V}^T \\ \mathbf{V} & \mathbf{U} \end{pmatrix}^{\nu} \begin{pmatrix} -\mathbf{F}^T \\ 0 \end{pmatrix}^{\nu}, \tag{C.38}$$

or

$$\boldsymbol{\beta} = -\mathbf{W}^{\nu}\mathbf{F}^{\nu T} \qquad \boldsymbol{\delta} = -\mathbf{V}^{\nu}\mathbf{F}^{\nu T}. \tag{C.39}$$

Then calculate the resulting χ^2 (using (C.20)):

$$\begin{aligned}
\left(\chi^2\right)' &= \mathbf{c}'^T\mathbf{G}\mathbf{c}' + \mathbf{d}'^T\mathbf{Y}\mathbf{d}' \\
&= (\boldsymbol{\gamma} + \mathbf{c}^{\nu})^T\mathbf{G}(\boldsymbol{\gamma} + \mathbf{c}^{\nu}) + (\boldsymbol{\delta} + \mathbf{d}^{\nu})^T\mathbf{Y}(\boldsymbol{\delta} + \mathbf{d}^{\nu}) \\
&= \boldsymbol{\gamma}^T\mathbf{G}\boldsymbol{\gamma} + \boldsymbol{\delta}^T\mathbf{Y}\boldsymbol{\delta} + 2\boldsymbol{\gamma}^T\mathbf{G}\mathbf{c}^{\nu} + 2\boldsymbol{\delta}^T\mathbf{Y}\mathbf{d}^{\nu} + \mathbf{c}^{\nu T}\mathbf{G}\mathbf{c}^{\nu} + \mathbf{d}^{\nu T}\mathbf{Y}\mathbf{d}^{\nu} \\
&= \boldsymbol{\beta}^T\mathbf{B}_{\mathbf{x}}^{\nu T}\mathbf{G}^{-1}\mathbf{G}\mathbf{G}^{-1}\mathbf{B}_{\mathbf{x}}^{\nu}\boldsymbol{\beta} - \boldsymbol{\beta}^T\mathbf{B}_{\mathbf{y}}^{\nu T}\mathbf{Y}^{-1}\mathbf{Y}\boldsymbol{\delta} \\
&\quad - 2\boldsymbol{\beta}^T\mathbf{B}_{\mathbf{x}}^{\nu T}\mathbf{G}^{-1}\mathbf{G}\mathbf{c}^{\nu} - 2\boldsymbol{\beta}^T\mathbf{B}_{\mathbf{y}}^{\nu T}\mathbf{Y}^{-1}\mathbf{Y}\mathbf{d}^{\nu} + \left(\chi^2\right)^{\nu} \\
&= \boldsymbol{\beta}^T\mathbf{H}^{\nu}\boldsymbol{\beta} - \boldsymbol{\beta}^T\mathbf{B}_{\mathbf{y}}^{\nu T}\boldsymbol{\delta} - 2\boldsymbol{\beta}^T(\mathbf{B}_{\mathbf{x}}^{\nu T}\mathbf{c}^{\nu} + \mathbf{B}_{\mathbf{y}}^{\nu T}\mathbf{d}^{\nu}) + \left(\chi^2\right)^{\nu} \\
&= \boldsymbol{\beta}^T(-\mathbf{H}^{\nu}\mathbf{W}^{\nu}\mathbf{F}^{\nu T} + \mathbf{B}_{\mathbf{y}}^{\nu T}\mathbf{V}^{\nu}\mathbf{F}^{\nu T}) - 2\boldsymbol{\beta}^T(\mathbf{r} + \mathbf{F})^{\nu T} + \left(\chi^2\right)^{\nu} \\
&= \mathbf{F}^{\nu}\boldsymbol{\beta} - 2(\mathbf{r} + \mathbf{F})^{\nu}\boldsymbol{\beta} + \left(\chi^2\right)^{\nu} \\
&= \left(\chi^2\right)^{\nu} - 2\mathbf{r}^{\nu}\boldsymbol{\beta} - \mathbf{F}^{\nu}\boldsymbol{\beta}.
\end{aligned} \tag{C.40}$$

BIBLIOGRAPHY

[1] Harvey B. Newman and Thomas Ypsilantis, editors. *History of Original Ideas and Basic Discoveries in Particle Physics.* NATO ASI Series. Plenum Press, New York, 1996.

[2] C. M. G. Lattes, G. P. S. Occhialini, and C. F. Powell. Observations of the Tracks of Slow Mesons in Photographic Emulsions. *Nature*, **159**: 486, 1947.

[3] M. Gell-Mann. *Physics Letters*, **8**:214, 1964.

G. Zweig. CERN Preprint 8181/TH-401 and 8419/TH-412. 1964.

[4] J. D. Bjorken. *Physical Review*, **179**:1547, 1969.

[5] C. G. Callan and D. J. Gross. *Physical Review Letters*, **22**:156, 1969.

[6] D. J. Gross and C. H. Llewellyn-Smith. *Nuclear Physics*, **B14**:337, 1969.

[7] *Proceedings of the XVIIth International Conference on High Energy Physics*, London, 1974, M. Haguenauer, p. IV-95; F. Sciulli, p. IV-105; D. C. Cundy, p. IV-131.

[8] D. J. Gross and F. Wilczek. *Physical Review Letters*, **30**:1343, 1973.

H. D. Politzer. *Physical Review Letters*, **30**:1346, 1973.

[9] F. J. Hasert *et al.* (Gargamelle Collaboration). *Physics Letters B*, **46**: 121 and 138, 1973.

[10] G. Arnison et al (UA1 Collaboration). *Physics Letters B*, **126**:398, 1983.

P. Bagnaia et al (UA2 Collaboration). *Physics Letters B*, **129**:130, 1983.

[11] S. L. Glashow, J. Iliopoulos, and L. Maiani. *Physical Review*, **D2**:1285, 1970.

[12] S. L. Glashow. *Nuclear Physics*, **22**:579, 1961.

A. Salam. N. Svartholm, ed. (Stockholm: Almqvist). page 367, 1968.

S. Weinberg. *Physical Review Letters*, **19**:1264, 1967.

[13] S. Abachi *et al.* (D0 Collaboration). *Physical Review Letters*, **74**:2632, April 1995.

(URL: `http://d0wop.fnal.gov/d0pubs/journals/PRL_top`)

F. Abe *et al.* (CDF Collaboration). *Physical Review Letters*, **74**:2626, April 1995.

(URL: `http://www-cdf.fnal.gov/top_status/prl_cdf.ps`)

[14] Y. J. Pei. A Simple Approach to describe Hadron Production Rates in e^+e^- Annihilation. *Zeitschrift für Physik C*, **72**:39, 1996.

[15] R. M. Barnett *et al.* Review of Particle Physics. *Physical Review*, **D54**: 1, 1996.

[16] J. J. Sakurai. *Advanced Quantum Mechanics.* Addison-Wesley, New York, 1967.

[17] B. Adeva *et al.* (L3 Collaboration). The Construction of the L3 Experiment. *Nuclear Instruments and Methods in Physics Research*, **A289**: 35–102, 1990.

[18] I. C. Brock *et al.* Luminosity Measurement in the L3 Detector at LEP. *Nuclear Instruments and Methods in Physics Research*, **A381**:236, 1996.

[19] Xudong Cai. *Contribution à l'élaboration et à la mise en œuvre du système de déclenchement et d'acquisition de l'expérience L3 au LEP.* PhD thesis, Université de Savoie, Laboratoire d'Annecy-Le-Vieux de Physique des Particules, 1994.

[20] M. Acciarri *et al.* (L3 SMD Collaboration). The L3 Silicon Microvertex Detector. *Nuclear Instruments and Methods in Physics Research*, **A351**: 300–312, 1994.

[21] V. Innocente, M. Maire, and E. Nagy. GEANE: Average Tracking and Error Propagation Package. *CERN Program Library*, **W5013-E**, July 1991.

V. Innocente and E. Nagy. Trajectory Fit in Presence of Dense Materials. *Nuclear Instruments and Methods in Physics Research*, **A324**: 297–306, 1993.

[22] Marcel Merk. *Study of Bhabha Scattering at the Z^0-Resonance using the L_3 Detector*. PhD thesis, Universiteit Nijmegan, 1992.

[23] Yannis Karyotakis. The L3 Electromagnetic Calorimeter. In H. S. Chen, editor, *Beijing Calorimetry Symposium*, pages 27–35, Beijing, China, 1995.

[24] Philip E. Kaaret. *Forward Production of J/Ψ in Hadronic Interactions and Calibration of a Large BGO Electromagnetic Calorimeter*. PhD thesis, Princeton University, 1989.

[25] R. Y. Zhu, G. Gratta, D. Kirkby, W. Lu, R. Mount, H. Newman, S. Shevchenko, U. Chaturvedi, M. Ilyas, M. Vivargent, S. X. Wu, and C. Tully. An RFQ Calibration System for L3 BGO Calorimeter. *Nuclear Physics B (Proc. Suppl.)*, **44**:109–115, 1995.

[26] V. E. Barnes *et al. Physical Review Letters*, **12**:204, 1964.

[27] M. Acciarri *et al.* (L3 Collaboration). Measurement of Cross Sections and Leptonic Forward-Backward Asymmetries at the Z Pole and Determination of Electroweak Parameters. *Zeitschrift für Physik C*, **62**: 551–573, 1994.

[28] G. Alexander *et al.* (OPAL Collaboration). Σ^+, Σ^0 and Σ^- Hyperon Production in Hadronic Z^0 Decays. *Zeitschrift für Physik C*, **73**:587–600, 1997.

[29] W. Adam *et al.* (DELPHI Collaboration). Production of Σ^0 and Ω^- in Z Decays. *Zeitschrift für Physik C*, **70**:371–382, 1996.

[30] P. Bialas, J. G. Körner, M. Krämer, and K. Zalewski. Joint angular decay distributions in exclusive weak decays of heavy mesons and baryons. *Zeitschrift für Physik C*, **57**:115–134, 1993.

[31] P. J. E. Peebles. *Principles of Physical Cosmology*. Princeton University Press, Princeton, New Jersey, 1993.

[32] Scott Stuart Snyder. *Measurement of the Top Quark Mass at DØ*. PhD thesis, State University of New York at Stony Brook, 1995.
(URL: `http://www-d0.fnal.gov/publications_talks/thesis/snyder/thesis-ps.html`)

[33] J. Peter Berge, Frank T. Solmitz, and Horace D. Taft. *Review of Scientific Instruments*, **32**(5):538–548, May 1961.

[34] O. I. Dahl, T. B. Day, F. T. Solmitz, and N. L. Gould. SQUAW Kinematic Fitting Program. Technical Report P-126, Lawrence Radiation Laboratory, Berkeley, California, July 1968.